Vascular Remodeling in Pulmonary Hypertension

by

Neil J. Kelly

Bachelor of Science in Biology, Massachusetts Institute of Technology, 2007

Bachelor of Science in Mathematics, Massachusetts Institute of Technology, 2007

Submitted to the Graduate Faculty of

University of Pittsburgh School of Medicine in partial fulfillment

of the requirements for the degree of

Doctor of Philosophy

University of Pittsburgh

2015

UNIVERSITY OF PITTSBURGH

SCHOOL OF MEDICINE

This dissertation was presented

by

Neil J. Kelly

It was defended on

July 29, 2015

and approved by

Timothy D. Oury, MD, PhD
Committee Chair
Professor, Department of Pathology

Elena A. Goncharova, PhD
Associate Professor, Department of Medicine

Wendy M. Mars, PhD
Associate Professor, Department of Pathology

Robert M. O'Doherty, PhD
Professor, Department of Medicine

Steven D. Shapiro, MD
Major Advisor
Professor, Department of Medicine

Vascular Remodeling in Pulmonary Hypertension

Neil J. Kelly, PhD

University of Pittsburgh, 2015

Pulmonary hypertension (PH) is a rare but deadly disease whose victims bear a 40% chance of mortality within the first five years of diagnosis. Although current treatment strategies have been successful at subduing symptoms of PH, they have done little to prolong the survival of those afflicted. PH is characterized histopathologically by, among other characteristics, hyperplasia and hypertrophy of the smooth muscle cells (SMCs) that constitute the medial layer of the pulmonary resistance arteries and which are thought to decrease the compliance and increase the resistance of the pulmonary vasculature. Over time, these changes increase the burden on the right heart and ultimately lead to its failure and patient death. While recent advances have greatly increased our understanding of pulmonary vascular remodeling, knowledge of these mechanisms is far from complete. Furthermore, the translation of putative mechanisms to animal models is hindered by inadequate tools to quantify medial thickening. Here we present a new method for the quantification of vascular remodeling. In addition, we describe a novel mechanism whereby a conserved 20 amino acid peptide (SR20) in the carboxyterminal domain (CTD) of macrophage elastase (MMP12) induces the expression of tumor necrosis factor-related apoptosis-inducing ligand (TRAIL). TRAIL is known to preferentially induce apoptosis in tumor cells, and we demonstrate the efficacy of SR20 and the MMP12 CTD *in vitro* and *in vivo* as a cytotoxic agent against tumor cells. TRAIL is also known to paradoxically increase the proliferation of vascular SMCs, and we present evidence that the MMP12 CTD increases the proliferation of pulmonary arterial SMCs through upregulation of TRAIL with potential links to PH. Finally, we present the results of a genome-wide association study in 36 inbred and wild-derived mouse strains exposed to a chronic high-fat diet-induced model of PH to uncover novel candidate genes linked to PH pathogenesis. The results of these studies should aid investigators in all areas of basic PH research through the provision of superior methods. Meanwhile, the identification of the MMP12

CTD as a mitogen for pulmonary SMCs, and the identification of genomic regions linked to PH development, will help improve our understanding of PH pathogenesis.

TABLE OF CONTENTS

LIST OF TABLES

LIST OF FIGURES

PREFACE

First, I would like to thank my mentor Steve Shapiro, whose support for my work and education has been unflinching. Steve has stood by me as I learned the universal truths about the difficulty of science and as we cherished the hard-won successes. Furthermore, his mounting burden of responsibilities and time-constraints has never been evident in the priority that Steve gives to his lab and his students, teaching us about lung diseases, macrophages, proteases, and the intricacies of the Pittsburgh healthcare market. I am tremendously grateful to have had the opportunity to work for such an outstanding scientist and mentor, and I am certain that I would not be at this point without his guidance.

Next, I am forever indebted to my colleagues and friends in the Shapiro Lab, particularly Nadine Dandachi, whose partnership in science and example in life will remain with me throughout my career. In addition, Adriana Leme, Paula Nave, John Wood, Chris Burton, Alyssa Gregory, Andy Metz, Stephen Scott, Justin Beiriger, Robin Chambers, and Brittani Agostini were incredible colleagues who were always willing to help – no matter how crazy or unimportant a particular experiment may have seemed. A special acknowledgement goes to Josiah Radder, who – beyond his tremendous talent and helpfulness in genomics and otherwise – always has a healthy skepticism and love of scientific conversations that keep me thinking about new ideas. In addition, I would like to thank the many friends and colleagues I have from four

years as a graduate student. One of the great pleasures of graduate school was the recurring opportunity to see a face in the hallway and strike up a conversation about life or science, knowing that the person on the other end is a friend.

The Vascular Medicine Institute is an amazing place to study, largely thanks to the vision and energy of Mark Gladwin, who has recruited some of the world's best scientists to work in its labs. The man who keeps the VMI running is Jeff Baust, a tireless worker and wondrous microsurgeon who does his best to accommodate the needs of every scientist at the VMI. I am also immensely thankful to my friends Elena Goncharova and Dmitry Goncharov, who have been amazing colleagues and are generously willing to share their time and expertise. Additionally, I would like to acknowledge how lucky I was to work at an institution with a state-of-the art imaging facility, the Center for Biologic Imaging (CBI), and an incredible staff to make use of this unique resource. Simon Watkins, the director of the CBI, and Claudette St. Croix were instrumental in taking our image-analysis tools from concept to reality.

All of my doctoral education has happened in the larger context of two exceptional programs: the Cellular and Molecular Pathology (CMP) graduate program, and the Medical Scientist Training Program (MSTP). I owe a great deal to Wendy Mars, the director of CMP, who always made sure that progress was made and milestones were met. Moreover, Wendy knows a lot about everything – and everything about the liver – which frequently leads to exciting scientific conversations, often with some implication to hepatology. In the MSTP, I would like to thank our program director Richard Steinman, our outgoing administrator Manjit Singh, Justin Markuss, and my career advisor Clayton Wiley for their constant and ongoing support. In addition, I would like to thank the members of my thesis committee – Steve, Elena,

Wendy, Tim Oury, and Rob O'Doherty – who, it seems, saw a completely different set of experiments each time we met but still had the faith to see me through to the end.

Finally, I would like to thank my mother, father, siblings, and friends for making the past four years about more than just science and education, but also about seeing the world, learning to golf, and enjoying some of the best years of my life.

1.0 INTRODUCTION

Pulmonary hypertension (PH) is a complex disease of the pulmonary circulation whose known therapies offer only symptomatic relief. PH is a rare disease, contributing to approximately 6.5 of every 100,000 deaths in the United States [1]; in a French national registry [2], PH had a prevalence of 15 cases per million adults and an annual incidence of 2.4 cases per million adults while disproportionately affecting women. While rare, PH is also deadly – in multiple national cohorts from France, the United Kingdom and Ireland [3], and the United States [4, 5], the 5-year mortality for PH is roughly 40%.

Clinically, PH is defined on the basis of right-heart catheterization as a sustained mean pulmonary artery pressure (mPAP) of greater than or equal to 25 mmHg at rest [6]. PH can arise from a multitude of causes and is classified accordingly: the latest guidelines [7] categorize PH based upon the underlying mechanism as pulmonary arterial hypertension (PAH), PH due to left-sided heart disease, PH due to lung disease and/or hypoxia, chronic thromboembolic pulmonary hypertension, and pulmonary hypertension with unclear multifactorial mechanisms (Table 1).

Table 1. Classification of pulmonary hypertension.

Group 1	Pulmonary arterial hypertension (PAH)
Group 2	Pulmonary hypertension due to left heart disease
Group 3	Pulmonary hypertension due to lung diseases and/or hypoxia
Group 4	Chronic thromboembolic pulmonary hypertension (CTEPH)
Group 5	Pulmonary hypertension with unclear multifactorial mechanisms

The subpopulation known as Group 1 PH (PAH) is defined as PH with an end-expiratory pulmonary artery wedge pressure (PAWP) of less than or equal to 15 mmHg, thereby excluding "backup" from elevated left-sided pressures as the source of PH, and pulmonary vascular resistance (PVR) greater than 3 wood units [6].

1.1 PATHOGENESIS OF PULMONARY HYPERTENSION

The form and function of the pulmonary vascular system are closely intertwined: the system must rapidly deliver large quantities of blood – 4-6 L/min – to the 2-cell-thick capillary-alveolus barrier where gas exchange can occur. In order to accommodate the rapid delivery of large quantities of blood to such a fragile barrier without causing endothelial injury or pulmonary edema, the system is designed as a high-volume, low-pressure, and low-resistance circuit [8]. In PAH, this carefully-crafted system is disrupted by an effective narrowing of the pulmonary vessels – in short, a shift in the normal balance of vessel tone favoring vasoconstrictive factors over their vasodilatory counterparts. Among the earliest molecular studies in PH were those which observed upregulation of the secreted vasoconstrictor peptide endothelin-1 (ET-1) [9] and downregulation of the vasodilatory enzyme endothelial nitric oxide synthase (eNOS, also known as NOS3) [10] in patients with PH. Similarly, hypoxic vasoconstriction, which functions physiologically to divert pulmonary blood flow to oxygenated alveoli, contributes to the development of Group 3 PH in the setting of lung disease with global hypoxia [11]. From Pouseille's Law, $R = 8L\eta/\pi r^4$, where R is resistance and r is radius, we see that even a small decrease in vessel radius can lead to a tremendous increase in PVR.

The natural history of PAH can perhaps be best understood in the context of a circulatory interpretation of Ohm's Law $Q = \Delta P/R$, where Q is the flow rate through the circuit, ΔP the pressure gradient across the circuit, and R the resistance of the circuit [8]. In the case of the pulmonary vasculature, this equation becomes

$$CO = \frac{mPAP - PAWP}{PVR}$$

where CO is the cardiac output and PAWP is interpreted as the left atrial pressure. In PAH, the vessel radius is decreased and PVR is increased; hence, for CO to remain constant, mPAP must necessarily increase. In other words, the right ventricle of the heart (RV) must pump against an increasing afterload in order to maintain a constant flow-rate through the pulmonary vasculature. As PAH progresses, the normally thin-walled RV hypertrophies to compensate for the increased afterload, and its eventual failure is the direct cause of mortality in approximately half of PAH patients [12]. Therefore, an understanding of PAH morbidity and mortality requires knowledge of the precipitating events behind elevated PVR.

1.2 HISTOPATHOLOGY OF PULMONARY HYPERTENSION

Among the five clinical groupings of PH, all share similar morphologic findings: atheroma formation and thickening of the medial smooth muscle cell layer of the small (40-300 μm) arteries [13, 14]. Meanwhile, PAH features prominent medial thickening – which involves both hypertrophy and hyperplasia of the smooth muscle fibers – as well as thickening of the intimal (endothelial cell) and adventitial (extracellular matrix) layers of the pulmonary arteries [13]. These changes, termed constrictive lesions when they infringe on the vessel lumen, are thought

to play a significant role in the pathogenesis of PH by increasing vessel stiffness and physically intruding on the cross-sectional area of the lumen to increase PVR (Figure 1).

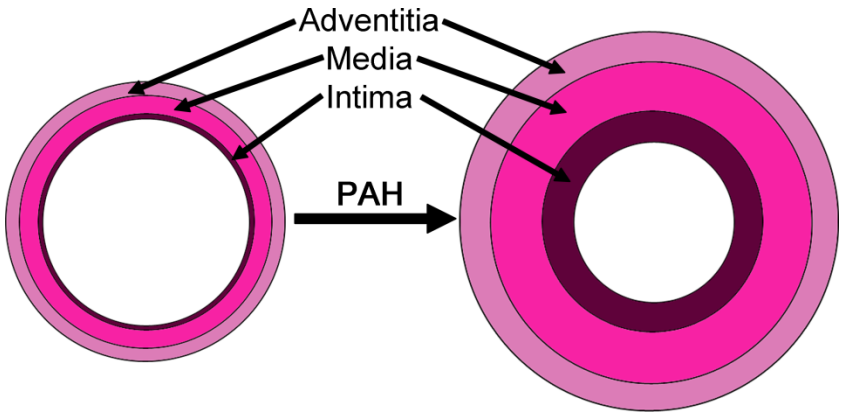

Figure 1. Schematic of histopathological changes in the pulmonary vasculature during PAH.

Importantly – despite its ubiquitous presence in the pulmonary arteries of PH patients – medial thickening is neither necessary nor sufficient for the development of PH. In human patients with chronic obstructive pulmonary disease (COPD), medial thickening has been observed in the absence of PH [15], perhaps because it involves predominantly outward thickening which does not infringe on the vessel lumen [16]. In contrast, treatment of chronically hypoxic rats with the angiotensin-converting enzyme (ACE) inhibitor cilazapril reversed medial thickening but did not affect PH [17]. Hence, it is likely that the type of vessel thickening, as well as the activities of endogenous vasodilatory and vasoconstrictive factors, determines the net relationship between wall thickness and PH. Nonetheless, the mechanisms behind medial thickening and, more generally, vascular remodeling, remain topics of vigorous investigation in the field of PH.

1.3 GENETICS OF PULMONARY ARTERIAL HYPERTENSION

The genetic factors behind PAH have provided valuable insights into the overall pathogenesis of PH. Familial PAH (FPAH; also known as Hereditary PAH, or HPAH) accounts for approximately ~2-4% of PAH cases [2, 4], defined as PAH with either (1) two or more family members with documented PAH or (2) a rare genetic variant known to be associated with PAH, such as *BMPR2* [7]. While approximately 80% of FPAH cases involve known mutations, most commonly related to Bone Morphogenic Protein Receptor 2 (BMPR2) signaling (Table 2), the causative factor behind ~20% of PAH cases remains unknown despite a clear autosomal dominant pattern of inheritance [18].

Table 2. Gene mutations associated with PAH

Gene Symbol	Synonyms	Gene Name	Ref.
BMPR2	--	Bone morphogenic protein receptor, type 2	[19, 20]
ACVRL1	*ALK1*	Activin A receptor type II-like 1	[21]
ENG	*HHT1*	Endoglin	[21]
SMAD9	--	SMAD family member 9 (encodes SMAD8 protein)	[22]
CAV1	--	Caveolin 1	[23]
KCNK3	--	Potassium channel, two pore domain subfamily K, member 3	[24]
EIF2AK4	*GCN2*	Eukaryotic translation initiation factor 2 alpha kinase 4	[25, 26]
CBLN2	--	Cerebellin 2 precursor	[27]

Coupling knowledge of the histopathologic findings from all of PH with genetic insights from FPAH, molecular biologists have begun to deduce the connections between the two with a seemingly simple question: how do genetic perturbations in the identified genes ultimately lead to the medial thickening and vascular remodeling observed in histological sections?

1.4 MECHANISMS OF PULMONARY VASCULAR REMODELING

As mentioned, pulmonary vascular remodeling of the medial smooth muscle cells (SMCs) involves primarily: (1) excessive migration, chiefly involving activation of Rho kinase (ROCK) [28, 29], (2) increased proliferation, and (3) resistance to apoptosis of SMCs [30].

1.4.1 BMP Signaling

BMPR2 is the most commonly mutated gene in FPAH, and understanding of its physiological role in bone morphogenic protein (BMP) signaling has offered significant insights into PAH pathogenesis. BMPs, the ligands for BMPR2, are members of the transforming growth factor-beta (TGFB) superfamily of cytokines and signal through receptor serine/threonine kinases [31]. Upon BMP binding, BMPR2, a type II receptor of the TGFB receptor superfamily [32], recruits and phosphorylates a type I receptor, typically BMPR1A or BMPR1B. In the case of BMP9 binding, it has recently been shown the BMPR2 also heterodimerizes with ALK1 [33], perhaps explaining its association with FPAH. The phosphorylated type I receptor then phosphorylates receptor-regulated R-SMADs – SMAD1, 5, or 8 – which bind to the co-SMAD, SMAD4, translocate to the nucleus, and promote apoptosis while inhibiting the proliferation of VSMCs (Figure 2) [34, 35]. Of the genes associated with FPAH, three genes (*BMPR2*, *ALK1*, and *SMAD9*) are also involved in BMP signaling, highlighting the importance of this pathway to PAH pathogenesis. However, while BMP signaling is commonly affected by mutation, several other pathways have been found to be significantly altered in patients with PH.

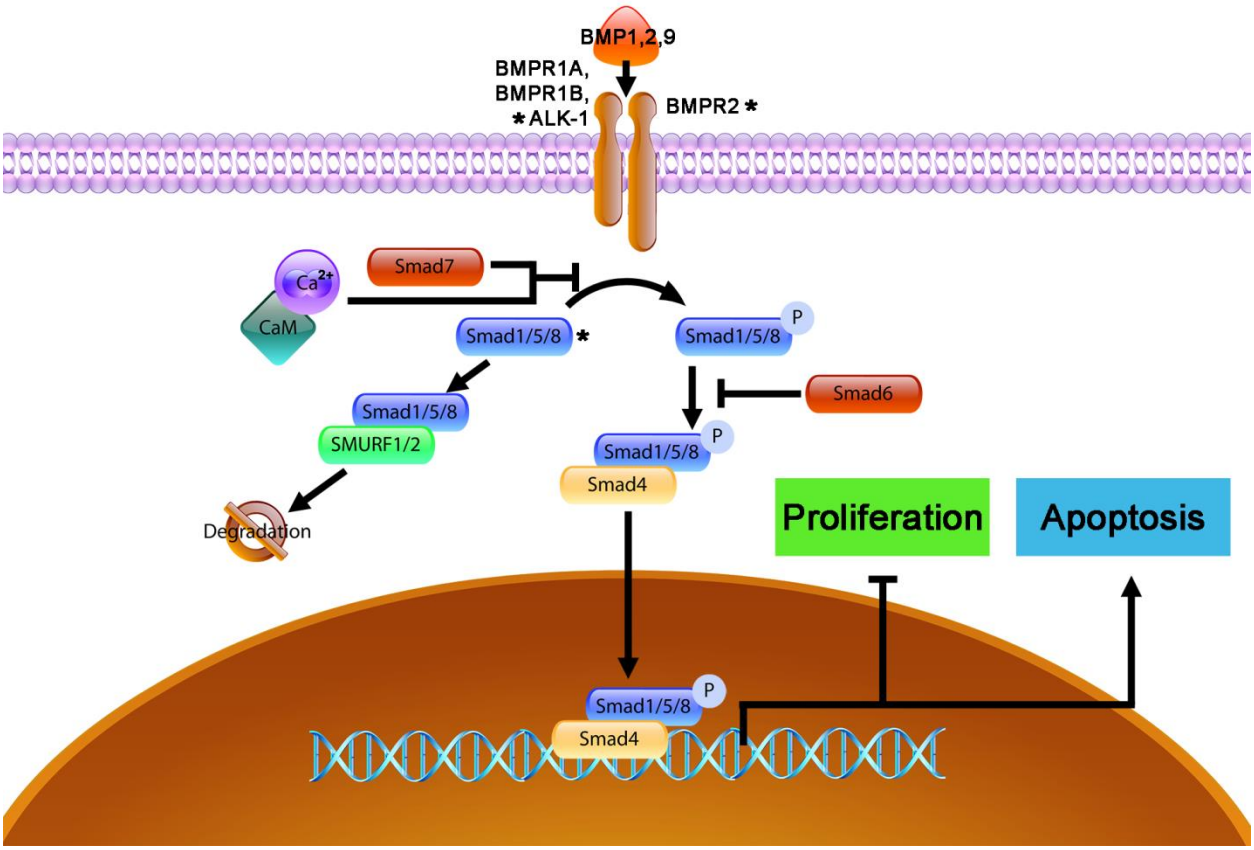

Figure 2. BMP-induced SMAD signaling in PH.
BMP: Bone morphogenic protein. CaM: Calmodulin. SMURF: SMAD ubiquitination and regulatory factor. (*) denotes proteins mutated in FPAH.

1.4.2 Intracellular cation concentrations

Early observations showed that elevated intracellular concentrations of potassium drive membrane depolarization in VSMCs from human and rodent PH [36-38]. The relevance of intracellular K^+ to PH pathology gained increased attention from a recent human study reporting an association between FPAH and mutations in the *KCNK3* gene encoding TASK1, a pH-sensitive potassium channel [24]. Intracellular K^+ is a major contributor to cell volume, and increased K^+ concentrations contribute to resistance from apoptosis by (*i*) prevention of apoptotic volume decrease, or AVD [39, 40], and (*ii*) inhibition of cytoplasmic apoptotic effector caspases

[41, 42]. In rodent models, treatment with dichloroacetate (DCA) [43, 44] or dehydroepiandrosterone (DHEA) [45], which potentiate K^+ efflux through membrane channels, prevented and reversed experimental PH by promoting VSMC apoptosis.

Intracellular K^+ can also promote proliferation through cross-talk with Ca^{2+}, an essential driver of VSMC proliferation [46, 47] whose concentration is increased in VSMCs from human PH patients [48]. In addition, the numerous ligands – including growth factors (EGF, FGF, PDGF), serotonin (5HT), endothelin (ET-1), interleukins, and others – that promote VSMC proliferation in PH [30, 35, 49] typically act through two pathways: (*i*) signaling through MAPK with nuclear translocation of pERK1/2 and activation of proliferative genes [35, 50], or (*ii*) increasing the intracellular concentration of calcium. In the setting of PH, cytosolic calcium concentrations are elevated primarily by (*i*) increased influx through transient receptor potential cation channels (TRPC) [51-53] and (*ii*) increased release from intracellular stores [30, 54]. Calcium influx may also be increased by opening of voltage-gated calcium channels in response to the depolarization that accompanies elevated intracellular potassium concentrations; however, these channels are not thought to play a significant role in PH [30, 35].

Elevated calcium concentrations have a multitude of downstream effects in pulmonary VSMCs, including antagonism of BMP2R/SMAD signaling (see Figure 2) and promotion of migration and proliferation [55]. Calcium signaling also leads to activation of the transcription factor NFAT, which represses transcription of the K^+ channels and further exacerbates intracellular K^+ concentrations [56]. Hence, increased cytosolic potassium and calcium concentrations are critical mediators of the proliferation and resistance to apoptosis observed in VSMCs in PH.

1.4.3 The role of hypoxia

The cellular response to hypoxia is controlled by the hypoxia-inducible factors (HIFs), classically HIF1A [57]. Under normoxic conditions, oxygen-sensing proline residues on HIF1A are hydroxylated which allows binding of the E3 ubiquitin ligase von Hippel Lindau (VHL) and, ultimately, proteasomal degradation of HIF1A. Under hypoxia, however, HIF1A (and also HIF2A) accumulates, heterodimerizes with HIF1B, and translocates to the nucleus where it modulates the transcription of HIF-responsive genes [58, 59].

Given their roles as master regulators of the hypoxic response, it is perhaps unsurprising that mice with heterozygous gene deletions of *Hif1a* [60] or *Hif2a* [61] are protected against chronic hypoxia-induced vascular remodeling and PH. As with other transcription factors, HIF1A and HIF2A have wide-ranging effects on numerous cellular processes. However, their roles in PH are likely to involve calcium influx through upregulation of TRPC [62] as well as systems-level effects mediated through microRNAs [63, 64]. Hence, while PH secondary to hypoxic lung disease is in some ways very different from PAH, the cellular mechanisms driving cellular proliferation are also very similar.

2.0 QUANTIFICATION OF VASCULAR REMODELING

2.1 INTRODUCTION

Vessel remodeling is a hallmark of vascular disease [16, 65] exemplified in the medial hypertrophy and hyperplasia that accompany pulmonary arterial hypertension [66, 67]. In recent years, tremendous progress has been made in defining the migratory, proliferative, and anti-apoptotic stimuli behind this morphologic finding [68]. Surprisingly, however, the geometric quantification of such features in histological sections still relies on a miscellany of outdated methods.

Based on our survey of the literature, a plurality of research articles calculates medial thickness using discrete measurements along the vessel boundary [69]. After wall thickness calculation, measurements are typically normalized to some metric of vessel size ranging from lumen area [70] to discrete measurements of end-to-end distance [69]. As we will show, the choice of measurement methodology can lead to vastly different results which hinder the acquisition of reliable data and the comparison of measurements between research groups.

The aim of this report is to combine old theories with new tools to establish the best method – in a way that is accessible to the majority of researchers in the field – for medial wall thickness measurement. With a focus on the pulmonary vasculature, we bring attention to the shortcomings of commonly-used techniques while presenting a novel and superior approach to

wall thickness measurement based on image skeletonization. In the process, we present a new, freely-available software tool to facilitate the simple and rapid calculation of wall thickness using this new approach.

2.2 METHODS

2.2.1 Animals

All animal experiments were performed in accordance with the Institutional Animal Care and Use Committee (IACUC) of the University of Pittsburgh School of Medicine. Animals were housed within a pathogen-free barrier facility that maintained a 12-hour light/dark cycle in Plexiglas cages (one to two rats or one to four mice per cage) with free access to autoclaved water and irradiated pellet food. Animal health, weight, and overall behavior were monitored throughout the experiments.

2.2.2 Sugen/hypoxia treatment

Induction of pulmonary hypertension by Sugen/hypoxia was performed as described previously [71, 72]. Briefly, 6-8-week-old male C57BL/6J mice (Jackson Laboratories, Bar Harbor, ME, USA) were exposed to hypoxia (10% O_2) for 35 days. At days 0, 7 and 14, mice were injected subcutaneously with SU5416 (20 mg/kg, Tocris BioScience, Bristol, UK). 6-8-week-old male Sprague-Dawley rats (Charles River Laboratories) received a single subcutaneous SU5416 injection (20 mg/kg) and were then maintained under hypoxia (10% O_2) for 3 weeks followed by

5 weeks at normoxia. During hypoxia exposure, the oxygen concentration was maintained using a ProOx Oxygen Controller (BioSpherix, Lacona, NY, USA); the forced circulation and instant homogenization of gases was provided by fan (BioSpherix). Negative controls included vehicle-injected age- and gender-matched animals maintained under normoxia.

2.2.3 Hemodynamics

In vivo pressure-volume (PV) loop measurements of right ventricular (RV) function were performed by a PV catheter in anesthetized animals [73]. Briefly, animals were anesthetized with isoflurane (5% for induction, 2% during surgery, and 1% while performing PV loop measurements). A four-electrode PV catheter (Scisense, Inc., London, ON, Canada) attached to the data acquisition system (EMKA Instruments, Falls Church, VA, USA) was inserted into the apex of the RV. Data were acquired using the PowerLab data acquisition system and LabChart Pro software (AD Instruments, Colorado Springs, CO, USA). Lung tissue was collected upon the completion of data acquisition.

2.2.4 Histology

For images used in line integral estimates, Wistar rat lungs were saline-perfused via the right ventricle and inflated via tracheostomy with 2% paraformaldehyde at 25 cm H_2O for 10 minutes, fixed for 2 hours at room temperature, then washed with 30% sucrose in phosphate-buffered saline (PBS) at 4°C for 16-24 hours. Snap-frozen sections (7μm) were immunostained with a Cy3-conjugated antibody to αSMA (Sigma, St. Louis, MO, USA), an antibody to PECAM (Abcam, Cambridge, UK) followed by incubation with a Cy5-conjugated secondary antibody,

and 4',6-diamidino-2-phenylindole (DAPI; Sigma) to mark nuclei. Images of pulmonary arterioles were captured at 40X magnification using an Olympus Provis fluorescence microscope digital camera system.

For all other analyses, staining was performed using sections of rodent lung tissue which were snap-frozen in OCT embedding compound (Tissue-Tek, Tokyo, Japan) as described [74]. Briefly, lungs were saline-perfused via the right ventricle, inflated via tracheostomy with 80% OCT/20% saline solution at 25 cm H2O for 10 minutes, snap-frozen in OCT embedding compound, and sectioned into 7 μm-thick slices followed by H&E and immuno-staining. Tissue sections were fixed with 3.7% paraformaldehyde in PBS at 4°C for 10 minutes and immunostained with anti-αSMA FITC-conjugated antibody (Sigma). H&E and αSMA stains were visualized at 40X magnification using an Olympus Provis 1 fluorescent microscope and Olympus Fluoview 1000 confocal microscope, respectively.

2.2.5 Literature survey

Journal articles involving non-human organisms, published in the calendar year 2014, and containing the MeSH term "pulmonary hypertension" were included in the survey. Articles with an exclusive focus on cardiac remodeling were excluded. Articles were considered to qualitatively assess medial thickening if they measured the percentage of muscularized arteries or reported and discussed medial thickening using histological images but without quantification. Diameter ranges were only included if they were specifically reported as external vessel diameter.

2.2.6 Software

All software was developed in MATLAB R2012a (MathWorks) using the Image Processing Toolbox and is available at http://www.vmi.pitt.edu/resources/VMIcalculator.html.

2.2.6.1 Image input

The VMI calculator takes RGB image formats and displays the color image in the left axes of the graphical user interface (GUI) while displaying a grayscale version of the selected color channel in the right axes of the GUI. If the selected color channel is "All", the program converts the RGB image to HSV by *rgb2hsv* and displays a grayscale version of the V channel of the resulting image in the right axes.

2.2.6.2 Contrast adjustment

The "Adjust Contrast" button on the VMI calculator GUI allows the user to manually adjust the contrast of the right axes grayscale image using MATLAB's *imcontrast* tool.

2.2.6.3 Image binarization

The VMI calculator binarizes images by thresholding via Otsu's method (*graythresh* in MATLAB) or edge detection by Sobel's method (*edge* in MATLAB). Alternatively, the GUI allows the user to draw regions by *imfreehand* which are interpreted as follows: "Encircle Vessels" sets boundary pixels of the region to 1 in the image binarization, "Fill Mask" sets pixels within the region to 1 in the binarization, and "Erase Mask" sets pixels within the region to 0 in the binarization.

2.2.6.4 Vessel identification

8-connected holes in the black & white image with area less than the user-specified minimum lumen area are automatically filled. From the black & white image binarization, 8-connected regions were considered candidate vessels. Candidate vessels are classified by *bwlabel* on the filled (*imfill*) image to account for the presence of multiple candidates in a single image; hence the labeled region consisted of the vessel wall and its lumen. A candidate is considered an actual vessel if it has an 8-connected hole (lumen) in the wall binarization and a wall area greater than the user-specified minimum wall area.

2.2.6.5 Area calculation

From the labeled image obtained by *bwlabel*, each labeled region (vessel) was considered separately. The number of wall pixels was counted as the number of non-zero pixels in the labeled region that were also non-zero in the wall binarization. The number of lumen pixels was counted as the number of non-zero pixels in the labeled region that were not part of the wall. The number of vessel pixels was the sum of the number of wall pixels and the number of lumen pixels. The area was calculated as the number of pixels in each segment: wall, lumen, or vessel.

2.2.6.6 Boundary method

The boundary method defines the outer boundary as the perimeter points of the vessel region after filling holes by *imfill*. The inner boundary is defined as the perimeter of points in the labeled black & white image that are not the lumen. The square of the Euclidean distance $d^2 = (x_o - x_i)^2 + (y_o - y_i)^2$ is computed for every outer boundary point (x_o, y_o) to every inner

boundary point (x_i, y_i), and the square root of the minimum for each outer boundary point is considered the distance at that outer boundary point. Deselection of the GUI option "Include zero-width sections" omits points of overlap between the outer and inner boundaries. The wall thickness is considered the mean of the boundary method measurements.

2.2.6.7 Rosette method

The rosette method draws a series of lines by MATLAB's *imline* tool at a user specified angle interval ranging from [90°, 450°) for wall thickness and [90°, 270°) for diameter. The line runs through the centroid (x_c, y_c) of the lumen and runs to one image border for the wall thickness or two image borders for diameter. The method returns no result if the lumen centroid lies outside the lumen. The second point of the line at angle θ is $(x_c + 100\cos\theta, y_c + 100\sin\theta)$. From the outer and inner boundaries defined in the boundary method, the wall thickness for each rosette segment is calculated as the Euclidean distance from the segment-intersecting outer boundary point closest to the lumen centroid to the segment-intersecting inner boundary point closest to the lumen centroid. The segment is not included if it does not intersect an outer and inner wall point or if the distance from the centroid to the nearest inner boundary-intersecting point is greater than the distance from the centroid to the nearest outer boundary-intersecting point. Deselection of the GUI option "Include zero-width sections" omits segments of zero distance. The diameter is taken to be the distance between the opposing (opposite directions) outer-boundary points nearest to the centroid. The wall thickness and diameter are considered the means of their respective rosette method measurements.

2.2.6.8 Skeleton method

The skeleton method identifies the minimum skeleton of the wall with the 'thin' command in *bwmorph* with pruning achieved by the 'shrink' command. To eliminate unwanted holes, we consider the minimum skeleton to be the perimeter points of the pruned skeleton after filling all holes. Skeleton length is determined by the *bwdistgeodesic* command using the 'quasi-euclidean' metric. Wall thickness is calculated as wall area A_w divided by skeleton length. External diameter is calculated as calculated as skeleton length divided by π plus wall thickness. Deselection of the GUI option "Include zero-width sections" subtracts the lengths of segments of outer boundary and inner boundary overlap from the skeleton length for the purposes of wall thickness measurement; diameter calculations are unaffected.

2.2.7 Method speed

The time to completion of VMI calculator measurements was measured using the *tic* and *toc* functions in MATLAB; the timer was begun with loading of the image and stopped after the display of results. Time to completion of manual measurements in ImageJ was measured with a stopwatch that was started after the image was loaded and stopped after the completion of measurements. For both methods, diameter and wall thickness were measured at 90° intervals by the rosette method; the VMI calculator also calculated wall area, vessel area, wall thickness by the boundary and skeleton methods, and external diameter by the skeleton method.

2.2.8 Statistics

Measurement repeatability and agreement were assessed according to the methods developed by Bland and Altman [75]. Correlation was measured by Pearson product-moment correlation and distance correlation [76]. Linear regressions were done in MATLAB R2012a (MathWorks). Method performance times were compared by Wilcoxon signed-rank test. Measurements between animal groups were compared by Student's t-test. A p-value of less than 0.05 was considered statistically significant.

2.3 RESULTS

2.3.1 The problem of medial wall thickness quantification

We began our study with the widely used Sugen/hypoxia rat model of pulmonary hypertension [71] and its recently developed mouse corollary [72, 77]. Male Sprague-Dawley rats and C57BL/6J mice were either vehicle-treated in room air (Naïve) or were maintained under hypoxia (10% O_2) receiving subcutaneous injections of the kinase domain insert receptor (KDR, also known as VEGFR2) antagonist Sugen/SU5416 (SuHx). At the end of the treatment period, the presence of pronounced elevation in right ventricular systolic pressure (RVSP) was confirmed by terminal right heart catheterization (Figure 3A). After lung tissue fixation, histological sections were stained with hematoxylin and eosin (H&E) for general assessment of pulmonary arteriolar morphology or α-smooth muscle actin (αSMA) to visualize vascular smooth muscle (Figure 3B). With SuHx treatment, both stains appeared to show qualitative

medial thickening; but what is the appropriate method by which to accurately and reliably quantify this structural change?

Fundamentally, we can think of a vessel's medial wall cross-section as a doughnut-shaped area surrounding the vessel's intima and lumen (for the sake of simplicity, we will refer to the combination of the intima and lumen as the lumen). The wall's inner boundary is defined as the set of wall points adjacent to the lumen, while the outer boundary constitutes all wall points adjacent to the exterior. From these boundaries, we can define the wall thickness T_w at a given point as the distance from the outer boundary to the inner boundary along a line perpendicular to the wall's "backbone" or minimum skeleton – the arc equidistant from the outer and inner wall boundaries [78]. While it would be ideal to calculate wall thickness directly from our definition, we do not know the equation for the minimum skeleton, and local fluctuations along its course can make estimates of the slope unreliable. Hence, we will describe three indirect methods of calculating wall thickness (Figure 3C): the rosette method, the boundary method, and the skeleton method.

In first describing the methods for wall thickness calculation, it is simplest to think of the vessel wall as the area between concentric circles of radii r_o and r_i, respectively, centered at the origin of a Cartesian x-y plane, with a minimum skeleton of radius $r_{sk} = (r_o + r_i)/2$ and uniform wall thickness of $T_w = r_o - r_i$. In the rosette method, a series of lines is drawn from the center of the vessel lumen to the exterior vessel wall, and T_w is calculated as the difference in distances at the line's intersections with the outer boundary, by definition equal to r_o, and the inner boundary, which equals r_i. In the boundary method, we compute the minimum distance from the wall's outer boundary to its inner boundary, and, in the case of boundaries of concentric circles, the minimum distance between the boundaries is $T_w = r_o - r_i$. Finally, in the skeleton

method, we utilize image skeletonization to yield a thinned, maximally pruned version of a region which is equidistant to its boundaries [78]. From the wall area A_w and minimum skeleton length L_{sk}, we calculate $T_w = A_w/L_{sk}$, which is equivalent to the difference in outer and inner radii for concentric circular boundaries.

To validate the methods for the case of concentric circular boundaries, we first show that the difference between r_o and r_i satisfies our definition for wall thickness: at any point along the skeleton defined by $x^2 + y^2 = r_{sk}^2$, we have $2x + 2y\,dy/dx = 0$ and slope $dy/dx = -x/y$. Using the opposite inverse to find the slope of the perpendicular line, we obtain the linear equation $y = (y_0/x_0)x + b$ where y_0 and x_0 correspond to the initial point on the skeleton and b represents the *y*-intercept of the perpendicular line. Substituting our initial values, we see that $b = 0$. Therefore, our perpendicular line passes through the origin, and its distance to the inner and outer boundaries is, by definition, equal to their respective radii. Hence, for concentric circular boundaries, we can define wall thickness as $T_w = r_o - r_i$, and we will use this definition to explain the following methods of wall thickness calculation.

In the rosette method, a series of lines is drawn from the center of the vessel lumen to the exterior vessel wall, and T_w is calculated as the difference in distances at the line's intersections with the outer boundary, by definition equal to r_o, and the inner boundary, which equals r_i.

In the boundary method, we compute the minimum distance from each point on the wall's outer boundary to its inner boundary. In the case of boundaries of concentric circles, we express the Euclidean distance T from an outer wall point (x_o, y_o) to an inner wall point (x_i, y_i) in polar coordinates in terms of their angles, θ_o and θ_i, respectively, from the center of the circle

$$T = \sqrt{(x_o - x_i)^2 + (y_o - y_i)^2}$$

$$= \sqrt{(r_o \cos\theta_o + r_i \cos\theta_i)^2 + (r_o \sin\theta_o + r_i \sin\theta_i)^2}$$

$$= \sqrt{r_o^2 - 2r_o r_i \cos(\theta_o - \theta_i) + r_i^2}$$

Substituting $\varphi = \theta_o - \theta_i$, we have

$$\frac{dT}{d\varphi} = \frac{r_o r_i \sin\varphi}{\sqrt{r_o^2 - 2r_o r_i \cos\varphi + r_i^2}}$$

from which we see that T achieves a minimum at $\sin\varphi = 0$, $\varphi = 0$, and $\theta_o = \theta_i$. Substituting this back into our distance equation, we see

$$T_{\varphi=0} = \sqrt{r_o^2 - 2r_o r_i + r_i^2}$$

$$= \sqrt{(r_o - r_i)^2}$$

$$= r_o - r_i$$

$$= T_w$$

In the skeleton method, we utilize image skeletonization to yield a thinned, maximally pruned – meaning no spurs – version of a region which is equidistant to its boundaries [78]. In the case of our hypothetical vessel wall, this results in a circle of radius $r_{sk} = (r_o + r_i)/2$ and circumferential length $L_{sk} = \pi(r_o + r_i)$. Because the wall area, A_w, is the difference in the areas enclosed by the outer and inner boundaries, we see

$$A_w = \pi r_o^2 - \pi r_i^2$$

$$= \pi(r_o^2 - r_i^2)$$

$$= \pi(r_o + r_i)(r_o - r_i)$$

$$= L_{sk} \times T_w$$

Hence, $T_w = A_w / L_{sk}$.

We developed a free user-friendly tool, which we call the VMI calculator, that semi-automatically binarizes images of vessel wall cross-sections and calculates wall thickness using these three methods as well as vessel component areas and diameters (Figure 3D).

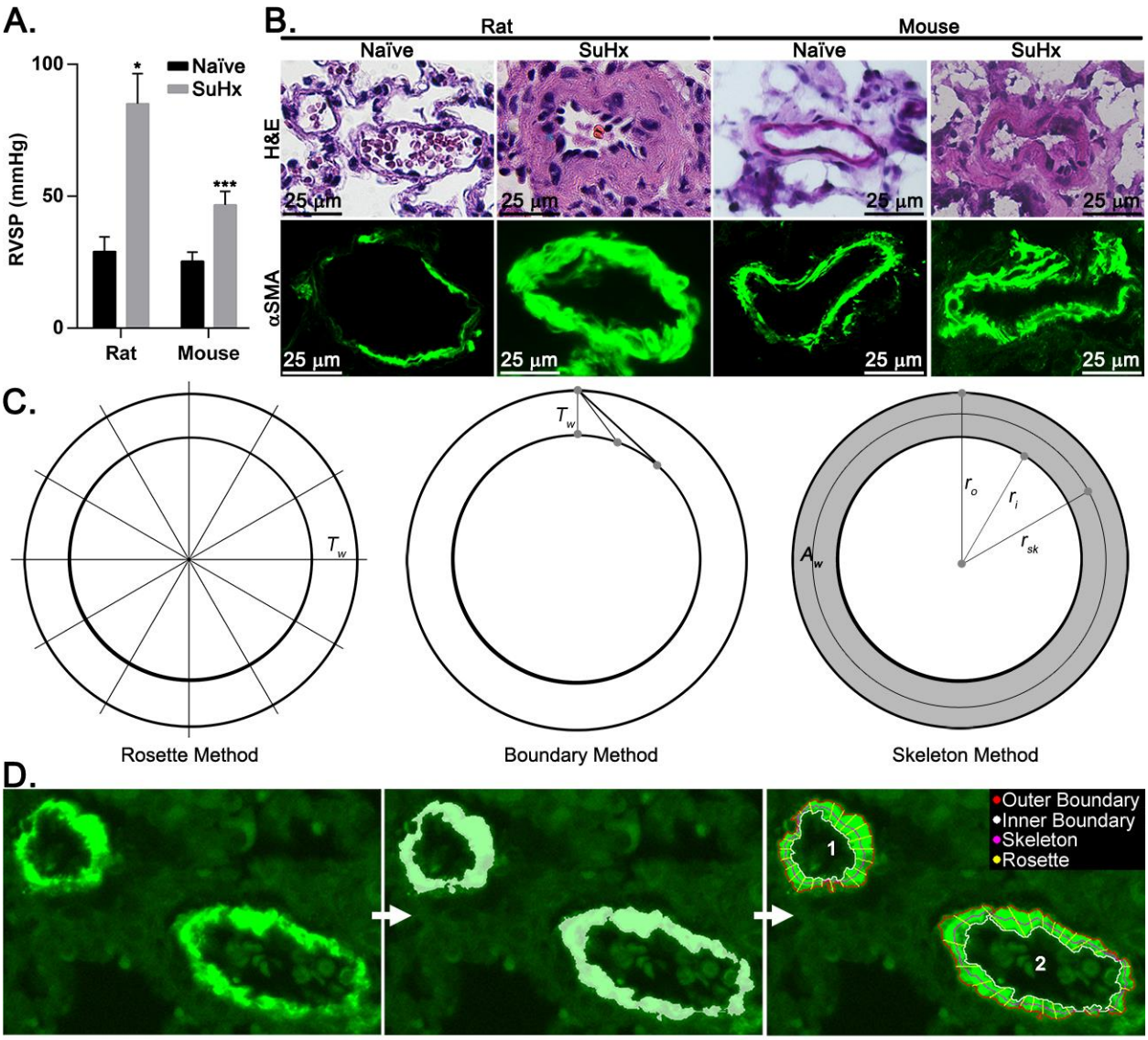

Figure 3. Quantification of vascular remodeling.

Male Sprague-Dawley rats or C57BL/6J mice were treated under room air (Naïve) or received subcutaneous injections of Sugen/SU5416 with hypoxia (10% O2; SuHx). (A) Right ventricular end-systolic pressure (RVSP) was measured by terminal catheterization in Naïve (n=2 rats, 3 mice) and SuHx (n=3 rats, 6 mice) rodents. (B) Representative lung sections stained with hematoxylin and eosin (H&E) or an antibody to α-smooth muscle actin (αSMA) at 40x magnification (scale bars are 25 μm). (C) Schematic representation of the rosette, boundary, and skeleton methods of wall thickness calculation. (D) Example of binarization and visual representation of wall

thickness measurements by the rosette, boundary, and skeleton methods using the VMI calculator. Data are mean + SD. *P<0.05, ***P<0.0005 by two-sided independent sample t-test.

2.3.2 Validation of the VMI calculator

The VMI calculator's wall thickness measurements were compared to manual rosette-method-measurements performed in ImageJ [79] using fifty immunofluorescent images of αSMA-stained vessels. To first verify that the VMI calculator's measurements were in the correct vicinity, we quantified the agreement between the VMI calculator's rosette method and manual measurements using ImageJ at sampling intervals of 90°, meaning 4 equally-spaced measurements per vessel, and 45°, with 8 measurements per vessel. The near-zero biases of -0.54 μm and -0.30 μm for 90° and 45° sampling intervals, respectively (Figure 4A), imply that the two tools are indeed measuring the same quantity. However, the poor agreement between the two methods suggests a lack of precision.

Using repeated measures of wall thickness to examine precision, we can see that the VMI calculator outperforms manual measurements, with a coefficient of repeatability of 1.14 μm versus 2.29 μm at a 90° sampling interval (Figure 4B). With a 5° sampling interval on the VMI calculator, the coefficient of repeatability for the rosette method decreases to 0.29 μm (Figure 4C), while the boundary method (Figure 4D) and skeleton method (Figure 4E) have coefficients of repeatability of 0.57 μm and 0.29 μm, respectively, well within acceptable limits of precision for the vessel sizes under consideration. In addition, the VMI calculator significantly reduced the time required for wall thickness calculation – measured as the time from image loading to the return of results – compared to manual measurements (Figure 4F) while returning vastly more information. In summary, the VMI calculator is both faster and more precise than manual measurements.

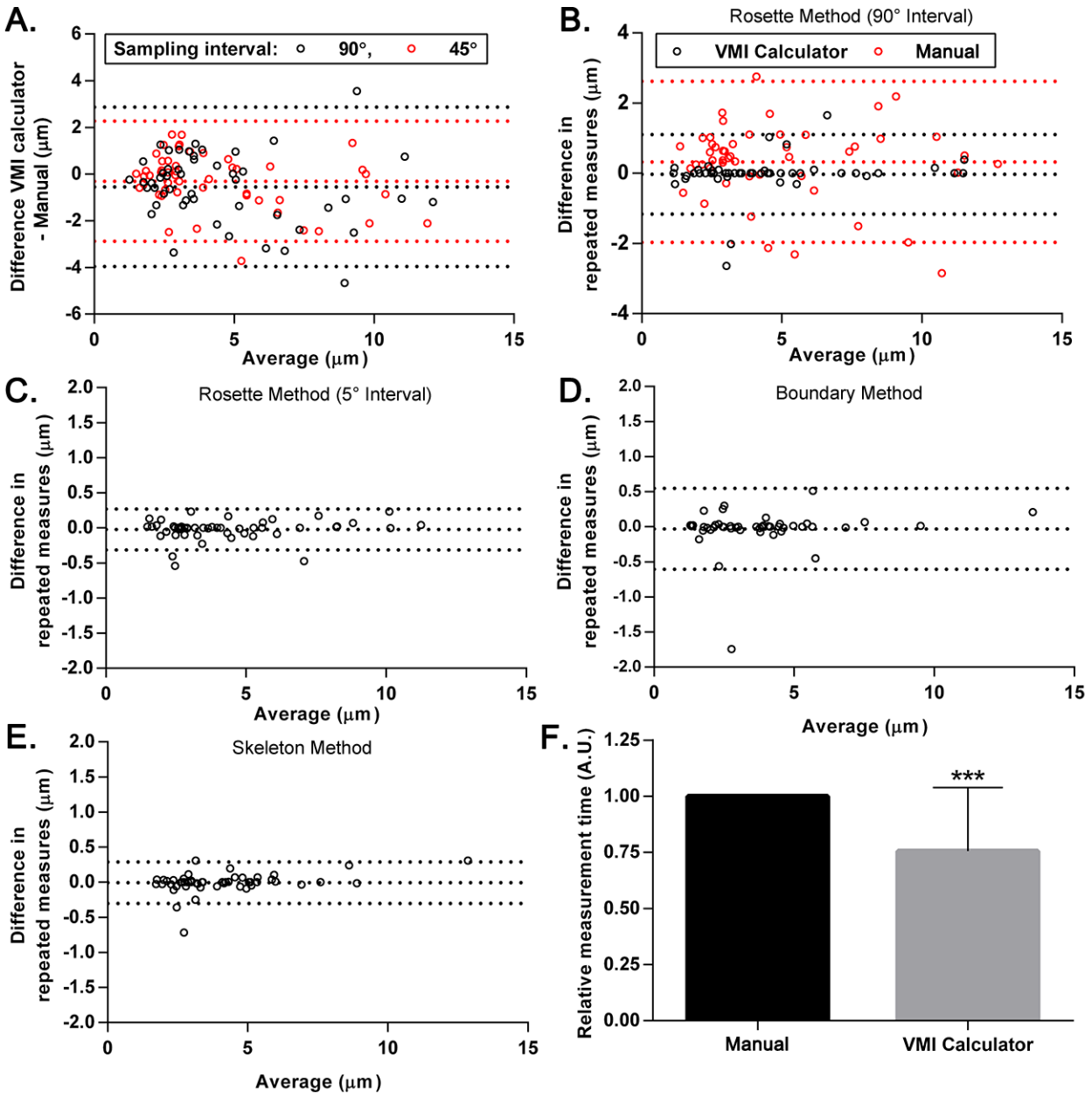

Figure 4. Validation of the VMI calculator.

Bland-Altman plots of (A) difference in VMI calculator measurements and manual measurements by the rosette method at 90° (red) and 45° (black) sampling intervals, (B) difference in repeated measures using the VMI calculator (black) and manual measurements (red) with the rosette method at 90° intervals, and difference in repeated measures by (C) the rosette method at a 5° sampling interval, (D) the boundary method, and (E) the skeleton method (n=50 vessels per plot, dotted lines are mean ± 2SD). (F) Relative time from image loading to vessel quantitation and return of results using manual measurements or the VMI calculator (n=20 images). Data are mean + SD. ***P<0.0005 by Wilcoxon signed-rank test.

2.3.3 Existing approaches to wall thickness measurement

In a survey of 141 journal articles involving animal models of pulmonary hypertension from the 2014 calendar year, 52% of the studies attempted to quantify medial thickening in the pulmonary vasculature. The majority of quantitative studies reported medial wall thickness, in which the value was reported as a raw measurement or as a fraction of vessel diameter, while the remainder of studies utilized area-based approaches (Figure 5A). Furthermore, every wall thickness report that detailed its methods used the rosette method.

Although suitable for vessel boundaries defined by concentric circles, the rosette method's flaws become apparent when considering non-ideal circumstances. Perhaps the most obvious of these shortcomings is that the rosette method will miscalculate T_w when its line segments intersect the wall at non-perpendicular angles, typically resulting in an overestimate of T_w. The second major drawback of the rosette method involves sampling error; to explore this issue, we quantified wall thickness in fifty αSMA-stained vessels by the rosette method at a 5° sampling interval. The issue of sampling error is evident in a comparison of each rosette segment measurement to its vessel's average, which follows a normal distribution with standard deviation of 52% (Figure 5B). Finally, we would expect an ideal measurement system to be independent of a vessel's angular orientation. However, consider the scenario in which the rosette method is applied at a 90° sampling interval, the most common in our literature survey (Figure 5C), and compared to the same measurement taken after rotating the vessel by a mere 5°. Analyzing measurement agreement by the method of Bland and Altman [75], we see limits of agreement (95% confidence interval) of -0.12 ± 1.81 μm (Figure 5D), a range that is hardly suitable for wall

thicknesses of 1 to 12 μm. Taken together, the rosette method – while widely used – is prone to systemic errors that may obscure real differences in medial wall thickness.

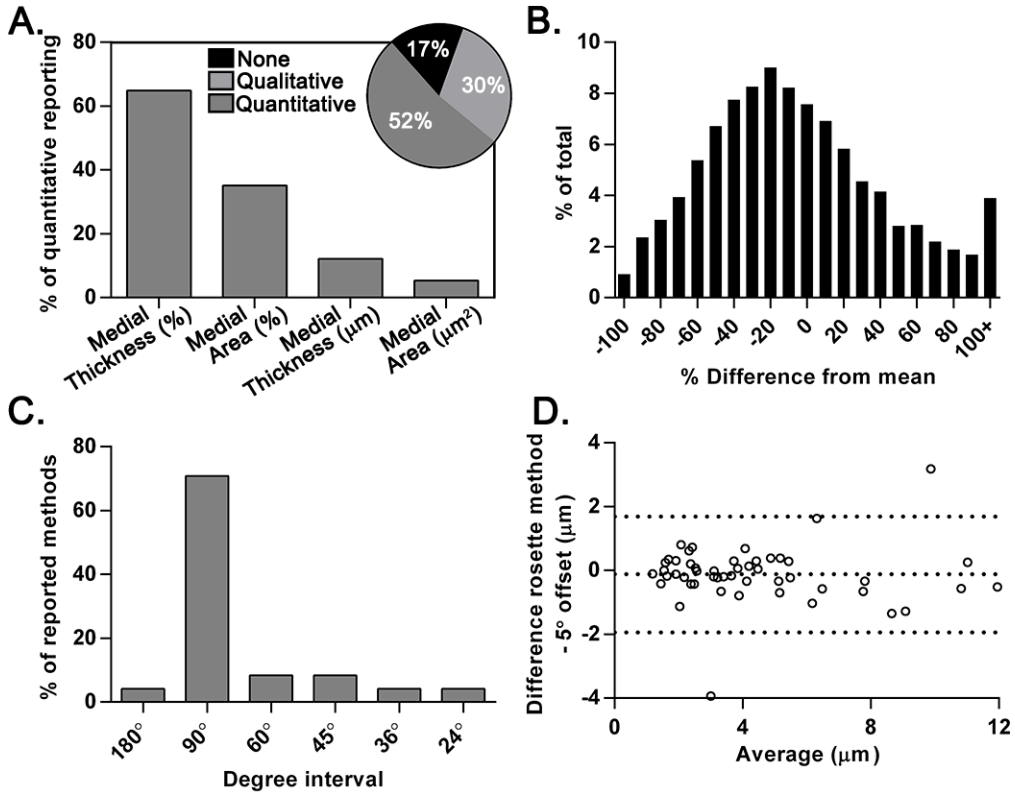

Figure 5. Current approaches to quantification of vascular remodeling.
Methods of wall thickness quantification were assessed in 141 journal articles related to pulmonary hypertension from the 2014 calendar year. (A) Relative frequency of reported measurements among articles quantifying medial thickening (pie chart shows percentage of all papers with quantitative, qualitative, or no assessment of medial thickening). (B) Histogram of the percent difference in wall thickness measurements of a single rosette segment versus its vessel average (n=50 vessels and 2917 segments). (C) Relative frequency of sampling intervals among journal articles which reported such in their methods (n=24 articles). (D) Bland-Altman plot of difference in wall thickness measurements sampled at 90° versus a 5° offset (n=50 vessels; dotted lines are mean ± 2SD).

2.3.4 Accurate measurement of wall thickness

The lack of a "gold standard" for wall thickness measurement necessitates the use of a theoretical approach to determining method accuracy. Before doing so, however, we can first think of the problem logically. As mentioned, based on the nature of the rosette method, we would expect it to overestimate the true wall thickness when a rosette segment intersects the wall

at an angle that is not perpendicular to the wall. In contrast, we would expect the boundary method to underestimate the true wall thickness, as the minimum distance from the outer wall boundary to the inner wall boundary will almost always (though not necessarily when gaps are present in the wall) be less than or equal to the true wall thickness. Therefore, we would expect the actual value of wall thickness to lie somewhere between the values obtained by the rosette and boundary methods. Plotting the agreement between the rosette and boundary methods and the skeleton method shows that the skeleton method possesses this intuitive characteristic of measuring wall thickness values less than those of the rosette method and greater than those of the boundary method (Figure 6A).

With this in mind, we can adopt a more rigorous approach to capture the mathematically correct measure of wall thickness. First, we can envision "sweeping" a line of variable thickness $T(x,y)$ to generate a closed loop in the form of a vessel cross section (Figure 6B). The path followed by the centroid (i.e. midpoint) of $T(x,y)$ is necessarily perpendicular to $T(x,y)$, and we can quantify the average wall thickness of the vessel, T_w, as the line integral of $T(x,y)$ over the centroid path divided by the arc length of the centroid path, or:

$$T_w = \frac{\oint_c T(x,y)dS}{L_c}.$$

Next, utilizing the Centroid Theorem from 4th-century mathematician Pappus of Alexandria [80], we obtain the critical property that $\oint_c T(x,y)dS$ is equal to the area of the wall A_w, which we can easily measure. Therefore, determination of the length of the centroid path L_c will allow us to obtain an accurate measure of T_w.

We hypothesized that the minimum skeleton provides an accurate estimate of the centroid path, which we can validate by estimating the line integral of $T(x,y)$ over the minimum

skeleton, $\oint_{sk} T(x,y)\,dS$, and comparing it to A_w; from Pappus' Centroid Theorem, the centroid path and minimum skeleton should be roughly equal if $\oint_{sk} T(x,y)dS \approx A_w$. To approximate $\oint_{sk} T(x,y)dS$, we made a series of wall-intersecting lines in the *x*-*y* plane at 1° intervals using the rosette method or an identical number of equally spaced measurements using the boundary method. We then set the *z*-value (height) of each point of intersection between the wall thickness lines and the skeleton to the length of the wall thickness line (Figure 6C). By summing the areas of the resulting quadrilaterals, we estimated the value of the line integral and compared it to the area of the wall. Estimates of the line integral based on the both the rosette and boundary methods correlated well (Pearson's $r > 0.98$) with the wall area (Figure 6D). Additionally, the line integral estimates and area showed limits of agreement of 28% below to 88% above using the rosette method and 30% below to 28% above using the boundary method (Figure 6E), consistent with our expectation that they overestimate and underestimate the wall thickness, respectively. Hence, the skeleton method approximates the centroid path and provides an accurate measurement of wall thickness in histological sections.

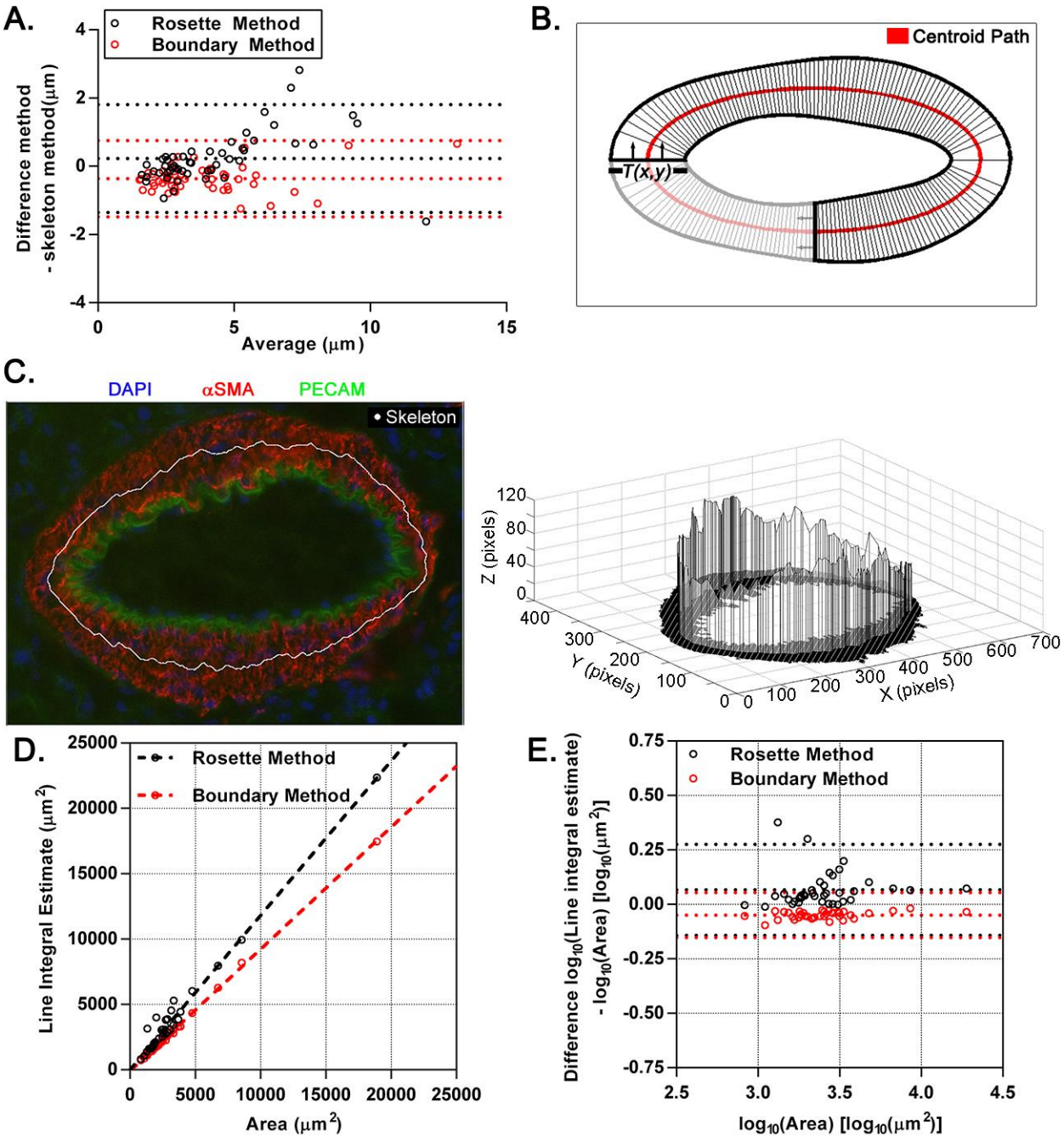

Figure 6. Accuracy of the skeleton method for wall thickness calculation.

(A) Bland-Altman plot of difference in rosette (black) and boundary (red) methods versus skeleton method (n=50 vessels in duplicate; dotted lines are mean ± 2SD). (B) Schematic of vessel wall area generated by sweeping a line of length T(x,y) to form a closed loop. (C) Schematic of a line integral estimate using the rosette method where the Z-axis corresponds to the wall thickness at the rosette's intersection with the skeleton. (D) Correlation of line integral estimates by the rosette (black) and boundary (red) methods with wall area (n=25 vessels; dashed lines are linear best-fits by least squares). (E) Bland-Altman plot of log10 difference in line integral estimate by the rosette (black) and boundary (red) method and wall area (n=25 vessels; dotted lines are mean ± 2SD).

2.3.5 Calculation of vessel diameter

Medial wall thickness is often viewed in the context of the external diameter (d_{ext}) of its corresponding vessel (internal diameter, d_{int}, and mid-wall diameter, d_{mid}, are frequently used, as well, but the distinction makes no difference for the current analyses). All calculations assume that the histological cross-section is perpendicular to the long axis of the vessel; while certainly not the case, we have no choice but to make this assumption. Typically, d_{ext} is measured using a corollary of the rosette method, whereby a series of lines is drawn through the center of the vessel's lumen and the mean of their distances between opposing outer wall boundary points is taken to be the diameter, d_{ros} (see Figure 3C). We compared our semi-automated measurements to manual measurements made using ImageJ at 90° intervals and found a negative bias of the VMI calculator compared to manual measurements (Figure 7A), perhaps indicating a tendency for manual measurements to measure diameter at the widest point of the vessel instead of through its lumen's centroid.

We can very easily justify the accuracy of our semi-automated calculations of d_{ros}. Notice that, in situations of suitable vessel concavity, if we were to integrate some continuous function $d_{ros}(\theta)$ in a polar coordinate system with θ ranging from 0 to π, we would simply have the area of the vessel, A_v (Figure 7B); in other words, d_{ros} is the diameter of a circle of area A_v, so the mean of discrete measurements d_{ros} is merely a rough estimate of $2\sqrt{A_v/\pi}$, and measurements taken at 5° intervals agree well with this approximation (Figure 7, C and D).

Whether d_{ros} is an appropriate method for diameter measurement depends on whether the histological image under consideration is assumed to accurately reflect the cross-sectional vessel shape. Cross-sectional vessel shape is dynamic and not necessarily circular [81, 82],

although it is often presumed to be so. However, in the case of the pulmonary vasculature, tissue fixatives are typically delivered to the airways at a positive pressure (often 25 cm H_2O), thereby subjecting the vasculature to a negative transmural pressure and collapsing the vessel walls. In this case and perhaps others, it is appropriate to assume a circular vessel cross-section for the measurement of vessel diameter. The wall skeleton length L_{sk} is independent of vessel shape (although still subject to elastic properties of the vessel) and thus representative of the circumferential length of the vessel wall at half its thickness; hence, we can infer that the external diameter of a given vessel in its circular form d_{sk} is equal to $L_{sk}/\pi + T_w$. To demonstrate the dependence of the rosette method on vessel circularity, we can assess its measurement with respect to a given vessel's index of circularity, Z, which we express as the ratio of 4π times the vessel area, A_v, to the square of the vessel perimeter, or

$$Z = \frac{4\pi A_v}{(\pi d_{sk})^2}$$

where $Z = 1$ corresponds to a perfect circle. By our earlier result that $d_{ros} \approx 2\sqrt{A_v/\pi}$, the ratio of d_{ros} to d_{sk} simplifies to

$$\frac{d_{ros}}{d_{sk}} \approx \sqrt{Z}$$

and we see that as Z approaches 1, the ratio of the d_{ext} calculations by the rosette method (at 5° intervals) to the skeleton method approaches equivalence and closely follows the square root of Z (Figure 7E). If the fifty vessels surveyed are representative of those measured in current practice, their mean circularity of 0.75 suggests that, under the assumption of circular vessel cross-sections, the rosette method underestimates d_{ext} by more than 13 percent.

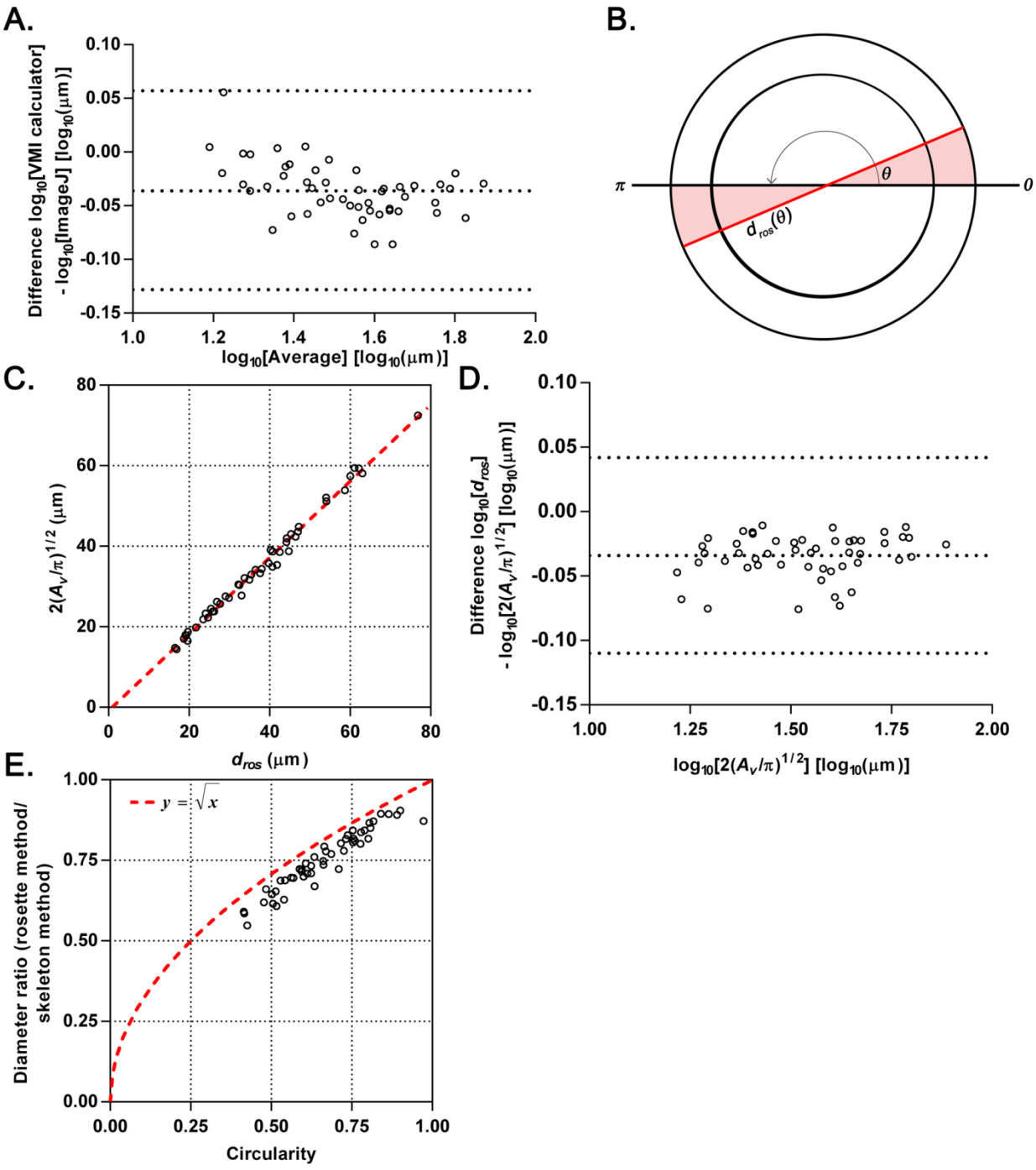

Figure 7. Vessel size using the rosette and skeleton methods.

(A) Bland-Altman plot of $\log_{10}$ difference in repeated $\boldsymbol{d_{ros}}$ measurements at 90° sampling interval using the VMI calculator or manual measurements (n=50 vessels; dotted lines are mean ± 2SD). (B) Schematic of relationship between $\boldsymbol{d_{ros}(\theta)}$ and vessel area, $\boldsymbol{A_v}$. (C) Correlation of external diameter calculated by the rosette method ($\boldsymbol{d_{ros}}$) and two times the square root of $\boldsymbol{2\sqrt{A_v/\pi}}$ (n=50 vessels). (D) Bland-Altman plot of $\log_{10}$ difference in $\boldsymbol{d_{ros}}$ and $\boldsymbol{2\sqrt{A_v/\pi}}$ (n=50 vessels; dotted lines are mean ± 2SD). (E) Ratio of external diameter calculated by the rosette method to that calculated by the skeleton method ($\boldsymbol{d_{ros}/d_{sk}}$) versus vessel circularity (n=50 vessels; dashed red line shows $\boldsymbol{y = \sqrt{x}}$).

2.3.6 Relationship between wall thickness and vessel diameter

Now that we have presented the best method for wall thickness measurement, we will discuss its interpretation in the context of data acquired from rat and mouse lungs after control or Sugen/hypoxia treatment. The most commonly reported metric of wall thickness is the so-called "medial index", which expresses T_w as a percentage of, typically, the external vessel diameter d_{ext} (see Figure 5A). The medial index stems from the "Law of Laplace," which relates transmural pressure P, wall thickness T_w, vessel diameter d, and circumferential stress, σ_θ, in thin-walled cylinders as $\sigma_\theta = Pd/(2T_w)$ [83, 84]. Then, based on the hypothesis that vessel wall thickness will change to maintain a constant circumferential stress, we have

$$100 \times 2T_w/d = P/c,$$

where c is a constant, and medial index can be interpreted as a surrogate for pressure.

However, as is widely known [85-87] although perhaps underappreciated, the relationship between medial index and mid-wall diameter is not flat, but rather has an initial phase of rapid decline followed by a plateau (Figure 8A). As may be deduced from data obtained through our literature survey, the shape of the medial index curve prompts researchers to limit their analyses to various ranges of vessel diameters (Figure 8A) and consequently abandon many data points.

The logarithm (base 10) of the wall thickness, meanwhile, has a lower distance correlation [76] with external diameter than the medial index, suggesting reduced statistical interdependence (Table 3) with vessel diameter in the ranges observed ($d_{ext} < 125\mu m$) regardless of organism or treatment condition (Figure 8B). In addition, $\log_{10} T_w$ follows a normal distribution, meaning its values can be conveniently compared by Students *t*-test (Figure

8C). Finally, it should be appreciated that any measurement of d_{ext} is subject to error involving vessel shape and slice orientation; because d_{ext} is excluded from its computation, $\log_{10} T_w$ is therefore less susceptible to measurement errors and assumptions than the medial index. Hence, the numerous advantages of $\log_{10} T_w$ over medial index led us to use this measure in our reporting.

Table 3. Distance correlation of medial index and $\log_{10}$(wall thickness) with external diameter.

		Medial index (%)	$\log_{10}(T_w)$
Rat	Naïve	0.5282	0.4369
	SuHx	0.6376	0.3536
Mouse	Naïve	0.8051	0.3763
	SuHx	0.4308	0.4132

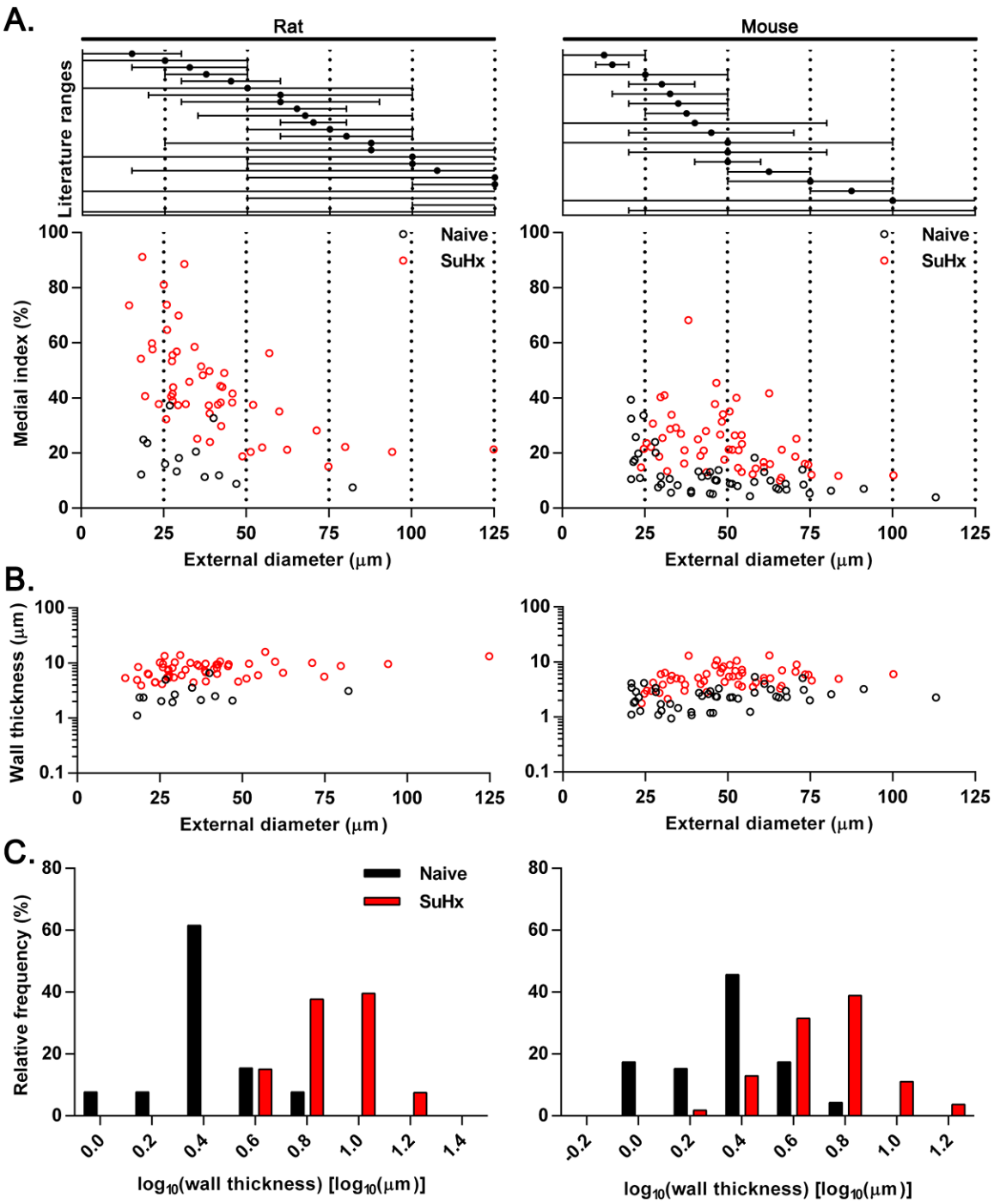

Figure 8. Relationship between wall thickness and vessel diameter.

Wall thickness and external diameter were calculated in lungs from Naïve (n=2 rats with 13 vessels, n=5 mice with 46 vessels) and SuHx-treated (n=3 rats with 53 vessels, n=6 mice with 54 vessels) animals. (A) Medial index (%) plotted versus external diameter. Upper panel shows external diameter ranges reported in 141 pulmonary hypertension journal articles from 2014. (B) $\log_{10} T_w$ plotted versus external diameter. (C) Histogram of relative frequency of $\log_{10} T_w$ values.

2.3.7 Assumptions of medial wall thickness measurements

Any discussion of wall thickness measurement methodologies would be incomplete without an acknowledgement of its inherent limitations. Quantification of medial thickening in histological sections is limited by two obvious factors: (*i*) the slice of the section is not necessarily perpendicular to the long axis of the vessel, and (*ii*) the shape of the vessel on cross-section, particularly if the vessels are non-distended, is not necessarily reflective of the vessel's *in vivo* shape. Historical studies have attempted to correct for offset angle [87] and vessel shape [88, 89] by applying various transformations with the assumption [82, 90] that vessels are circular in cross-section with uniform wall thickness. In essence, these methods trade one assumption for another.

An alternative approach is to measure the medial wall thickness of the vessels as they appear, as is most commonly done, and to do so accurately, which is possible using the skeleton method. Meanwhile, the sources of error should be acknowledged and understood, but their effects will be limited if cases and controls are prepared and analyzed in identical fashion.

In wall thickness measurements, the error comes from the offset angle θ of the vessel cross section with the plane perpendicular to the long axis of the vessel (Figure 9A). With the skeleton method, the percent error δ_w of the wall thickness measurement can be expressed as

$$\delta_w = 100 \times \left| 1 - \frac{\cos\theta}{a(\cos\theta - 1) + 1} \right|$$

where a is the fraction of the skeleton's length in the direction of the histological slice. With a ranging from 0 to 1, and θ ranging from 0 to 90°, we can see that δ_w ranges from 0 to 100% with an average of 25.2% if all combinations of a and θ are considered equally likely (Figure 9B).

For comparison, let us consider the other major metric of medial thickening used in the pulmonary hypertension literature (see Figure 5A), the percentage ratio of the medial wall area A_w to the total vessel area A_v. In contrast to the medial wall thickness, the percent medial area is independent of θ but has error in its assumption of vessel shape. If we define the circularity z as the ratio of $4\pi A_v/P_v^2$, where P_v is the vessel perimeter, then the percent error of the area ratio δ_a becomes

$$\delta_a = 100 \times \left|1 - \frac{z_{im}}{z_{act}}\right|$$

where z_{im} is the circularity observed in histological section and z_{act} is the actual circularity of the vessel. With z_{im} and z_{act} ranging from 0.5 to 1, based on our observations in mice (Figure 9C), δ_a ranges from 0 to 100%, with an average of 23.3% if all combinations of z_{im} and z_{act} are considered equally likely (Figure 9D). Because wall thickness and area have different sources of error, we recommend reporting each of their values, both of which are easily calculated in the VMI calculator.

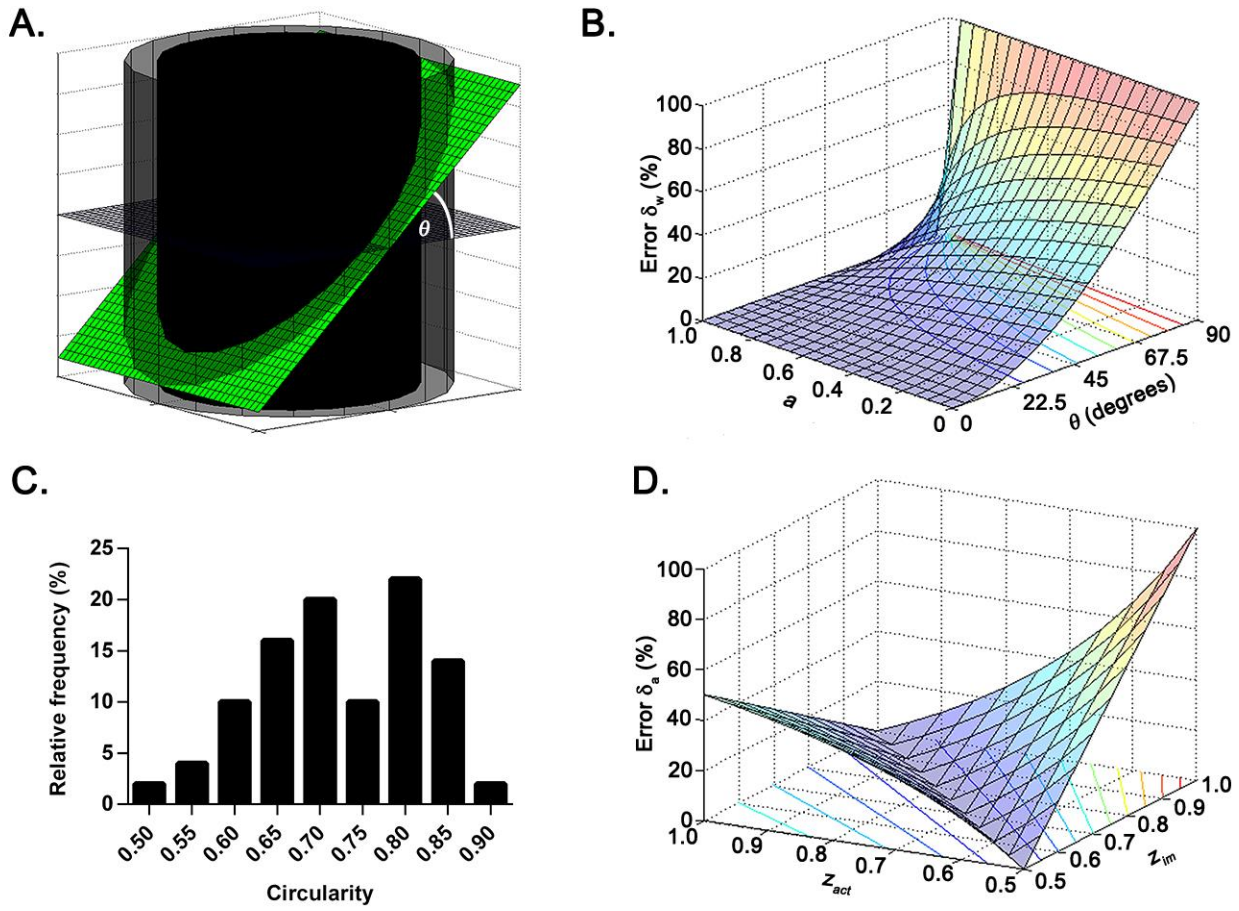

Figure 9. Limitations of wall thickness and percent medial area measurements.
(A) Schematic of histological section at offset angle $\boldsymbol{\theta}$ from the slice perpendicular to the long axis. (B) Percent error of wall thickness measurements $\boldsymbol{\delta_w}$ plotted versus the proportion of the skeleton length parallel to the direction of the histological slice, $\boldsymbol{a}$, and the offset angle $\boldsymbol{\theta}$ of the histological slice. (C) Relative frequency of circularities in sections from the lungs of naïve mice (n=46 vessels). (D) Percent error of percent medial area measurements $\boldsymbol{\delta_a}$ plotted versus the observed vessel circularity $\boldsymbol{z_{im}}$ and the actual vessel circularity $\boldsymbol{z_{act}}$.

2.3.8 Method use in Sugen/hypoxia rat and mouse models of pulmonary hypertension

Finally, we return to our original problem: the quantification medial thickening in the Sugen/hypoxia rat and mouse models of pulmonary hypertension (see Figure 3, A and B). After staining the medial component of lung sections with anti-αSMA, wall thickness was calculated by the skeleton method. The $\log_{10} T_w$ was significantly increased after Sugen/hypoxia treatment in rats and mice (Figure 10A). Likewise, the percentage ratio of medial area to vessel area was

significantly increased after Sugen/hypoxia treatment in rats and mice (Figure 10B). These data clearly demonstrate the utility of the VMI calculator in practice as an important complement to vascular research methodologies.

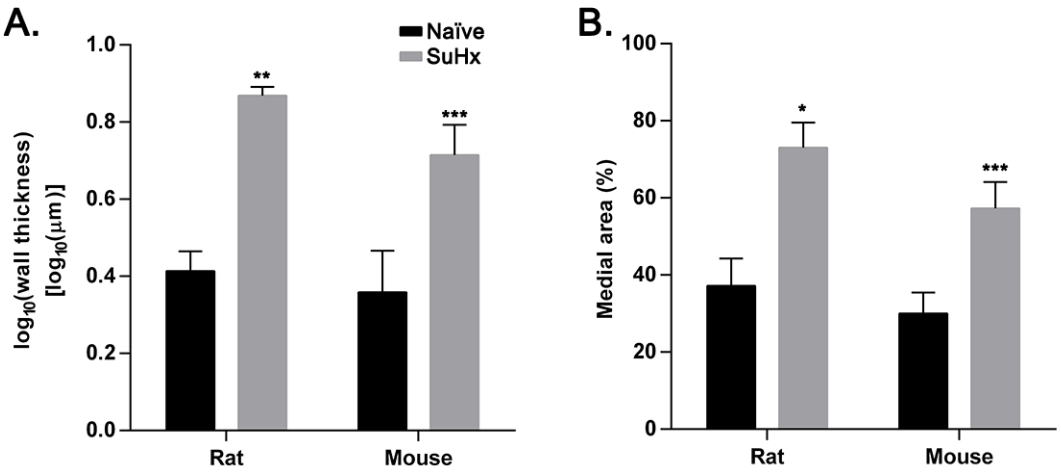

Figure 10. Increased $\log_{10}$(wall thickness) and percent medial area in Sugen/hypoxia-exposed rodents. Wall thickness and percent medial area were calculated in lungs from Naïve (n=2 rats with 6-7 vessels/rat, n=5 mice with 5-14 vessels/mouse) and SuHx-treated (n=3 rats with 16-21 vessels/rat, n=6 mice with 6-11 vessels/mouse) animals. (A) Average $\log_{10}$(wall thickness) among all vessels calculated using the skeleton method. (B) Average percent medial area among all vessels. Data are mean + SD. *P<0.05, **P<0.005, ***P<0.0005 by two-sided independent sample t-test.

2.4 DISCUSSION

In this report, we describe and validate a novel method for wall thickness calculation, the skeleton method, and demonstrate its superiority over previous approaches to thickness measurement. In addition, we present a new semi-automated software program, the VMI calculator, which calculates vessel wall thickness in histological images using this improved technique. Finally, we propose utilizing two methods for the interpretation of wall thickness measurements, the the $\log_{10}$(wall thickness) and the percent medial area, while demonstrating their use in Sugen/hypoxia rodent models of pulmonary hypertension.

Although the majority of the work presented relies on long-known theories and relationships, the best methods for wall thickness measurement have never been rigorously analyzed with modern image analysis tools. We suspect that the ongoing use of inferior methods is not due to lack of awareness of their shortcomings, but rather due to the lack of a superior and accessible alternative. Hence, we developed the skeleton method and made it freely-availably in the VMI calculator to both improve and accelerate the process of medial wall thickness calculation. While the skeleton method is more accurate than the rosette and boundary methods, it does have a drawback in that it returns a single value of wall thickness without capturing any variability; hence, we also included the rosette and boundary methods in the VMI calculator to return maximum and minimum wall thickness values for each vessel.

Based on the limitations and assumptions of various measurements, we proposed two quantities for comparisons: the $\log_{10}$(wall thickness) and the percent medial area. In our datasets, the $\log_{10}$(wall thickness) had three major advantages over the widely-used medial index in that (*i*) its values were normally distributed, (*ii*) they were relatively uncorrelated to external vessel diameter lengths ranging from 0 to 125 μm, and (*iii*) its calculation was independent of external diameter measurement, which is itself prone to error. The $\log_{10}$(wall thickness) is limited in its assumption that the histological slice is perpendicular to the long axis of the vessel, yet it is independent of vessel shape. In contrast, the percent medial area is independent of cross-section angle but assumes the accuracy of the vessel shape in cross-section. Because of their non-overlapping assumptions, we recommend the use of both metrics for the quantification of medial thickening.

In this paper, we focused our attention on the measurement of medial wall thickness; however, there is no reason that the techniques described cannot be applied to other layers or

subsections of the vessel wall. The VMI calculator can easily be used to quantify intimal and adventitial thickness. With this point in mind, we designed the VMI calculator to allow manual tracing of wall regions for measurement by the various methods. Manual tracing enables users to quantify not only high-contrast immunofluorescent images, but also immunohistochemical or simply histochemical stains.

While wall thickness calculations derived from histological sections are not a substitute for *in vivo* and myographic measurements, their ubiquity and persistence suggest that they will remain an integral part of vascular research. As such, it is crucial that they are measured appropriately; it is our hope and belief that the tools and analyses presented in this report will prompt investigators to uniformly adopt the best practices for vessel wall thickness calculation.

2.5 CONCLUSIONS

The skeleton method and the VMI calculator will be useful to investigators in the field studying medial thickening. Furthermore, they may assist with quantification of remodeling associated with dseases of the systemic circulation, airways, and more.

3.0 REGULATION OF TRAIL SIGNALING BY THE CARBOXYTERMINAL DOMAIN OF MACROPHAGE ELASTASE

3.1 INTRODUCTION

Lung cancer is the leading cause of cancer mortality in the United States, and despite recent progress in the management of many cancers, death rates among lung cancer patients remain alarmingly high [91]. Lung cancer is strongly correlated to a history of cigarette smoking [92], which is accompanied by damage and remodeling cycles that underlie the pathogeneses of other smoking-related diseases [93]. Matrix metalloproteinases (MMPs) are among the key endogenous mediators of these alterations in lung structure and function [94-96], and MMPs also play critical roles in tumor biology. While the overall effect of MMPs is to promote tumor progression [97], some MMPs – particularly MMP12 – appear to work for the host in inhibiting tumor progression [98, 99].

The MMPs constitute a family of 24 members with many common functional and structural characteristics, including an amino-terminal proenzyme domain and a zinc-containing catalytic domain. Most MMPs also contain a carboxy-terminal hemopexin-like domain, while some possess additional features such as a transmembrane domain [100]. In the context of malignancies, historical studies have focused on the MMPs' abilities to penetrate basement membranes and clear routes for tumor invasion [101, 102]. More recent evidence has shown an

increasingly diverse role for MMPs in cancer progression encompassing the release of matrix-bound growth factors [103], generation of chemotactic gradients [104], and modulation of tumor angiogenesis [98, 105, 106]. Hence, MMPs have garnered significant attention as potential targets for anti-cancer treatment [100, 107]. However, while MMP inhibitors showed therapeutic promise in murine models of cancer [108, 109], their efficacies in clinical trials have been surprisingly disappointing [110]. The failure of these drugs in human cancers is likely due to the diversity of MMPs, whereby certain MMPs consistently promote tumorigenesis, while others exhibit both pro- and anti-tumorigenic properties depending on the tumor type, disease stage, and cellular source [100, 111].

Macrophage elastase (*MMP12*) is one of the most highly upregulated genes in the lungs of cigarette smokers [112], yet its role in lung cancer remains controversial. Gene expression studies have shown significant associations between increased *MMP12* expression and risk of local recurrence and metastasis in non-small cell lung cancer [113, 114]. In contrast, promoter polymorphisms causing increased *MMP12* expression have been linked to prolonged survival in a cohort of lung cancer patients [115]. Meanwhile, murine models have shown a protective role for MMP12 against lung tumor growth [99] and metastasis [98] owing to its ability to generate the anti-angiogenic peptides endostatin (from type XVIII collagen) and angiostatin (from plasmin[ogen]) [116, 117]. Taken together, it is plausible that the anti-cancer effects of MMP12 impede the development or progression of lung cancer in human smokers.

We recently demonstrated a role for MMP12 that extends beyond its protein-cleaving function, as the conserved SR20 peptide in its C-terminal domain (CTD) directly enhances bacterial killing [118]. Hence, we hypothesized that MMP12 may also modulate cancer cell growth independent of its catalytic function. To explore the extra-proteolytic roles of MMP12 in

lung cancer, we subjected both lung cancer cells and primary lung cells to full-length MMP12 as well as fragments of both its catalytic domain and CTD. Through this *in vitro* model, we were able to delineate a novel mechanism by which the CTD of MMP12, through the activity of the SR20 peptide, suppresses tumor growth while sparing non-cancerous lung cells. Furthermore, we provide initial evidence supporting the efficacy of SR20 as a peptide chemotherapeutic in two murine models of lung cancer.

3.2 METHODS

3.2.1 Cell lines

A549 (CCL-185), MLE (CRL-2110), and LL47 (CCL-135) cells were obtained from and authenticated by the ATCC. 91T cells were kindly provided by Dr. Jill Siegfried who characterized these cells at the University of Pittsburgh [119]. Murine KW-857 cells were a generous donation from Dr. Kwok Wong who generated these cells from primary mouse tissue at Dana Farber Cancer Institute [120]. Cells were frozen into individual aliquots after no more than three passages, and thawed aliquots were each passaged for less than 6 months. Because the cells were obtained directly from the original source institutions and have undergone minimal passaging in order to eliminate the possibility of drift or contamination, these lines have not been re-authenticated.

3.2.2 Primary cells

Human bronchial epithelial cells (BEC) were a kind donation from Dr. Michael Myerberg at the University of Pittsburgh. Primary murine fibroblasts (PMF) were isolated as described previously [121]. These cells were cultured in Dulbecco's Modified Eagle Medium (DMEM, Invitrogen) with L-glutamine supplementation, 10% fetal bovine serum (FBS, Hyclone), and 50 U/mL of penicillin/streptomycin (Invitrogen). Human microvascular endothelial cells (HMVEC) were purchased from Lonza and grown in EGM2-MV culture media (Lonza).

3.2.3 Peptides

Human SR20 (sequence ARNQVFLFKDDKYWLISNLR) and SR20-GFP were synthesized at the University of Pittsburgh's protein core as described [118]. Human [*IgG1 Fc-FLAG*]-MMP12 C-terminal domain (CTD; sequence [*MGWSCIILFLVATATGVHSDKTHTCPPCPAPELLGGPSVFLFPPKPKDTLMISRTPEVTCVVV DVSHEDPEVKFNWYVDGVEVHNAKTKPREEQYNSTYRVVSVLTVLHQDWLNGKEYKCKVSN KALPAPIEKTISKAKGQPREPQVYTLPPSREEMTKNQVSLTCLVKGFYPSDIAVEWESNGQPE NNYKTTPPVLDSDGSFFLYSKLTVDKSRWQQGNVFSCSVMHEALHNHYTQKSLSLSPGKAAA NSSIDLISVPVDSRRPACKIPNDLKQKVMNHDYKDDDDK*]PALCDPNLSFDAVTTVGNKIFF FKDRFFWLKVSERPKTSVNLISSLWPTLPSGIEAAYEIEARNQVFLFKDDKYWLISNLRPE PNYPKSIHSFGFPNFVKKIDAAVFNPRFYRTYFFVDNQYWRYDERRQMMDPGYPKLITK NFQGIGPKIDAVFYSKNKYYYFFQGSNQFEYDFLLQRITKTLKSNSWFGC) was synthesized by GenScript. Recombinant human MMP12 catalytic domain (CAT; sequence REMPGGPVWRKHYITYRINNYTPDMNREDVDYAIRKAFQVWSNVTPLKFSKINTGMAD

ILVVFARGAHGDFHAFDGKGGILAHAFGPGSGIGGDAHFDEDEFWTTHSGGTNLFLTAV HEIGHSLGLGHSSDPKAVMFPTYKYVDINTFRLSADDIRGIQSLYGDPKENQRLP) was synthesized as described previously [122].

3.2.4 Cell culture

All cells were maintained in a humidified incubator at 37°C and 5% CO_2. Cells were treated with 20 μg/mL SR20 (in 10% Dimethyl sulfoxide, Sigma), 50 μg/mL CTD, or 100 μg/mL CAT, or 30-100 ng/mL recombinant human TRAIL (rhTRAIL, R&D Systems) for 1 hour in serum-free DMEM. After 1 hour, cells were washed in PBS and incubated in serum free media for 24-72 hours. For inhibitor experiments, cells were pre-incubated with 20 μM Z-IETD-FMK caspase-8 blocking peptide (BD Pharmingen), 20 μM Z-LEHD-FMK caspase-9 blocking peptide (BD Pharmingen), 3 ng/mL recombinant human TRAIL-R1 Fc chimera (rhDR4:Fc, R&D Systems), or 0.25 μg/mL mouse monoclonal [2E5] anti-TRAIL antibody (Abcam) for 30 minutes prior to the addition of SR20/CTD/CAT/rhTRAIL and remained for the hour of treatment. The anti-TRAIL antibody was reapplied to the media at 0.25 μg/mL following the 1 hour treatment period.

3.2.5 Thymidine incorporation

Cells were plated at a density of $5x10^4$ cells/well in 24-well plates and treated with CTD as described. After 1 hour, cells were washed in PBS and incubated in serum free DMEM containing 1μCi/mL [^{3}H] for 48 hours. Cells were washed with PBS, incubated with 5% trichloroacetic acid (Fisher Scientific) for 20 minutes and washed with deionized water. Cells

were dissolved in 200 mM of NaOH and transferred to scintillation vials. Disintegrations per minute (DPM) were measured on a Tri-carb 2100TR Liquid Scintillation Analyzer (Packard).

3.2.6 *In vitro* TUNEL staining

Cells were plated at a density of $5x10^4$ cells/well in 24-well plates and treated with CTD as described. After 48 hours, detached and adherent cells were collected, pooled, and transferred to glass slides by Cytospin (Thermo Fisher). TUNEL assays were performed on cells placed on slides using the ApopTag Plus Peroxidase Kit (Chemicon International) according to the manufacturer's instructions. The percentage of TUNEL-positive cells was counted under light microscopy.

3.2.7 Immunofluorescence

A549 cells were plated on tissue culture treated coverslips (Thermo-Fisher) in 24-well plates ($5x10^4$ cells/well), allowed to adhere for 16 hours, and transferred to serum fee media for 24 hours. Cells were treated with CTD as described, fixed with 2% paraformaldehyde and permeabilized with 0.1% Triton X-100. Cells were co-stained with Rhodamine-Phalloidin (Invitrogen), rabbit anti-MMP-12 (H-300; Santa Cruz), and Alexa Fluor 488-conjugated donkey anti-Rabbit-IgG (Invitrogen). Coverslips were mounted on microscope slides using VECTASHIELD HardSet Mounting Media with DAPI (Vector Laboratories) and imaged at 100X using an Olympus Fluoview 100 upright confocal microscope.

3.2.8 Luciferase assays

pRL-CMV, pGL2-Basic, and pGL2-Control were purchased from Promega. pGL2-TRAIL, with the 1523 base pairs upstream of *TNFSF10* cloned upstream of firefly luciferase, was a kind gift from Dr. B. Mark Evers[123]. A549 cells were plated in 96-well plates at a density of $2x10^4$ cells/well. After 24 hours, cells were co-transfected with 10 ng of pRL-CMV and 400 ng of either pGL2-Basic, pGL2-Control, or pGL2-TRAIL in Lipofectamine LTX PLUS (Invitrogen) and 20% v/v OptiMEM (Invitrogen) according to the manufacturer's protocol. 24 hrs after transfection, cells were treated with PBS or 50 μg/mL CTD for 24 hrs and luciferase activity was measured using the Dual-Glo Luciferase Assay System (Promega) according to the manufacturer's instructions.

3.2.9 Macrophage co-culture

Thioglycollate-stimulated peritoneal macrophages were resuspended in DMEM with 5% FBS and co-cultured with plated A549 cells at different concentrations ranging from $5x10^4$ - $15x10^4$ cells/well for 1-72 hours. At the appropriate time point, cells were washed thoroughly to remove nonadherent cells and macrophages.

3.2.10 Nuclear extraction

The cytoplasmic and nuclear fractions were isolated using NE-PER-Nuclear and Cytoplamic Extraction Kit (Thermo Scientific) according to the manufacturer's instructions.

3.2.11 Western blotting

Cells were collected using 0.05% Trypsin-EDTA (Invitrogen) and centrifuged at 1500 rpm for 10 minutes followed by 2 washes with PBS. Cell pellets were collected after centrifugation at 3000 rpm for 10 minutes and were lysed in 2X Cell Lysis Buffer (Cell Signaling). Total protein was quantified using the Dc Protein Assay (BioRad) according to the manufacturer's guidelines. 10-35 μg total protein were loaded on 4-15% Tris-HCl SDS polyacrylamide gels (BioRad) followed by transfer of proteins onto a nitrocellulose membrane. After blocking with 5% milk solution in TBS with 0.05% Tween 20, the blots were incubated with the primary antibody for 1 hour. The following antibodies and dilutions were used. Antibodies to AKT, Caspase-3, -8, and -9, Bad, phospho-Bad, Bcl-xL/Bcl-xS, NFκB, p44/42 MAPK, TRAIL, XIAP, c-FLIP, Lamin B1, and β-Tubulin were obtained from Cell Signaling Technologies. Antibodies to DR4, GAPDH, and Human IgG were obtained from Santa Cruz Biotechnology. After 3 washes with TBS plus tween 0.05% for 10 mins each, the blots were incubated with HRP-conjuguated secondary antibody (Santa Cruz Biotechnology) for 1 hr, followed by further washings. The signal was visualized using SuperSignal West Pico Chemiluminescent Substrate (Thermo Fisher).

3.2.12 Quantitative real-time PCR

Total RNA was isolated from cell lysates with the RNEasy Mini Kit (Qiagen) according to the manufacturer's instructions. RNA concentration was quantified on an ND-1000 spectrophotometer and 1.5 μg total RNA was subjected to reverse transcription (RT) using the High Capacity cDNA Reverse Transcription Kit (Applied Biosystems) according to the manufacturer's protocol. Quantitative real-time PCR (qPCR) was performed using the ABI 7300

Real-Time PCR System (Applied Biosystems) and TaqMan primers specific to TRAIL (Hs00921974_m1), DR4 (Hs00269492_m1), and GAPDH (Hs99999905_m1). Relative mRNA quantity was calculated using the delta-delta C_T method.

3.2.13 ELISA

Cells were plated in 6-well plates at a concentration of $2.4x10^5$ cells per well and the media was collected 48 hours after CTD treatment. The media was centrifuged at 1200xg for 10 minutes to pellet nonadherent cells, and the supernatant was analyzed for TRAIL using TRAIL ELISA kit (ab46117, Abcam) according to the manufacturer's instructions. The results were expressed as pg/ml of growth medium blanked to DMEM. The experiment was performed in triplicates and repeated 3 times.

3.2.14 Electrophoretic mobility shift assays (EMSA)

Genomic DNA (gDNA) was extracted from A549 cells using DNeasy Blood and Tissue Kit (Qiagen) per the manufacturer's protocol. gDNA was PCR-amplified on a BioRad C1000 thermal cycler using 5'-biotinylated primers (Invitrogen). Forward (F) and reverse (R) primers were as follows: Primer Set 1 (F) 5'-AAGGGCAGGAAGTGATGGTG-3', (R) 5'-AGGCTGGACAGGTAGGAAGT-3'; Primer Set 2 (F) 5'-TGGGTCCTGAATCTGAGGGT-3', (R) 5'-TGCACCCCTTATCTGCACTC-3'; Primer Set 3 (F) 5'-TCCTACCTGTCCAGCCTAAC-3', (R) 5'-TCAGGATCCATGCACCCCTT-3'; Primer Set 4 (F) 5'GGCTTGAGGTGAGTGCAGAT-3', (R) 5'-TTCTGGGTTCTGTGGCCTTG-3'. PCR products were separated by gel electrophoresis and purified using the QIAquick Gel Extraction

Kit (QIAGEN) according to the manufacturer's protocol. DNA binding was carried out with the LightShift Chemiluminescent EMSA Kit (Thermo Scientific) according to the manufacturer's protocol using a reaction mixture containing 28 pg/μL PCR product with or without 80 ng/μL CTD or an equimolar concentration of IgG Fc (R&D Systems). After 20 minutes incubation at room temperature, the reaction mixture was separated by gel electrophoresis on a 6% Tris-borate-EDTA (TBE) gel (Invitrogen), transferred to a Biodyne pre-cut modified nylon membrane (Thermo Scientific), and visualized using the Chemiluminescent Nucleic Acid Detection Module (Thermo Scientific).

3.2.15 Mice

C57BL/6J (WT) and *NU/J* mice were purchased from Jackson Laboratories and acclimated for 1 week prior to use. MMP12-deficient (*Mmp12*$^{-/-}$) mice on a *C57BL/6J* background (10 generation back-cross from *129/Sv*) were generated in our laboratory as described [124]. Lox-Stop-Lox *Kras*^{G12D} (*Kras*$^{LSL/G12D}$) mice were a generous gift from Dr. Tyler Jacks [125] and subsequently backcrossed onto a *C57Bl/6J* background for greater than ten generations. *Mmp12*$^{-/-}$ and *Kras*$^{LSL/G12D}$ were intercrossed to generate *Kras*$^{LSL/G12D}$:*Mmp12*$^{-/-}$ mice. All mice were housed in ventilated Plexiglas cages (one to four animals per cage) within a pathogen-free barrier facility that maintained a 12-hour light/dark cycle. Mice had free access to autoclaved water and irradiated pellet food.

3.2.16 Murine lung cancer models

For orthotopic lung A549 xenografts, pathogen free *NU/J* mice were intratracheally xenotransplanted at age 7-9 weeks with 10^7 A549 cells in 35 μL DMEM with 0.01M EDTA. 35 μL of 20 μg/μL SR20 or PBS was intratracheally instilled twice weekly for 10 weeks. For oncogenic *Kras* induction, tumors were induced in 8-week old $Kras^{LSL/G12D}$ and $Kras^{LSL/G12D}$:$Mmp12^{-/-}$ mice by administration of $5x10^6$ plaque forming units (pfu) adenoviral Cre recombinase (AdCre, University of Iowa). Seven weeks after tumor induction, mice received twice weekly dosing of 35 μL of 20 μg/μL SR20 or PBS by intratracheal instillation for 10 weeks. At the completion of treatment, mice were asphyxiated by CO_2 inhalation and lungs were inflated with 10% buffered formalin (Sigma-Aldrich) at 25 cm H_2O for 10 minutes.

3.2.17 Immunohistochemistry

Lungs were embedded in paraffin and 5 μm sections were cut and stained with hematoxylin and eosin (H&E). Tumor areas were expressed as a percentage of total lung areas on transverse sections from each lung lobe. TUNEL staining was performed using the Apoptag peroxidase in situ apoptosis detection kit (Millipore) according to the manufacturer's protocol. Ki67 staining was performed using a rabbit polyclonal antibody to Ki67 (Abcam) and the Vectastain Elite ABC Kit Rabbit IgG with DAB peroxidase substrate (Vector Labs) according to the manufacturer's protocol. TUNEL- and Ki67-stained sections were counterstained in 0.5% methyl green (Sigma). Images were captured at 10X or 60X on an Olympus Provis digital microscope system. Tumor areas and positive cells were quantified using NIS Elements BR3.0 (Nikon).

3.2.18 Statistics

Statistical analysis for all experiments was performed using GraphPad Prism 6 (GraphPad Software). Data are presented as mean ± SEM. Data were checked for normality by the Shapiro-Wilk test with an alpha of 0.05. Statistical comparisons between groups were made using two-sided independent-sample Student's *t* test. *P* values less than 0.05 were considered statistically significant.

3.3 RESULTS

3.3.1 MMP12 suppresses the growth of tumor cells through the SR20 peptide in its CTD

To examine whether MMP12 directly modulates cellular proliferation, we co-cultured A549 lung cancer cells with peritoneal macrophages from C57BL/6J wild-type (WT) or *Mmp12* null mutant (*Mmp12*$^{-/-}$) mice and measured proliferation by [^{3}H]-thymidine incorporation. Co-culture with WT macrophages led to a dose-dependent reduction in A549 proliferation at early (1-3 hr) and late (72 hr) incubation periods (Figure 11A), likely corresponding to the release of preformed and newly synthesized mediators, respectively [126]. Meanwhile, A549s co-cultured with *Mmp12*$^{-/-}$ macrophages proliferated normally (Figure 11B), suggesting that MMP12 is responsible for the reduced A549 proliferation seen in macrophage co-culture.

MMP12 is translated as a 470 amino acid protein consisting of a 9 kDa amino-terminal pro-domain that is cleaved upon activation, a 22 kDa catalytic domain, and a 23 kDa carboxy-terminal hemopexin-like domain (Figure 11C) [127]. To localize the anti-proliferative effects of

MMP12, we quantified the proliferation of A549 cells treated with either the catalytic (CAT) or carboxy-terminal domain (CTD) of recombinant human MMP12. While CAT had no effect on A549 proliferation, CTD caused a pronounced decrease in [^{3}H]-thymidine uptake compared to vehicle-treated controls. Further, the anti-proliferative effect was mimicked with the highly conserved CTD fragment SR20 (Figure 11D) that has previously been shown to enhance bacterial killing by macrophages [118].

To examine the breadth of CTD's anti-proliferative effects beyond A549 cells, we exposed a variety of primary and adenocarcinoma cells to CTD or SR20 and quantified proliferation by [^{3}H]-thymidine uptake. Adenocarcinoma cell lines included human A549 and 91T[119] cells as well as murine KW-857 cells [120], while non-transformed cells of both murine and human origin were considered, including primary murine fibroblasts (PMF), murine lung epithelial cells (MLE), human lung fibroblasts (LL47), human microvascular endothelial cells (HMVEC), and human bronchial epithelial cells (BEC). Consistently, CTD and SR20 stunted the proliferation of tumor cells but had no effects on non-transformed cells (Figure 11, E and F).

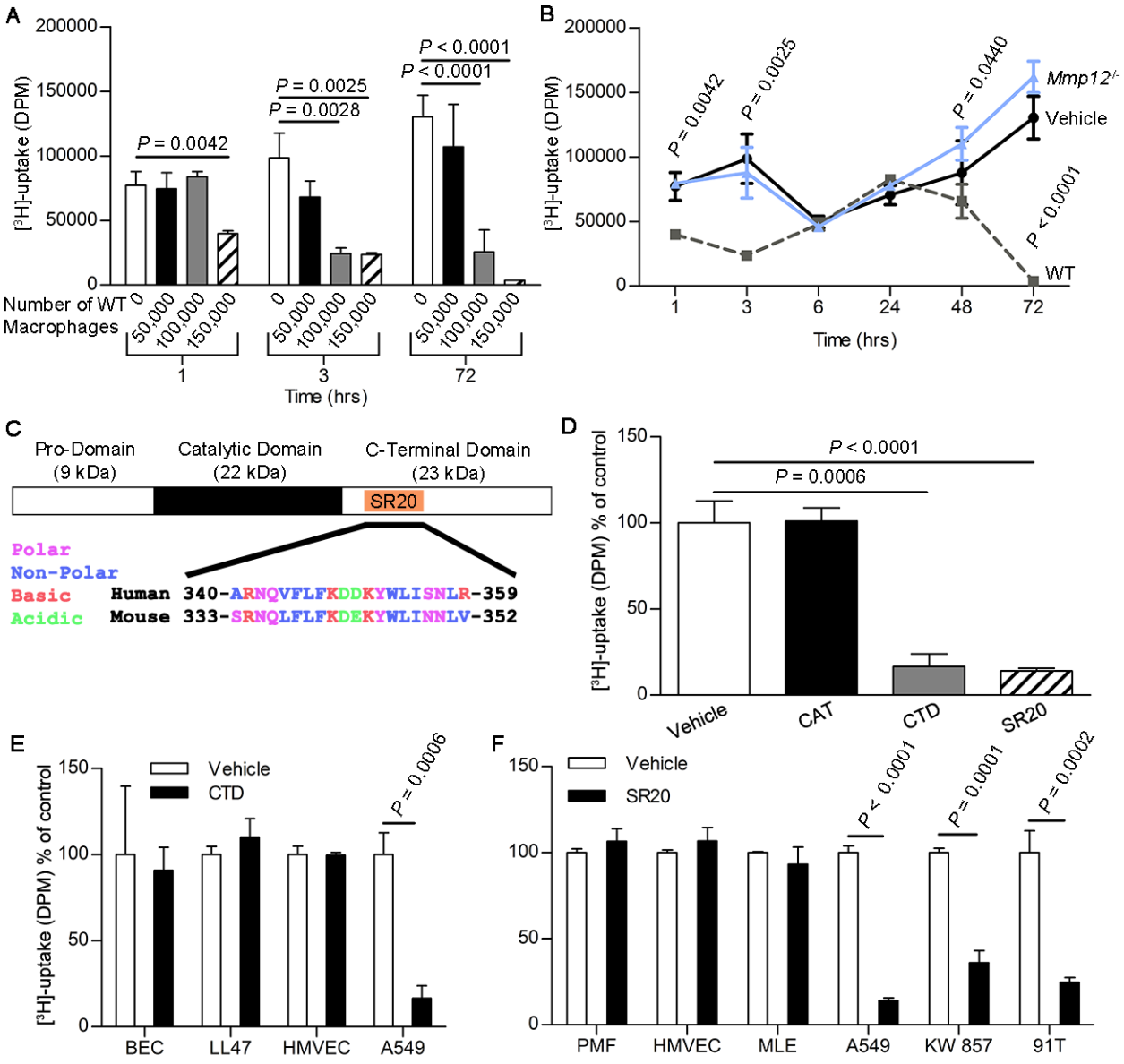

Figure 11. MMP12 CTD blunts A549 cell proliferation.

(A) A549 cells were cultured alone (control, *N*=4 replicates per time point) or co-cultured with 50-, 100-, and 150-thousand peritoneal macrophages (*N*=3 replicates per group per time point) from WT mice for 1, 3, and 72 hours and proliferation was measured by [^{3}H]-thymidine incorporation. (B) Time course from 1 to 72 hrs of [^{3}H]-thymidine incorporation in A549 cells in the absence of macrophages (control) or co-incubated with 150,000 WT or *Mmp12*$^{-/-}$ macrophages (*N*=3 replicates per group per time point). *P* values are *Mmp12*$^{-/-}$ versus control. (C) Primary structure of MMP12 consists of an N-terminal pro-domain, catalytic domain, and C-terminal domain containing a conserved SR20 peptide. (D) A549 cells were treated for one hour with 100 µg/mL CAT, 50 µg/mL CTD, or 20 µg/mL SR20 and proliferation was measured by [^{3}H]-thymidine incorporation in the 48 hours after treatment (*N*=3-4 replicates per treatment). (E) BEC, LL47, and HMVEC non-cancer cells and A549 cancer cell lines were treated with 50 µg/mL CTD for one hour and proliferation was measured by [^{3}H]-thymidine incorporation in the 48 hours after treatment (*N*=3-4 replicates per cell type per treatment). (F) PMF, HMVEC, and MLE non-cancer cells and A549, KW-857, and 91T cancer cell lines were treated with 20 µg/mL SR20 for 1 hour and proliferation was measured by [^{3}H]-thymidine incorporation in the 48 hours after treatment (*N*=3-4 replicates per cell type per treatment). Data are mean ± SEM. *P* values were calculated by two-sided independent sample *t* test.

3.3.2 MMP12 CTD traffics to the nucleus and initiates the transcription of TRAIL

Because the anti-proliferative effects of CTD were limited to cancerous cells, we suspected that CTD exerts its effects on cell growth through tumor necrosis factor-related apoptosis-inducing ligand (TRAIL, also known as TNFSF10), which has also been shown to exert specific effects on cancer cell viability [128]. TRAIL exists as both a type II transmembrane [128] and soluble (sTRAIL) polypeptide [129] whose binding to death receptors 4 (DR4) or 5 (DR5) triggers apoptotic cell death [130, 131]. Incubation of A549 cells with CTD or SR20 led to a significant increase in *TRAIL* and *DR4* mRNA (Figure 12A and Figure 13A) and protein (Figure 12B and Figure 13B) expression, as well as an 80-fold increase in sTRAIL protein (Figure 12, C and D) after 48 hours incubation. In agreement with a recent study [132], we found that CTD and SR20 traffic to the nucleus of A549 cells (Figure 12, E and F, and Figure 13C), suggesting that CTD may activate an anti-proliferative transcriptional program much like the anti-viral response triggered by MMP12's catalytic domain [132]. Indeed, CTD (Figure 12G), but not IgG Fc (Figure 13D) bound to multiple DNA fragments directly upstream of the TRAIL gene *TNFSF10* in electrophoretic mobility shift assays. To confirm the CTD-responsiveness of the TRAIL promoter, we transfected A549 cells with firefly luciferase-encoding plasmids pGL2-Basic, pGL2-Control, and pGL2-TRAIL, in which the luciferase gene is flanked at its 5' end by no promoter, the CMV promoter, or the 1523 base-pair region upstream of the *TNFSF10* gene [123], respectively. CTD treatment significantly increased the luciferase activity of pGL2-TRAIL-transfected cells while it had no effect on those transfected with either pGL2-Basic or pGL2-Control (Figure 12H).

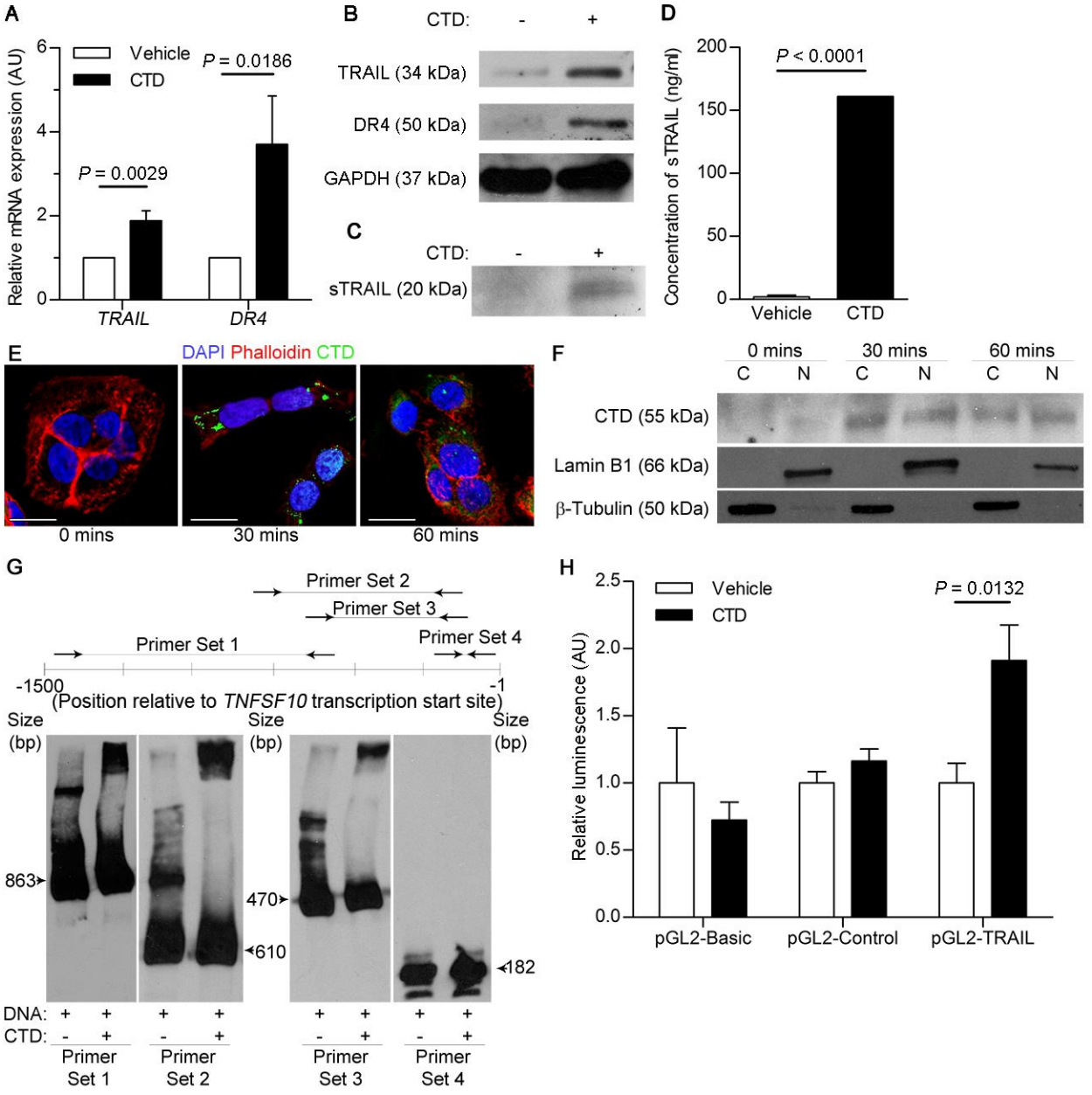

Figure 12. CTD induces the expression of TRAIL and DR4.

A549 cells were treated with 50 μg/mL CTD for 1 hour. (A) Relative mRNA expression of *TRAIL* and *DR4* normalized to *GAPDH* control at 5 hours after CTD treatment (*N*=4 means of independent experiments). (B) Representative western blot of TRAIL, DR4, and GAPDH endogenous control protein 48 hours after CTD treatment. (C) Representative western blot and (D) quantitative ELISA for sTRAIL in culture media at 48 hours after CTD treatment (*N*=3 means of independent experiments). (E) Confocal microscopy of CTD-treated A549 cells stained with rhodamine-phalloidin (red), 4',6-diamidino-2-phenylindole (DAPI; blue), and anti-MMP12-CTD (green). Images are representative of 3 independent experiments. Images were captured at 100X; scale bars are 10 μm. (F) A549 cytoplasmic (C) and nuclear (N) extracts were prepared at 0, 30, and 60 minutes after 50 μg/mL CTD treatment. (G) Representative EMSA of oligonucleotide fragments upstream of the *TNFSF10* transcription start site after 30 mins incubation with CTD. (H) A549 cells were co-transfected with pRL-CMV encoding *Renilla* luciferase and either pGL2-Basic, pGL2-Control, or pGL2-TRAIL encoding firefly luciferase and treated with 50 μg/mL CTD for 24 hours. Firefly luciferase activity was normalized to *Renilla* luciferase activity and expressed relative to

vehicle-treated controls (*N*=6 replicates per group). Western blots are representative of 3 independent experiments. Data are mean + SEM. *P* values were calculated by two-sided independent sample *t* test.

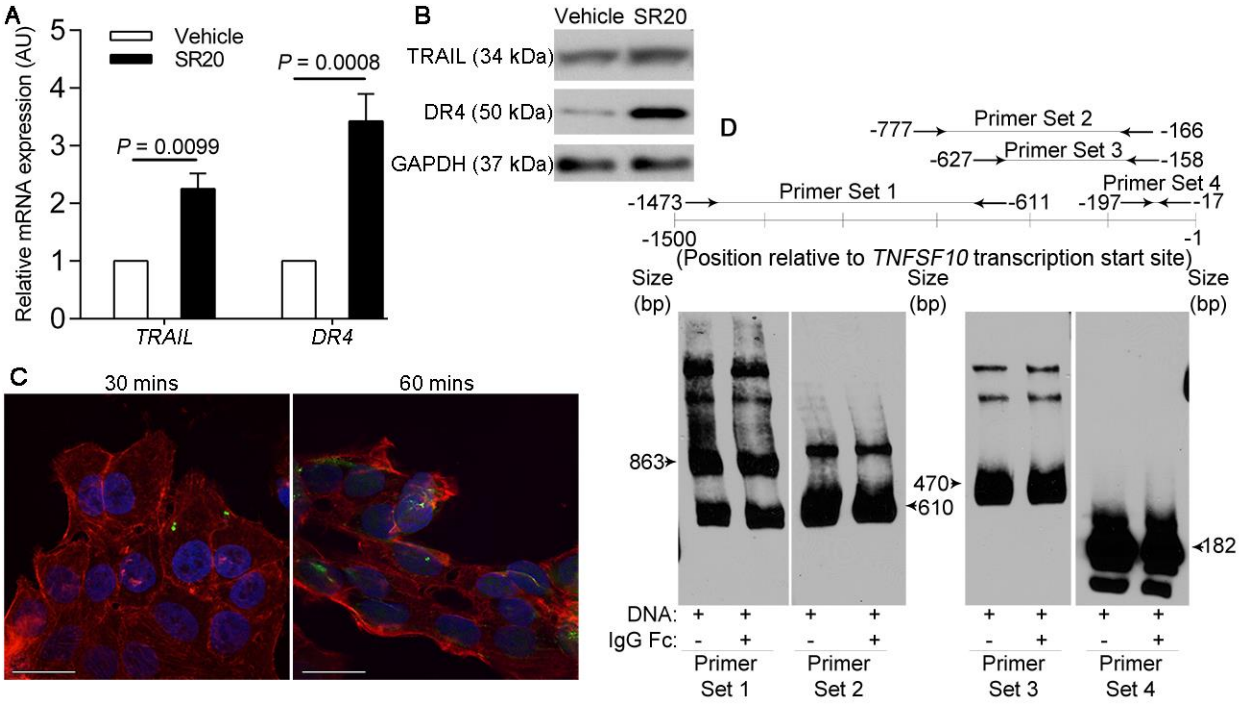

Figure 13. SR20 induces the expression of TRAIL and DR4.
A549 cells were treated with 20 μg/mL SR20 for 1 hour. (A) Relative mRNA expression of *TRAIL* and *DR4* normalized to *GAPDH* control at 5 hours after SR20 treatment (*N*=3 means of independent experiments). (B) Representative western blot of TRAIL, DR4, and GAPDH endogenous control protein 48 hours after SR20 treatment. (C) Confocal microscopy of SR20:GFP-treated (green) A549 cells stained with rhodamine-phalloidin (red) and 4',6-diamidino-2-phenylindole (DAPI; blue). Images were captured at 100X; scale bars are 10 μm. (D) Representative EMSA of oligonucleotide fragments upstream of the *TNFSF10* transcription start site after 30 mins incubation with IgG Fc. Western blots and EMSAs are representative of 3 independent experiments. Data are mean + SEM. *P* values were calculated by two-sided independent sample *t* test.

3.3.3 MMP12 CTD sensitizes tumor cells to TRAIL-mediated apoptosis

To determine whether induction of the TRAIL-DR4 axis was responsible for the decreased A549 proliferation following CTD treatment, we inhibited TRAIL signaling with a recombinant human DR4:IgG Fc chimera (rhDR4:Fc) during [^{3}H]-thymidine incorporation assays. rhDR4:Fc completely abolished the anti-proliferative effect of CTD (Figure 14A), and we confirmed rhDR4:Fc also abolished the anti-proliferative effect of SR20 (Figure 15A). Because TRAIL

exerts its anti-proliferative effects by initiating apoptosis [130], we hypothesized that CTD activates the apoptotic machinery of tumor cells. As expected, treatment of A549 cells with CTD (Figure 14B) or SR20 (Figure 15B), but not CAT, led to cleavage and activation of the apoptotic effector caspase-3 (CASP3) which was inhibited by pre-treatment with a neutralizing antibody to TRAIL (Figure 3C). Likewise, CTD treatment increased the percentage of TUNEL-positive cells (Figure 14, D and E), further indicating that CTD causes A549 cell apoptosis. Mirroring its effects on A549 cell proliferation, rhDR4:Fc blunted CASP3 cleavage induced by CTD (Figure 14F). TRAIL-bound DR4 initiates apoptotic cell death through caspase-8 (CASP8) [133], which can trigger apoptosis by direct cleavage of CASP3 [134] or intrinsic pathway signaling leading to caspase-9 (CASP9) activation [135-137] and subsequent CASP3 cleavage [136]. Previous reports indicated that type II pneumocytes, which share many properties with A549 cells [138], require the activation of both pathways in order to overcome anti-apoptotic mechanisms [139]; similarly, we found that CASP3 cleavage in CTD-treated A549 cells was blunted by antagonistic blocking peptides to either CASP8 (CASP8 BP) or CASP9 (CASP 9 BP; Figure 14G).

Resistance to TRAIL-mediated apoptosis has been a major obstacle in the therapeutic use of TRAIL, and A549 cells have been reported to be largely insensitive to recombinant human TRAIL (rhTRAIL) treatment [140]. To determine whether CTD treatment was modulating TRAIL-resistance pathways, we compared apoptotic mediators in A549 cells treated with either CTD alone, 100 ng/mL rhTRAIL alone, or CTD plus 30 ng/mL rhTRAIL. CTD treatment caused reduced levels of anti-apoptotic proteins phospho-Bcl-2-associated death promoter [141] (pBAD), B-cell lymphoma-extra large (BCL-XL), and X-linked inhibitor of apoptosis [142] (XIAP), along with increases in the pro-apoptotic proteins BAD and BCL-XS [143], all of which have been linked to TRAIL sensitivity [144-146] and were unaffected by rhTRAIL alone (Figure

14H). Likewise, CTD treatment decreased the levels of pro-survival proteins NFκB, AKT, and p44/42 MAPK linked to alternative TRAIL signaling in resistant cells [140, 147], while their levels were unchanged by rhTRAIL (Figure 14I). Meanwhile, CTD treatment decreased the expression of c-FLIP in A549 cells (Figure 14J), which functions in both TRAIL-resistance and the acquisition of pro-survival TRAIL-signaling phenotypes [140]. Taken together, these data -- and the upregulation of DR4 by CTD -- suggest that CTD sensitizes A549 cells to TRAIL-mediated apoptosis.

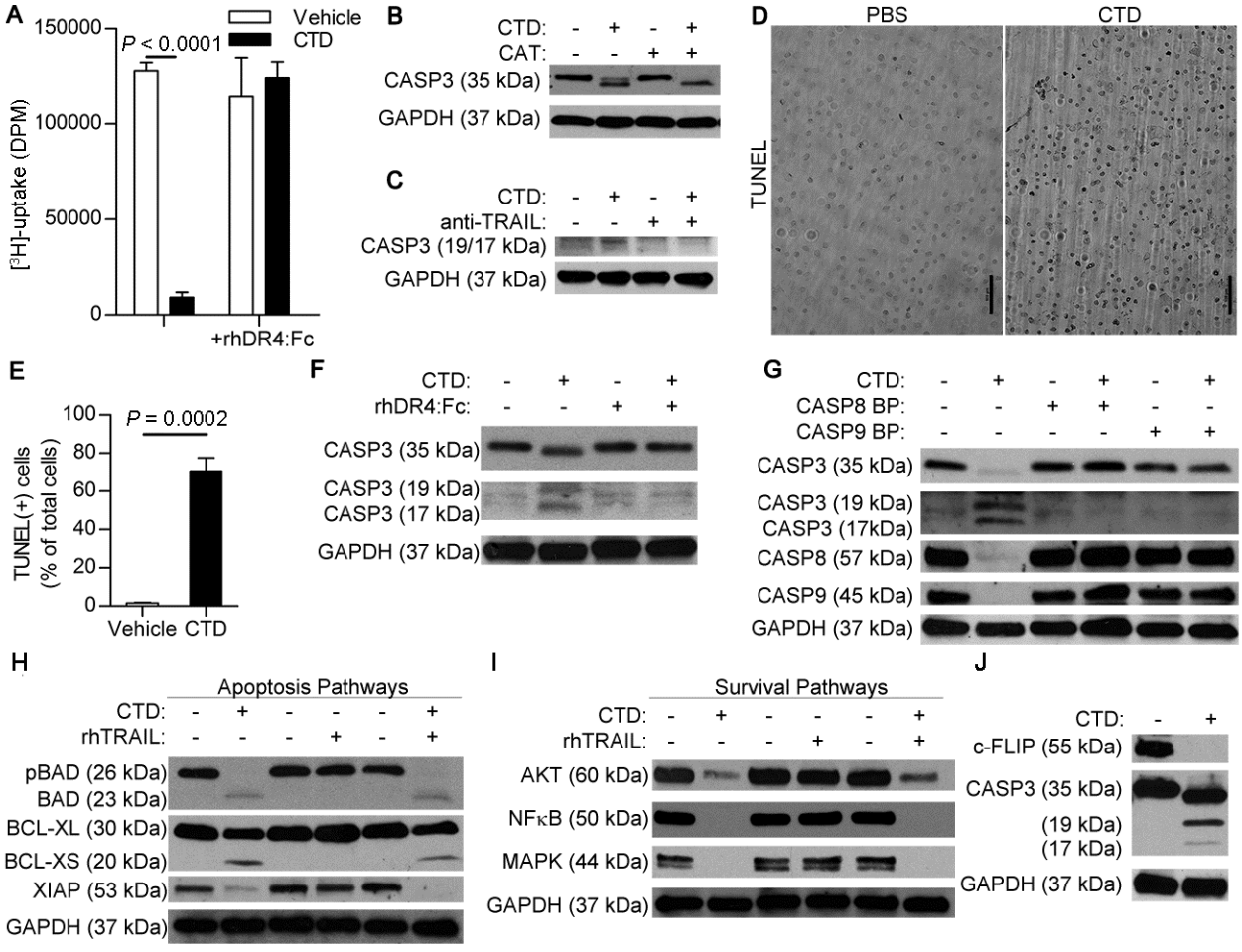

Figure 14. CTD induces TRAIL-dependent apoptosis and TRAIL sensitization.
A549 cells were treated with 50 mg/mL CTD for 1 hour and experiments were conducted 48 hours later. (A) A549 cells were pre-incubated in the absence or presence of rhDR4:Fc for 30 mins continuing into CTD incubation and proliferation was measured by [^{3}H]-thymidine incorporation (*N*=3-4 replicates per treatment). (B) A549 cells were treated with CTD or 100 μg/mL CAT. Representative western blot of CASP3 and GAPDH. (C) A549 cells were pre-incubated with or without anti-TRAIL antibody continuing into CTD incubation. Representative western blot of

CASP3 and GAPDH. (D) Representative images of vehicle and CTD-treated cells stained for TUNEL (brown; scale bars are 100 μm). (E) TUNEL-positive cells were quantified as a percentage of total cells (*N*=3 means of independent experiments). (F) Representative western blot for CASP3 and GAPDH in CTD-treated cells plus or minus rhDR4:Fc. (G) Representative western blot for caspase-3, -8, -9 and GAPDH protein in cells treated with CTD in the presence or absence of CASP8 BP or CASP9 BP. (H) A549 cells were treated with CTD, 100 ng/mL rhTRAIL, or CTD plus 30 ng/mL rhTRAIL. Representative western blot for phospho-BAD (pBAd), BAD, BCL-XL, BCL-XS, XIAP, and GAPDH. (I) Representative western blot for AKT, NFkB p50, p44/42 MAPK, and GAPDH. (J) Representative western blot for c-FLIP and CASP3 in cells treated with CTD. Western blots are representative of 3-6 independent experiments. Data are mean + SEM. *P* values were calculated by two-sided independent sample *t* test.

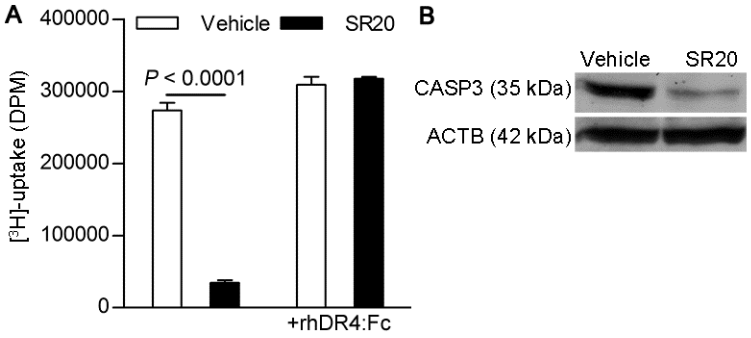

Figure 15. SR20 induces TRAIL-dependent apoptosis of A549 cells.
(A) A549 cells were pre-incubated in the absence or presence of rhDR4:Fc for 30 mins continuing into a 1 hour incubation with 20 μg/mL SR20 and proliferation was measured by [^{3}H]-thymidine incorporation in the 48 hours following treatment (*N*=3-5 replicates per group). (B) A549 cells were treated with 20 μg/mL SR20 protein was harvested 48 hrs after treatment. Representative western blot of CASP3 and ACTB endogenous control protein. Western blots are representative of 3 independent experiments. Data are mean + SEM. *P* values were calculated by two-sided independent sample *t* test.

3.3.4 SR20 is therapeutic *in vivo* in murine models of lung cancer

To confirm the importance of these findings *in vivo* and examine the feasibility of CTD as a chemotherapeutic, we instilled cancerous mice intratracheally with SR20, which contains the anti-tumor activity of CTD. The therapeutic efficacy of SR20 *in vivo* was first tested on an orthotopic A549 lung xenograft in athymic nude mice (*NU/J*). One week after A549 cell implantation, mice were given intratracheal instillations of SR20 or vehicle control 2 times per week for 10 weeks, and mice given SR20 experienced a 60% reduction in lung tumor area compared to vehicle-treated mice (Figure 16, A and B). In a second murine model of endogenous lung cancer (*Kras*$^{LSL/G12D}$), tumors were induced by intratracheal delivery of an adenoviral vector

containing Cre recombinase (AdCre) to trigger oncogenic *kras* expression [125]. Seven weeks after AdCre delivery, mice were begun on a regimen of either SR20 or vehicle control by twice weekly intratracheal instillation for 10 weeks. Interestingly, we observed that concurrent deletion of *Mmp12* (*Kras*$^{LSL/G12D}$:*Mmp12*$^{-/-}$) led to a significant increase tumor burden (Figure 16, C and D) adding to evidence of a physiological role for *Mmp12* in tumor surveillance [98, 99]. Treatment of *Kras*$^{LSL/G12D}$:*Mmp12*$^{-/-}$ mice with SR20 significantly reduced the overall tumor area by greater than 80% (Figure 16, C and D). In addition, tumors in SR20-treated mice harbored a greater percentage of apoptotic cells, as measured by TUNEL staining (Figure 16, E and F), while having fewer dividing cells as measured by Ki67 positivity (Figure 16, G and H). In summary, these data suggest that SR20 is an important physiological inhibitor of tumorigenesis with therapeutic potential in lung cancer.

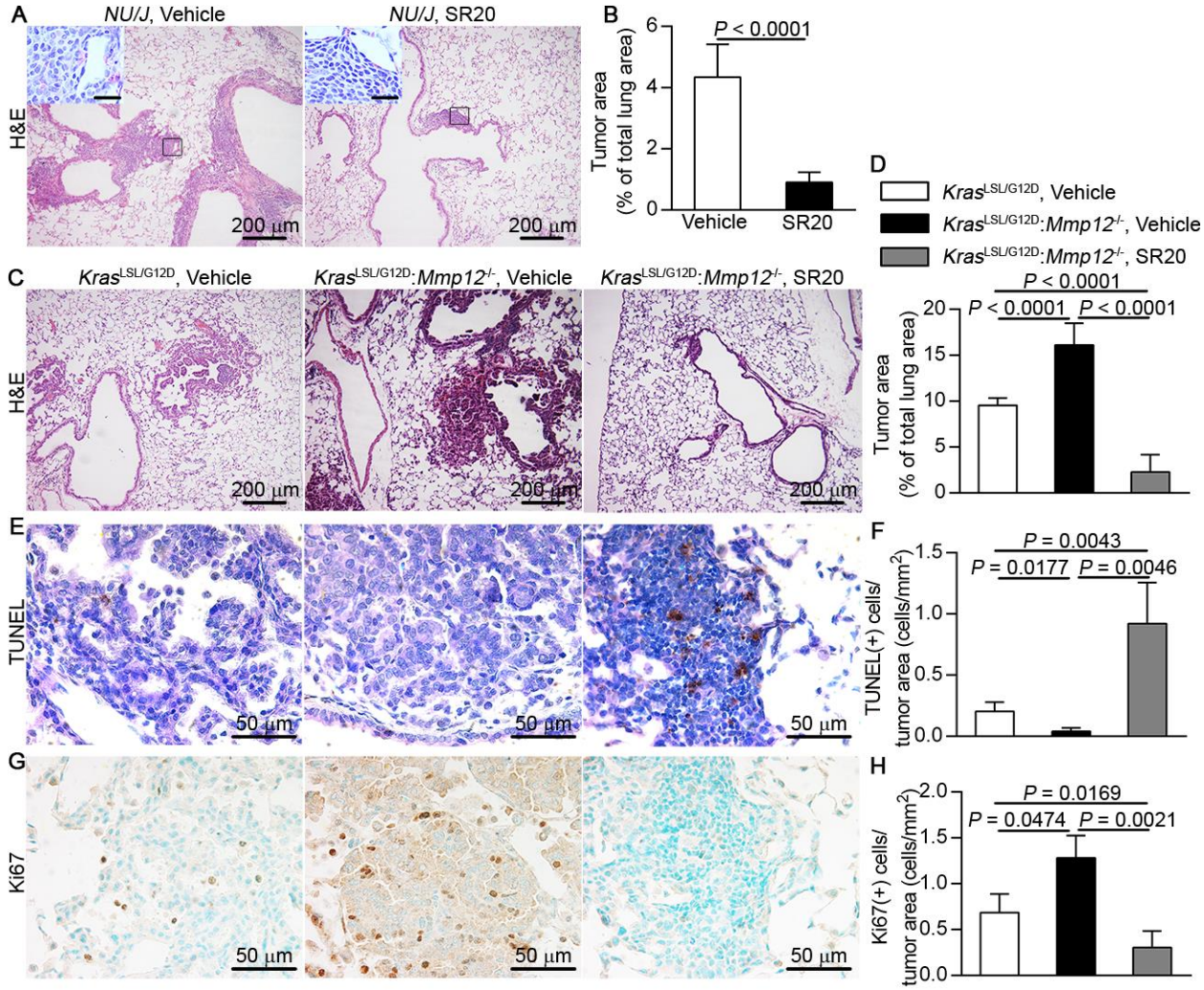

Figure 16. SR20 inhibits tumor growth.

Athymic nude mouse (*NU/J*) lungs were instilled with 10^7 cells 1 week later were instilled with vehicle control or SR20 twice weekly for 10 weeks. Mice were sacrificed at the end of the 10 week treatment period, lungs were inflated, and H&E sections were prepared. (A) Representative 10X H&E images of vehicle- and SR20-treated lungs. Boxes show inset area. Insets are 60X with scale bars of 20 μm. (B) Tumor area was measured as a percentage of total lung area (*N*=8 mice per group). Tumorigenesis was initiated in *Kras*$^{LSL/G12D}$ and *Kras*$^{LSL/G12D}$:*Mmp12*$^{-/-}$ by AdCre instillation. 7 weeks after tumor initiation, mice were treated intratracheally with vehicle control or SR20 twice weekly for 10 weeks. Mice were sacrificed at the end of the 10 week treatment period, lungs were inflated, and H&E sections were prepared. (C) Representative 10X H&E images of vehicle- and SR-20 treated lungs. (D) Tumor area was calculated as a percentage of total lung area (*N*=7-14 mice per group). (E) Representative 60X images of apoptotic cells stained with TUNEL. (F) Apoptotic cells were quantified as the number of TUNEL(+) cells per mm^2 of tumor area (*N*=3-5 mice per group). (E) Representative 60X images of dividing cells stained with Ki67. (F) Dividing cells were quantified as the number of Ki67(+) cells per mm^2 of tumor area (*N*=3-5 mice per group). Data are mean + SEM. *P* values were calculated by two-sided independent sample *t* test.

3.4 DISCUSSION

In this study, we present novel evidence for an endogenous mechanism of tumor defense. Using multiple lung cancer cell lines, we show that SR20, a conserved 20 amino acid region in the C-terminal domain of MMP12, invokes a potent tumoricidal program. By upregulating DR4 and its ligand, TRAIL, SR20 initiates an autocrine signaling loop leading to *in vitro* apoptosis of several lung cancer cell lines. Moreover, as appears to be the case with TRAIL, SR20 is cytotoxic to the tumor cell lines only while leaving non-cancerous lung cells intact. SR20 is effective in inhibiting lung tumor growth *in vivo* hence raising the possibility of a novel – and greatly needed – therapeutic agent for lung cancer.

Previously, studies from our laboratory [98] and others [99] showed that MMP12 inhibits tumor progression and metastasis through the generation of angiostatic peptides angiostatin and endostatin, this study elucidates a direct tumoricidal role for MMP12 via TRAIL-mediated apoptosis. This region has previously been shown to mediate intracellular killing of bacteria by macrophages via disruption of lipid membrane integrity [118], while full-length MMP12 has recently been shown to possess transcription-modulatory activity residing in its catalytic domain [132]. As we confirmed, the MMP12 CTD also traffics to the nucleus and binds DNA regions upstream of the TRAIL gene, *TNFSF10*. As CTD sensitizes TRAIL-resistant cells to its apoptotic signaling effects, it is likely that CTD regulates an entire set of target genes that may assist therapeutic efforts to overcome the characteristic resistance to TRAIL [140].

Our study is limited in that, although SR20 appears efficacious primary murine lung cancers, the efficacy of CTD and SR20 against primary human lung adenocarcinomas is not assessed. Human lung cancers are known to have varying sensitivities to TRAIL-mediated apoptosis which may include the activation of alternative pro-growth signaling pathways [148].

However, the ability of CTD and SR20 to initiate cell death in A549 cells, which are known to be resistant to TRAIL-mediated apoptosis [140], is promising in that it may have similar effects on resistant primary tumor cells. Furthermore, in light of preliminary evidence suggesting a transcriptional role for the MMP12 CTD, further benchtop studies will be required to fully understand the gene networks whose expression is modulated by CTD – networks that may or may not work in synergy with the mechanism described in this paper.

3.5 CONCLUSIONS

Nearly 25 years ago, the discovery of TRAIL brought great hope owing to its ability to induce apoptosis in cancer cells while sparing primary non-transformed cells [149]. The discovery of CTD's TRAIL-inducing and TRAIL-sensitizing effects suggests not only that TRAIL resistance can be overcome by endogenous mechanisms, but also that SR20 may represent an opportunity for a potent new chemotherapeutic agent.

4.0 THE CARBOXYTERMINAL DOMAIN OF MACROPHAGE ELASTASE IN PULMONARY VASCULAR REMODELING

4.1 INTRODUCTION

Vascular remodeling, as discussed (see 1.2), is a defining feature of pulmonary hypertension involving excessive proliferation and migration of vascular smooth muscle cells (SMCs) coupled with resistance to apoptosis [30].

As described earlier (see 3.3.2), TNF-related apoptosis inducing ligand (TRAIL, also known as TNFSF10) is a type II transmembrane protein [128, 150] which also exists in a soluble form (sTRAIL) [129]. Historically, TRAIL gained significant attention in the field of cancer research because it specifically induced apoptosis in tumor cells while leaving non-transformed cells intact [128, 150, 151]. TRAIL exerts its apoptotic effects in humans by signaling through death receptors 4 (DR4, also known as TNFRSF10A) [131] and 5 (DR5, also known as TNFRSF10B) [131, 152-154], while the rodent genome contains only a single death receptor orthologue of DR5 [155]. Classical TRAIL signaling through the death-domain-containing DR4 and DR5 [156] involves recruitment of the intracellular Fas-associated death domain (FADD) which, through its death-effector domain, recruits caspase-8 (Casp8) to initiate the assembly of the death-inducing signaling complex (DISC) [133].

Meanwhile, TRAIL can also bind to the transmembrane decoy receptors DcR1 (also known as TNFRSF10C) [130, 157] and DcR2 (also known as TNFRSF10D) [158-160], as well as the soluble protein osteoprotegerin (OPG) [161]. DcR1 and DcR2, which contain an absent intracellular domain and truncated death domain [156, 162], respectively, and the soluble protein OPG [163] are thought to antagonize TRAIL signaling by competitively inhibiting DR4 and DR5.

Although TRAIL is best known as an apoptosis-inducing ligand in transformed cells with little to no pro-apoptotic activity against non-transformed cells [128], a noteworthy exception was observed in systemic vascular smooth muscle cells (VSMCs), where TRAIL is expressed and appeared to induce VSMC apoptosis *in vitro* at high concentrations (≥100 ng/mL) [164, 165]. However, later studies found that lower concentrations of TRAIL paradoxically induced the proliferation of systemic VSMCs through increased ERK1/2 activation [166] and NFκB-dependent induction of IGF1R expression [167], consistent with the *in vivo* observation that administration of recombinant human TRAIL in diabetic *ApoE*$^{-/-}$ mice increased the stability and VSMC content of atherosclerotic plaques [168].

More recently, work by Lawrie *et al*. demonstrated that TRAIL is abundantly expressed in VSMCs of the characteristic plexiform lesions in human PAH [169] as well as in the media of remodeled pulmonary arteries in a Paigen diet-induced model of murine PH [170]. Mirroring its effects on systemic VSMCs, recombinant human TRAIL induced the proliferation and migration of human pulmonary VSMCs. Moreover, inhibition of TRAIL via gene deletion or neutralizing antibody prevented and reversed medial thickening in multiple rat and mouse models of PH [171]. Taken together, these studies demonstrate that TRAIL is an important effector of vascular

remodeling in PH; however, the upstream events responsible for induction of TRAIL in the setting of PH remain unknown.

We recently described a novel mechanism (see 3.0) whereby the carboxyterminal domain (CTD) of macrophage elastase (MMP12) induces the expression of TRAIL in tumor cells through a conserved 20 amino acid peptide known as SR20. Meanwhile, macrophages, the predominant source of MMP12 [132], are required for the development of hypoxia-induced PH in rodent models [172] and localize to sites of vascular remodeling [49]. In this report, we present evidence suggesting that the MMP12 CTD may be responsible for TRAIL-dependent pulmonary VSMC proliferation in PH.

4.2 METHODS

4.2.1 Primary cells

Primary human pulmonary artery smooth muscle cells (hPASMCs) were a kind gift from Dr. Elena Goncharova at the University of Pittsburgh School of Medicine. hPASMCs were grown in SmGM2 growth media (Lonza) supplemented with an Antibiotic-Antimycotic formulation of 100 U/mL penicillin, 100 μg/mL streptomycin, and 0.25 μg/mL Fungizone (Life Technologies) for no more than six passages.

4.2.2 Cell lines

RAW 264.7 (TIB-71) murine macrophages were purchased from the ATCC and grown in Dulbecco's Modified Eagle Medium (DMEM; Life Technologies) supplemented with 10% fetal bovine serum (Hyclone), 100 U/mL penicillin, and 100 μg/mL streptomycin (Life Technologies). Cells were frozen into individual aliquots after no more than three passages, and thawed aliquots were each passaged for less than 6 months. Because the cells were obtained directly from the original source institutions and have undergone minimal passaging in order to eliminate the possibility of drift or contamination, these lines have not been re-authenticated.

4.2.3 siRNA

hPASMCs were seeded in 24-well tissue culture dishes at a density of 50,000 cells/well in 500 mL SmGM containing antibiotic-antimycotic and incubated at 37°C for 3 hours. Silencer Select siRNA oligonucleotide to *TNFSF10* (siTRAIL; s16663) and Silencer Select Negative Control #1 (siCtl) were purchased from Life Technologies. Transfection was performed using HiPerfect transfection reagent (QIAGEN) at a final concentration of 30 nM according to the manufacturer's protocol. After 24 hours, CTD treatment and [^{3}H]-thymiding incorporation assays were performed as described (see 3.2.5).

4.2.4 Western blotting

Western blotting was performed as described (see 3.2.11). Antibodies to TRAIL, phospho-AKT (S473), AKT, phospho-ERK1/2 (T202/Y204), ERK1/2, GAPDH, and HIF1A were purchased from Cell Signaling Technologies.

4.2.5 Quantitative real-time PCR

qPCR was performed as described (see 3.2.12). *Mmp12* mRNA was quantified with a TaqMan primer (Mm00500554_m1, Life Technologies) and normalized to *Gapdh* mRNA (Mm99999915_g1, Life Technologies) by the delta delta C_T method.

4.2.6 Animals

Male C57BL/6J (WT) and *Mmp12*$^{-/-}$ mice were bred and raised as described (see 3.2.15). All animal experiments were performed in accordance with the Institutional Animal Care and Use Committee (IACUC) of the University of Pittsburgh School of Medicine.

4.2.7 Intratracheal instillation of SR20

Intratracheal instillation of SR20 was performed as described (see 3.2.16); briefly, male C57BL/6J mice received twice weekly dosing of 35 μL of 20 μg/μL SR20 or PBS by intratracheal instillation for 9 weeks beginning at 8 weeks of age.

4.2.8 Models of pulmonary hypertension

For high-fat diet-induced pulmonary hypertension, mice were fed an open diet consisting of 15% lipids/kcals (regular diet or RD) or 60% lipids/kcals (high-fat diet or HFD; Research Diets) for 20 weeks beginning at 8-12 weeks of age. For hypoxia-induced pulmonary hypertension, mice were housed in cages exposed to room air (Normoxia) or 10% O_2 (Hypoxia) for 9 weeks beginning at 8-12 weeks of age (see Table 4).

Table 4. Summary of pulmonary hypertension experiments in WT and *Mmp12*$^{-/-}$ mice.

	Normoxia (Room Air)	**Hypoxiax (10% O_2)**	**RD (15% Lipids)**	**HFD (60% Lipids)**
	(6 wks beginning @ 13 wks old)	(6 wks beginning @ 13 wks old)	(20 wks beginning @ 8 wks old)	(20 wks beginning @ 8 wks old)
	N	***N***	***N***	***N***
WT	8	8	8	8
***Mmp12*$^{-/-}$**	8	5	9	8

4.2.9 Hemodynamics

Right-ventricular hemodynamics were measured as described (see 2.2.3).

4.2.10 Histology

Mice were sacrificed following hemodynamic assessment. Lungs were inflated and fixed in 2% paraformaldehyde at 25 cm H_2O for 2 hours followed by 24 hours at 4°C in phosphate-buffered saline containing 30% sucrose (Sigma). Snap-frozen sections (7μm) were immunostained with a

Cy3-conjugated antibody to αSMA (Sigma, St. Louis, MO, USA) and 4',6-diamidino-2-phenylindole (DAPI; Sigma) to mark nuclei. Images of pulmonary arterioles were captured at 40X magnification using an Olympus Provis fluorescence microscope digital camera system.

4.2.11 Statistics

Statistical analysis for all experiments was performed using GraphPad Prism 6 (GraphPad Software). Data are presented as mean ± SD. Statistical comparisons between groups were made using two-sided independent-sample Student's *t* test, two-way ANOVA, or multiple *t*-tests with a false discovery rate (FDR) of less than 1%. *P* values less than 0.05 were considered statistically significant.

4.3 RESULTS

4.3.1 MMP12 is upregulated in macrophages grown in hypoxia

To determine the relevance of MMP12 in the context of pulmonary hypertension, we exposed RAW 264.7 murine macrophages to either normoxia (20% O_2) or hypoxia (0.5% O_2) for 48 hours. The hypoxic response was validated by upregulation of hypoxia-inducible factor 1-alpha (HIF1A) protein expression (Figure 17A). *Mmp12* mRNA expression was increased approximately two-fold by hypoxia exposure (Figure 17B), suggesting that it may play a role in the hypoxic environment associated with pulmonary hypertension.

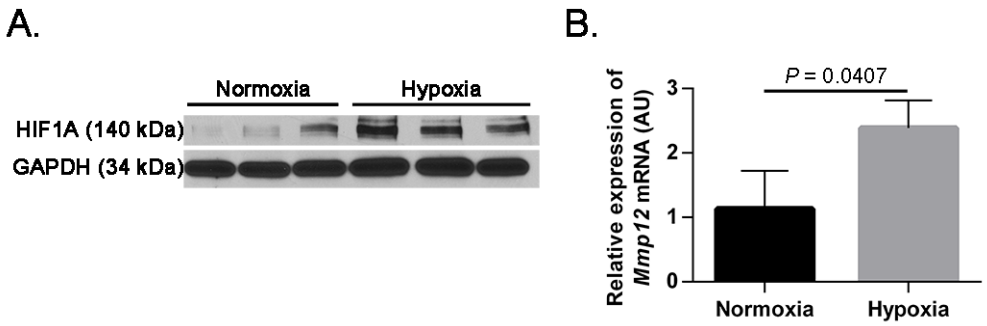

Figure 17. *Mmp12* is upregulated in murine macrophages exposed to hypoxia.
RAW 264.7 murine macrophages were grown in normoxia (20% O_2) or hypoxia (0.5% O_2) for 24 hours. (A) Hypoxia was confirmed by protein expression of HIF1A on Western blot. (B) *Mmp12* mRNA expression was measured by qRT-PCR and expressed relative to *Gapdh* endogenous control (N = 3/group). Data are mean + SD. P values were calculated by two-sided independent sample t-test.

4.3.2 MMP12 CTD triggers a TRAIL-dependent increase in hPASMC proliferation

To first examine whether the MMP12 CTD could upregulate the expression of *TRAIL* in pulmonary vascular smooth muscle – much like it does in A549 lung cancer cells – we exposed hPASMCs to CTD for 48 hours and measured *TRAIL* mRNA and protein expression by qPCR and western blot, respectively. CTD treatment led to a greater than two-fold increase in TRAIL mRNA expression (Figure 18A) and a corresponding increase in TRAIL protein expression (Figure 18B).

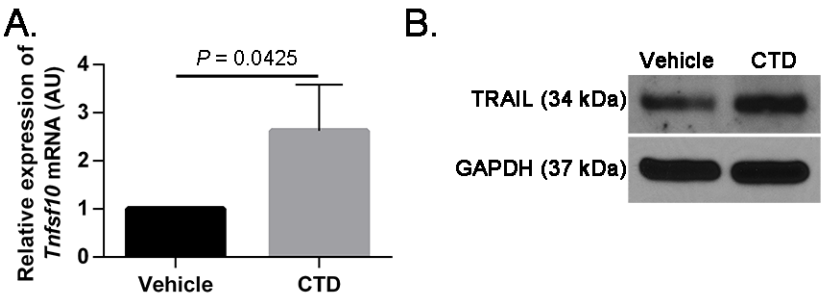

Figure 18. MMP12 CTD induces the expression of TRAIL in hPASMCs.
hPASMCs were treated with either PBS (Vehicle) or 50 μg/mL CTD for 1 hour followed by incubation in basal media containing 0.1% BSA. (A) RNA was harvested 24 hours after CTD treatment and *Tnfsf10* (*Trail*) and *Gapdh* mRNA were quantified by qRT-PCR (N = 3 means of independent experiments). (B) Representative western blot for TRAIL and GAPDH 48 hours after CTD treatment. Data are mean + SD. P values were calculated by two-sided independent sample t test.

Because TRAIL is known to increase the proliferation of vascular smooth muscle cells, we next measured hPASMC proliferation by [^{3}H]-thymidine uptake after treatment with the MMP12 CTD. As expected, the MMP12 CTD increased [^{3}H]-thymidine uptake by more than 60% (Figure 19A). Moreover, the increase in proliferation was abolished by siRNA-mediated knockdown of *TRAIL* (Figure 19, A and B), implying that the increased proliferation caused by the MMP12 CTD is TRAIL-dependent. As evidenced by increased phosphorylation of AKT and ERK1/2 (p44/42 MAPK) on western blot (Figure 19C), CTD appears to act at least partially through the AKT and ERK signaling pathways.

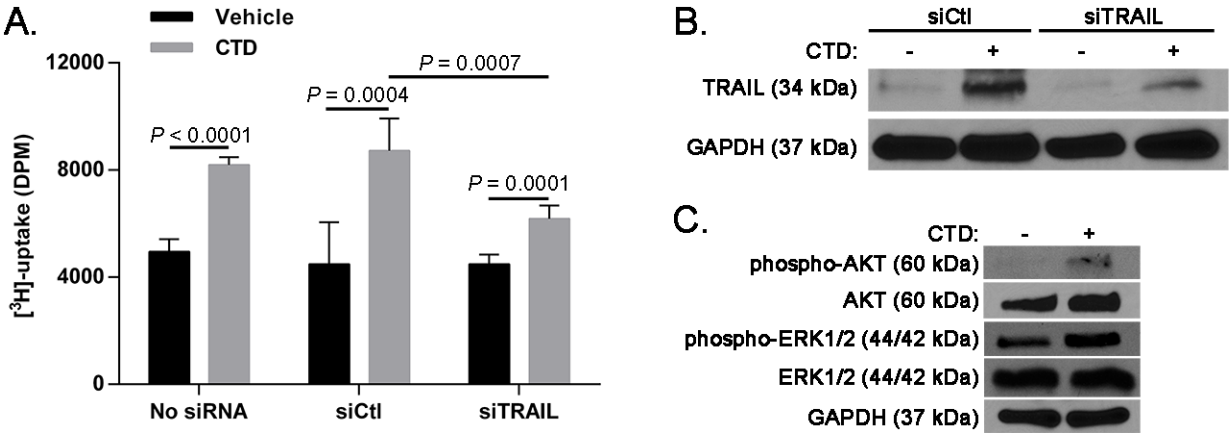

Figure 19. MMP12 CTD induces TRAIL-dependent proliferation of hPASMCs.
Following incubation for 24 hours in growth media alone (No siRNA) or growth media containing a control (siCtl) or TRAIL (siTRAIL) silencing RNA, hPASMCs were treated with PBS (Vehicle) or 0.5 μg/mL CTD for 1 hour. (A) hPASMC proliferation was measured by [3H]-thymidine incorporation in the 48 hours following CTD treatment (*N*=4-6 independent experiments/group). (B) Representative western blot of TRAIL and GAPDH protein at 48 hours after CTD treatment with siCtl or siTRAIL. (C) Representative western blot of phospho-AKT, AKT, phospho-ERK1/2, ERK1/2, and GAPDH protein at 48 hours after CTD treatment. Data are mean + SD. *P* values were calculated by two-sided independent sample *t*-test or two-way ANOVA as appropriate.

4.3.3 SR20 instillation may increase medial wall thickness *in vivo* but does not alter pulmonary vascular resistance

To determine whether the increased SMC proliferation triggered by the MMP12 CTD translates to *in vivo* models, we instilled C57BL/6J mice intratracheally with SR20 – the bioactive peptide

responsible for TRAIL upregulation by the CTD – twice weekly for 9 weeks beginning at 8 weeks of age. At the end of the treatment period, lungs were sectioned and stained for with an antibody to αSMA. The percent medial wall area and medial wall thickness was calculated using the VMI calculator as described above (see Figure 3C). SR20 treatment caused a modest but statistically significant increase in the percent medial wall area but did not affect medial thickness (Figure 20, A and B). In addition, instillation of SR20 had no effect on pulmonary vascular resistance (Figure 20B). Taken together, these data suggest that SR20 instillation may promote vascular remodeling *in vivo*.

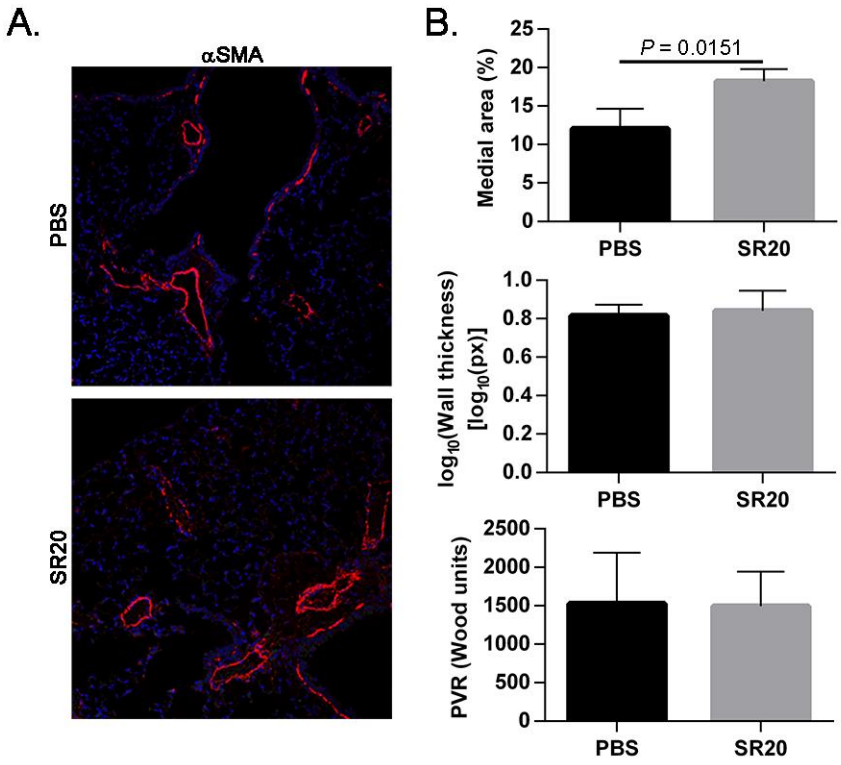

Figure 20. SR20 may induce medial thickening *in vivo*.

Male C57BL/6J received twice weekly 35 μL intratracheal instillations of PBS or 20 μg/μL SR20 for 9 weeks beginning at 8 weeks of age. (A) Representative images from PBS- or SR20-treated lungs stained for alpha-smooth muscle actin (αSMA, red) and 4',6-diamidino-2-phenylindole (DAPI, blue). (B) Medial area as a percentage of total vessel area, $\log_{10}$(wall thickness), and peripheral vascular resistance were quantified in PBS- and SR20-treated animals (*N*=3-5 mice/group). *P* values were calculated by two-sided independent sample *t*-test.

4.3.4 MMP12 is protective in hypoxia-induced pulmonary hypertension

Given the evidence that the MMP12 CTD induces pulmonary VSMC proliferation and, potentially, pulmonary vascular remodeling *in vivo*, we hypothesized that genetic deletion of *Mmp12* protects against pulmonary hypertension in mice. In male WT and *Mmp12*$^{-/-}$ mice, we utilized two murine models of pulmonary hypertension: (1) mice were fed either a regular (RD) or high-fat (HFD; 60% lipids/kcals) diet for 20 weeks or (2) mice were housed in room air (Normoxia) or 10% O_2 (Hypoxia) for 9 weeks beginning at 8-12 weeks of age. Surprisingly, *Mmp12*$^{-/-}$ mice were significantly more susceptible to chronic hypoxia-induced elevation in right ventricular systolic pressure (RVSP) than their WT counterparts (Figure 21A), and the two strains differed neither in the HFD-induced RVSP elevation (Figure 21A) nor in measures of body weight (Figure 21B), right ventricular hypertrophy (Fulton's index, Figure 21C), or pulmonary vascular resistance (PVR, Figure 21D).

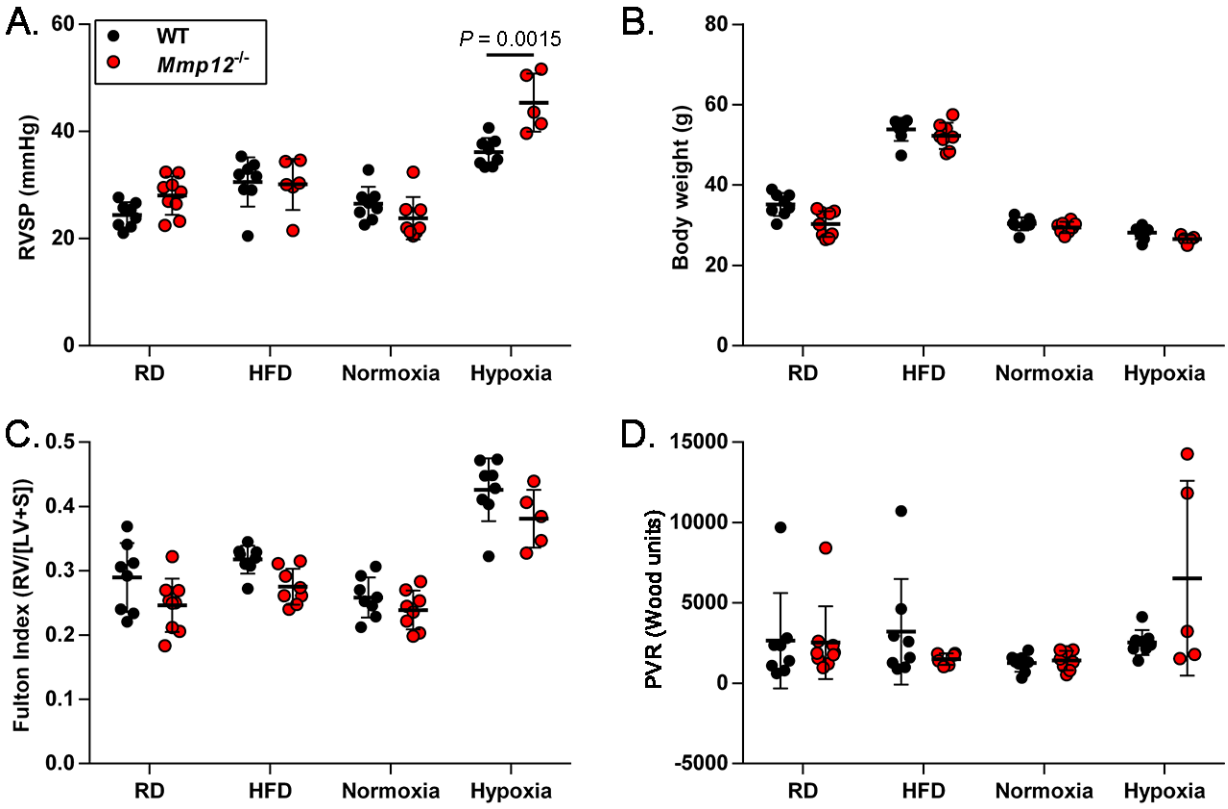

Figure 21. *Mmp12* is protective in murine hypoxia-induced pulmonary hypertension.
Male C57BL/6J (WT, black) or *Mmp12*$^{-/-}$ (red) mice were fed a regular (RD) or high-fat (HFD) diet for 20 weeks beginning at 8-12 weeks of age (*N*=6-9 mice/group). Alternatively, mice were housed in room air (Normoxia) or 10% O_2 (Hypoxia) for 9 weeks beginning at 8-12 weeks of age (*N*=5-8 mice/group). Hemodynamic measurements were obtained by terminal right-heart catheterization. (A) Right ventricular systolic pressure (RVSP), (B) body weight, (C) RV remodeling as assessed by Fulton index, and (D) pulmonary vascular resistance (PVR) were recorded. Data are mean ± SD. *P* values were calculated by two-sided independent sample *t*-test with false discovery rate less than 1%.

These data suggest that either (*i*) MMP12 CTD does not induce pulmonary VSMC proliferation *in vivo* in mice or (*ii*) the mitogenic effects of MMP12 on pulmonary VSMC proliferation are outweighed by other local or systemic effects in the HFD- and hypoxia-induced murine models of PH.

4.4 DISCUSSION

In this section, we describe a novel role for the CTD of macrophage elastase (MMP12) as a mitogen for human pulmonary VSMCs. We show that MMP12 is upregulated in macrophages grown under hypoxic conditions seen in PH, and that its CTD induces TRAIL-dependent proliferation of hPASMCs. Unexpectedly, however, genetic deletion of *Mmp12* in mice led to increased susceptibility to PH in a chronic hypoxia model, suggesting the MMP12 has a net protective effect on PH development.

The possible mechanisms behind MMP12-mediated protection against PH are numerous yet speculative at this point. TRAIL appears to promote the proliferation of VSMCs [166, 167], yet it may trigger apoptosis in endothelial cells [164]. Hence, the MMP12 CTD may prevent intimal hypertrophy even while it promotes medial thickening. Simultaneously, the catalytic domain of MMP12 is known to cleave plasmin(ogen) and type XVIII collagen and generate the anti-angiogenic peptides angiostatin [117] and endostatin [116], respectively, which may further inhibit intimal thickening and concomitant elevations in pulmonary vascular resistance.

The finding that *Mmp12*$^{-/-}$ mice have increased susceptibility to hypoxia-induced PH is even more surprising given what is known about its classical substrate, elastin, in pulmonary hypertension. Based on early studies [173, 174], it has been hypothesized that elastin degradation precedes pulmonary vascular remodeling, in part through the release of matrix-bound growth factors bFGF and tenascin-C [175]. In fact, previous studies have shown that serine elastase inhibitors and broad-spectrum MMP inhibitors induce apoptosis of hypertrophied medial walls in isolated hypertensive pulmonary arteries from rats [176]; likewise, systemic serine elastase inhibition was curative in a monocrotaline-induced PH model in rats [177]. In this context, our

findings suggest that any detrimental activity stemming from MMP12-mediated elastolysis is outweighed by other factors in the chronic hypoxia mouse model.

Mouse models are an additional factor complicating the study of MMP12 in PH; mouse models of PH, while attractive because of the wide availability of genetically-modified mice, do not develop the degree of vascular remodeling observed in rat models [30]; additionally, chronic hypoxia in the absence of Sugen (SU5416) is only thought to lead to minimal remodeling. Therefore, the relevance of MMP12 and the effect of its deletion/inhibition may be different in other models of PH [178].

In summary, MMP12 appears to be an attractive topic for further research in the context of PH. Its potentially conflicting roles – pathogenic elastin degradation and promotion of SMC proliferation versus speculated inhibition of intimal hypertrophy – may complicate its study, yet the use of multiple *in vivo* and *in vitro* models should help to clarify the role of MMP12 in PH.

4.5 CONCLUSIONS

From the above studies, it appears clear that MMP12 plays an important role in the pathogenesis of PH. However, the exact nature of this role remains unclear: the MMP12 CTD induces the TRAIL-dependent proliferation of hPASMCs, in contrast to its apoptosis-inducing activity against lung cancer cells (Figure 22).

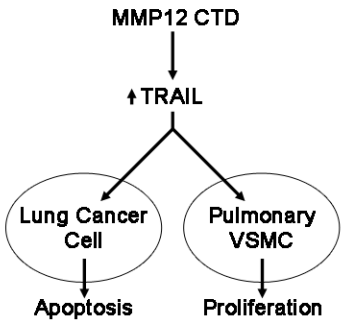

Figure 22. Proposed effects of the MMP12 CTD on lung cancer cells and pulmonary vascular smooth muscle cells (VSMC).

However, MMP12 has a net protective effect against chronic hypoxia-induced PH in mice. Further studies will be needed to elucidate the predominant PH-relevant mechanisms from MMP12's numerous activities.

5.0 GENOME-WIDE ASSOCIATION STUDY OF PULMONARY HYPERTENSION SUSCEPTIBILITY IN MICE

5.1 INTRODUCTION

Knowledge of the molecular events leading to pulmonary arterial hypertension (PAH) pathogenesis has exploded in recent decades; however, our understanding remains far from complete, as evidenced by the absolute dearth of medical interventions to prolong the survival of patients suffering from this deadly disease [179].

Human genetics-based approaches have contributed a wealth of knowledge regarding the pathogenesis of PAH by studying the co-occurrence of PAH cases in families (Familial PAH, or FPAH) [18]. These studies led to the identification of mutations in *BMPR2* as heritable disease genes [19, 20]. However, ~30% of FPAH cases lack pathogenic *BMPR2* mutations [180], and, while inherited in an autosomal dominant fashion, FPAH has a penetrance of only ~27%. Hence, PAH is a complex disease which is incompletely explained by known genetic factors.

Indeed, PAH cases with no clear heritable component (Idiopathic PAH, or IPAH) are approximately 15 times more common than FPAH [2, 181], and sporadic *BMPR2* mutations are observed in only 6-40% of IPAH cases [18, 182]. A recent genome-wide association study (GWAS) in humans identified a promising candidate gene in PAH pathogenesis, *CBLN2* [27], which induces vascular smooth muscle cells apoptosis and adds further evidence to the portrait

of PAH as a disease of excessive proliferation and diminished apoptosis of pulmonary vascular smooth muscle cells. However, PAH is also a systemic disease involving inflammatory cells, right ventricular dysfunction, and skeletal muscle abnormalities. In recent years, a new metabolic hypothesis has emerged to unite the multitude of abnormalities in the complex pathogenesis of PAH [183]. This theory has gained traction from, among others, observations in rodent models that (*i*) metabolic syndrome induces experimental PH [73, 170] and (*ii*) drugs that treat metabolic abnormalities also reverse experimental PH [64, 184].

In this study, we sought to leverage the power of GWAS with the feasibility of mouse models to identify novel candidate genes in PH pathogenesis as it relates to the metabolic syndrome. Murine GWAS have been employed to identify candidate genes associated with other pulmonary disorders including asthma [185] and lung cancer [186]. We hypothesized that a murine GWAS associating genomic single nucleotide polymorphisms (SNPs) with metabolic syndrome-induced PH would identify genes that are known to be involved in PH pathogenesis, as well as novel genes that may be related to PH. To induce disease, we utilized a high-fat diet-induced mouse model which has been shown to produce a robust PH phenotype in mice [73]. Here we report the results of the association of genomic single nucleotide polymorphisms (SNPs) with high-fat diet-induced changes in right ventricular maximum pressure (RV MaxP) in 36 inbred and wild-derived mouse strains.

5.2 METHODS

5.2.1 Animals

Male mice from 36 inbred and wild-derived strains (Table 5) were purchased from Jackson Laboratories (Bar Harbor, ME). All animal experiments were performed in accordance with the Institutional Animal Care and Use Committee (IACUC) of the University of Pittsburgh School of Medicine. Animals were housed within a pathogen-free barrier facility that maintained a 12-hour light/dark cycle in Plexiglas cages (one to four mice per cage) with free access to autoclaved water and irradiated pellet food. Animal health, weight, and overall behavior were monitored throughout the experiments.

Table 5. Mouse strains used in strain study

129S1/SvImJ	C57BL/10J	DBA/2J	NZB/BinJ
A/J	C57BL/6J	FVB/NJ	NZO/HiLtJ
AKR/J	C57BLKS/J	KK/HlJ	NZW/LacJ
BALB/cByJ	C57BR/cdJ	LG/J	PHK/PhJ
BALB/cJ	C57L/J	Ln/J	PL/J
BPN/3J	CAST/EiJ	LP/J	RIIIS/J
BTBRT+tf/J	CBA/J	MRL/MpJ	SJL/J
BUB/BnJ	CE/J	NOD/ShiLtJ	SWR/J
C3H/HeJ	DBA/1J	NON/ShiLtJ	WSB/EiJ

5.2.2 High-fat feeding

Male mice were fed an open regular (15% lipids/kcals) or high-fat (60% lipids/kcals; Research Diets), diet for 20 weeks beginning at 6-12 weeks of age.

5.2.3 Hemodynamics

Right-ventricular hemodynamics were measured as described (see 2.2.3).

5.2.4 Genome-wide SNP association

GWAS was performed as described previously [186]. Briefly, phenotypes were quantified as described and high-density mouse genotypes were obtained from the Center for Genome Dynamics at Jackson Laboratories [187, 188]. GWAS was performed using a univariate linear mixed model with Genome-wide Efficient Mixed Model Algorithm (GEMMA) [189, 190] where *P*-values reflected the strength of genotype-phenotype association.

5.2.5 Region analysis

Regions were constructed by beginning with a significant SNP ($P < 10^{-3}$) and iteratively adding flanking significant SNPs within ± 1 Mb until there were no significant SNPs in the 1 Mb upstream or downstream of the region.

Region *P*-values were calculated by the hypergeometric survival function based on the total number of SNPs, the number of SNPs in the region, the total number of significant SNPs ($P < 10^{-3}$), and the number of significant SNPs in the region. Regions with hypergeometric $P < 2.5\text{x}10^{-3}$ were considered significant. Mouse genes with exons contained wholly or partially within a significant region were considered candidate genes.

5.2.6 Network analysis

An interactome of human protein-protein interactions was kindly provided by Dr. Albert-László Barabási of Northeastern University [191]. Mouse-human orthologues were obtained from the Mouse Genome Database [192]. All network-based analyses were performed in the Python programming language. PH-related genes were curated as described previously [64, 193]. For a candidate node *v*, the (shortest path) betweenness centrality $C_B(v)$ was calculated in a subnetwork of the largest connected component *V* of PH-related genes with *v* added by

$$C_B(v) = \sum_{s,t \in V} \frac{\sigma(s,t|v)}{\sigma(s,t)}$$

where *s* and *t* are nodes in *V*, $\sigma(s,t)$ is the number of shortest paths between *s* and *t*, and $\sigma(s,t|v)$ is the number of shortest paths between *s* and *t* that pass through *v* [194]. Shortest paths were calculated by Dijkstra's algorithm. Betweenness centrality was normalized to its theoretical maximum based on the number of nodes *N* in *V* as $C_B(v)/(0.5(N-1)(N-2))$ [64].

5.3 RESULTS

5.3.1 Interstrain differences in high-fat diet-induced PH susceptibility

To quantify the effects of chronic high-fat feeding on pulmonary hemodynamics, we first stratified mice from 36 inbred or wild-derived strains into regular diet (15% lipids/kcals) or high-fat diet (60% lipids/kcals) beginning at 6-12 weeks of age. In order to eliminate the confounding effects of gender [195], only male mice were used in this study. After 20 weeks on their

respective diets, body weights were recorded and left- and right-ventricular (Figure 23) pressures were measured by terminal cardiac catheterization.

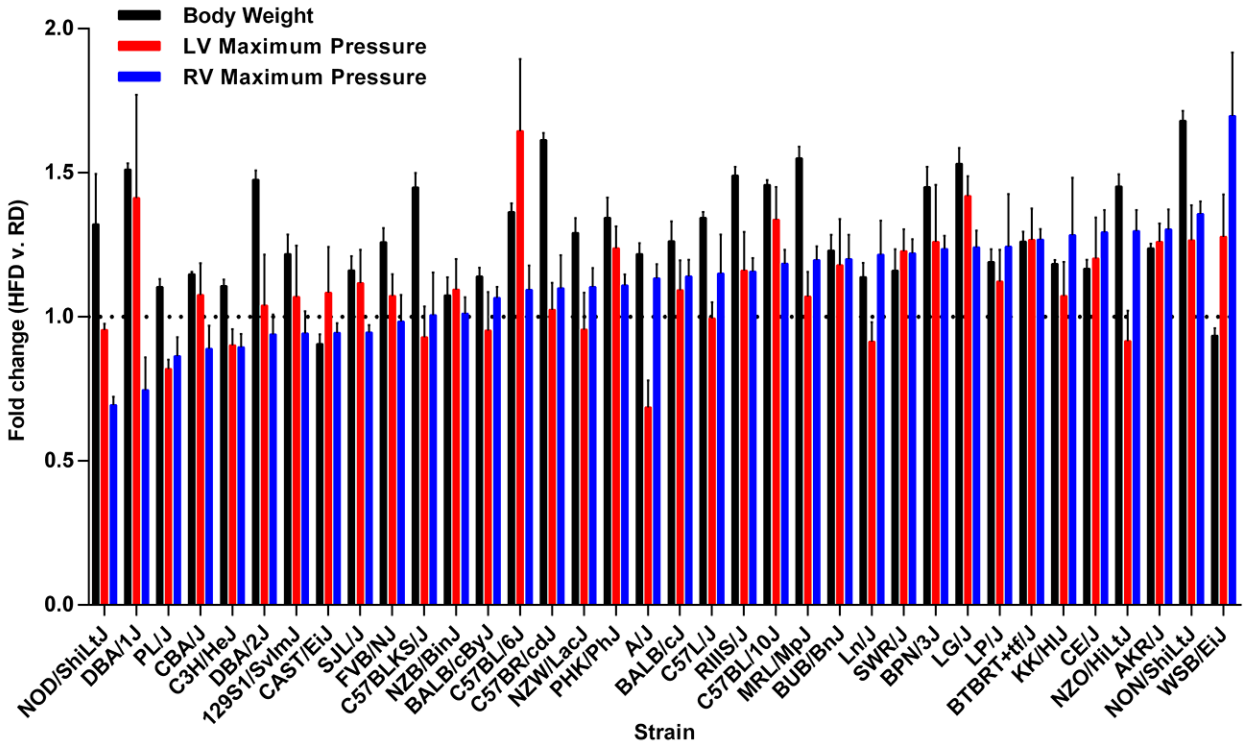

Figure 23. Fold change in RV maximum pressure.
36 strains of inbred or wild-derived mice were fed with a regular (RD) or high-fat (HFD) diet for 20 weeks beginning at 6-12 weeks of age (*N*=3-8 mice/diet per strain). Left- (LV) and Right-ventricular (RV) hemodynamics were measured by terminal catheterization. Fold change in body weight, LV Maximum Pressure, and RV Maximum Pressure was calculated as the HFD value divided by the average RD value. Data are mean ± SD.

5.3.2 Genome-wide SNP association identifies regions associated with right-ventricular hemodynamics

Following data acquisition, we identified single nucleotide polymorphisms (SNPs) associated with each of 48 phenotypes – encompassing weight, ventricular remodeling, and left- and right-sided hemodynamics – by Genome-wide Efficient Mixed Model Association (GEMMA; see Appendix A) [189, 190]. To account for the influence of baseline phenotypes on high-fat phenotypes, we expressed each quantitative phenotype on high-fat diet as a fold change from the

mean regular diet value of its strain. Reasoning that important SNPs were likely to cluster together in chromosomal regions, we constructed genomic regions of interest for each phenotype by combining 1 megabase (Mb) flanking segments of significant SNPs ($P < 10^{-3}$). Significant regions were defined as regions that were enriched for significant SNPs by hypergeometric enrichment with $P < 2.5x10^{-3}$. We then developed a list of candidate genes based upon their presence in a significant region.

To filter our initial list of candidate 1,511 candidate genes associate with RV maximum pressure (RV MaxP) genes, we excluded genes that were associated with either body weight, LV MaxP, or LV end-systolic pressure (LV ESP), reasoning that these genes could function upstream of the molecular events of most interest to our study. Meanwhile, we excluded genes that were not also associated with RV ESP, reasoning that genes associated with both phenotypes were less likely to be false positives. Using this method, we were able to roughly halve our initial list to 880 candidate genes (Figure 24).

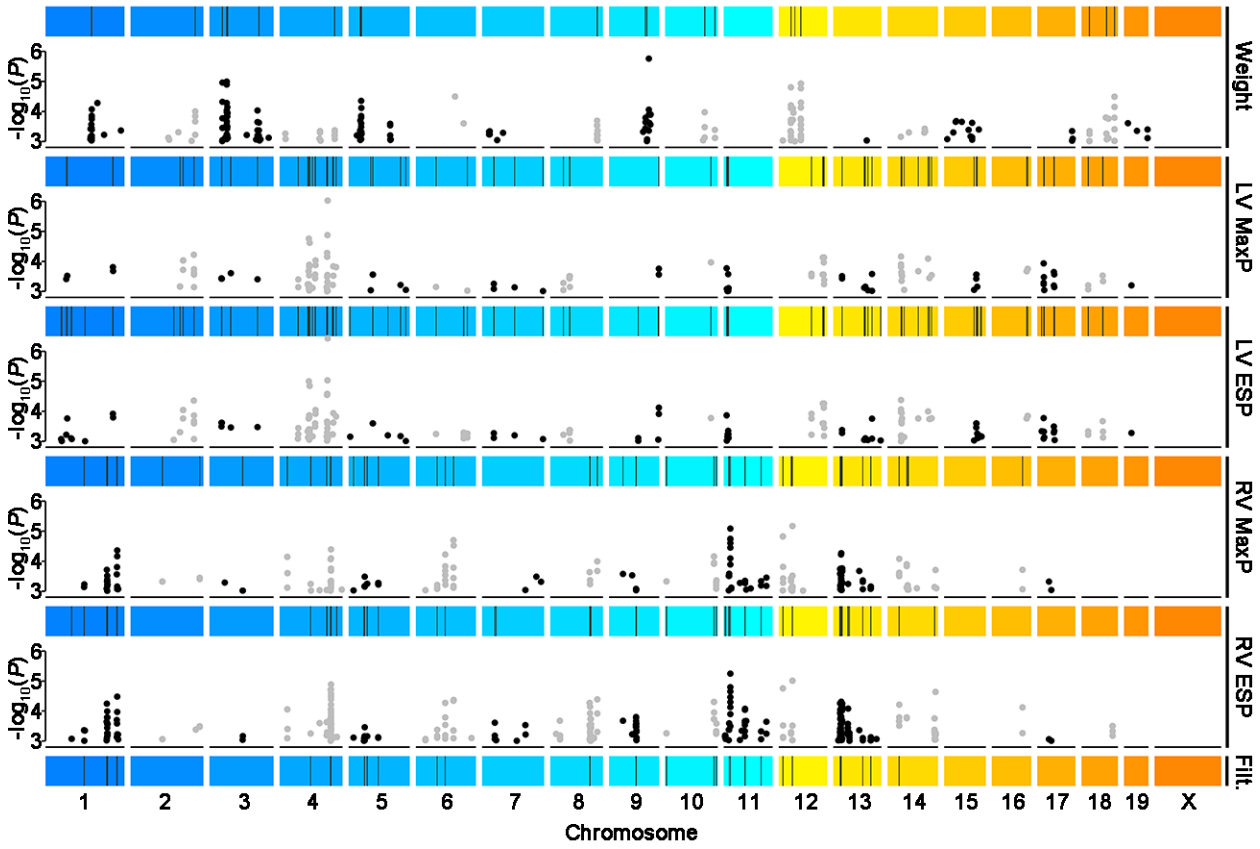

Figure 24. Region-based filtering of GWAS results.
Genome wide SNP association *P*-values were calculated by GEMMA for fold change (HFD v. RD) in body weight (Weight), LV maximum pressure (LV MaxP), LV end-systolic pressure (LV ESP), RV maximum pressure (RV MaxP), and RV end-systolic pressure (RV ESP). Black and gray dots represent SNP *P*-values (left axis) for the respective phenotypes (right axis) at their chromosomal position (x axis). Colored strips represent chromosomes, and black bars show regions containing one enriched (hypergeometric $P < 2.5\text{x}10^{-3}$) for significant SNPs ($P < 10^{-3}$). Regions were filtered (Filt.) as chromosomal regions that were significant in RV MaxP and RV ESP phenotypes but neither Weight, LV MaxP, nor LV ESP phenotypes.

5.3.3 Network analysis identifies candidate genes associated with human PH

For the next step in our filtering process, we sought to identify genes that are closely related to what is currently known about pulmonary hypertension (PH). Protein interaction networks have been successfully used to gain novel insights into PH pathogenesis [64, 193], and we examined the PH-relatedness of the human orthologues [192] of our candidate genes based on their

connectedness to a subnetwork of known PH genes [193] within a curated global network of protein-protein interactions [191] (Figure 25).

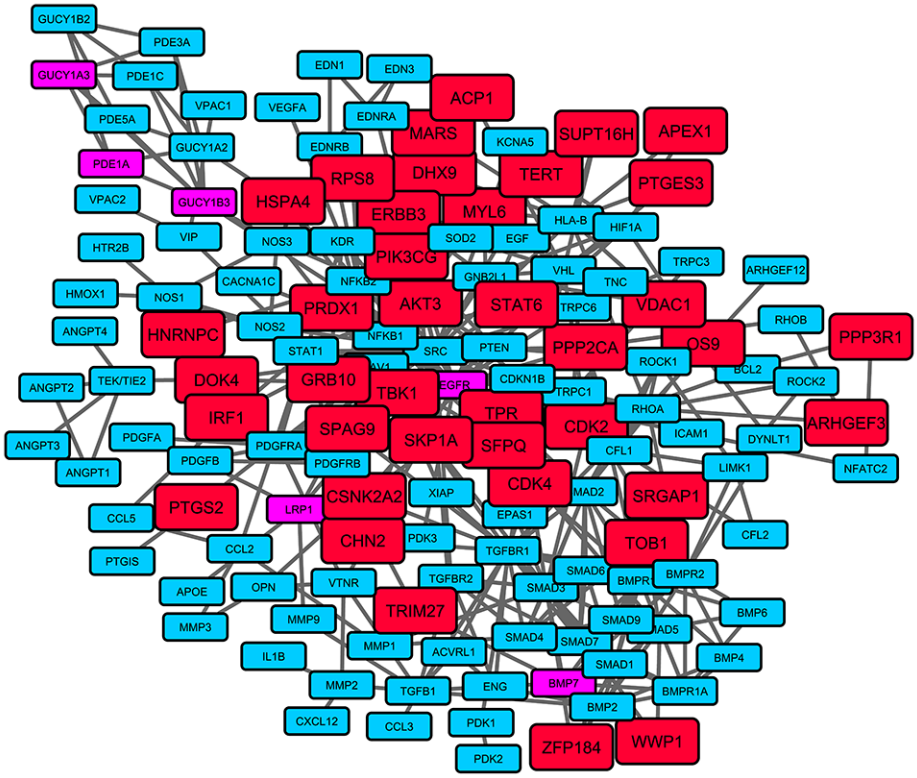

Figure 25. Pulmonary hypertension interactome with candidate genes.
Graph showing known PH genes (blue) and their interactions with each other and PH candidate genes that are already known PH genes (pink) or neighbors of known PH genes (red).

We scored the PH-relatedness of our candidate genes based on their shortest path betweenness centrality [194] in a subnetwork consisting of the candidate and known PH genes [64]. Shortest path betweenness centrality of a node *v* measures the fraction of shortest paths between two other network nodes, *s* and *t*, that pass through *v*; in essence, shortest path betweenness centrality measures the amount of network connectivity that would be lost of *v* were to be removed from the network. We normalized each value to its theoretical maximum for an undirected graph: one half times the subnetwork size minus one times the subnetwork size minus two (Table 6).

Table 6. Top fifteen candidate genes ranked by normalized betweenness centrality.
Known PH-related genes are highlighted in yellow.

Symbol	Chrom.	Start	End	Betweenness Centrality
Gucy1b3	3	81835926	81878633	0.07256
Egfr	11	16652206	16818161	0.07155
Dok4	8	97387728	97400212	0.04940
Ppp2ca	11	51912183	51941280	0.03848
Sfpq	4	126698568	126714257	0.02890
Hspa4	11	53073316	53113959	0.02625
Irf1	11	53583516	53591876	0.02458
Cdk2	10	128134995	128142107	0.02446
Cdk4	10	126500590	126504976	0.02333
Skp1a	11	52045497	52060360	0.02198
Myl6	10	127927916	127930931	0.02167
Mars	10	126733277	126748842	0.02105
Stat6	10	127080042	127098013	0.02105
Hnrnpc	14	52693055	52723703	0.02105
Tbk1	10	120983511	121023850	0.02105

5.4 DISCUSSION

In this report, we present the results of a murine GWAS of right ventricular pressure phenotypes after chronic high-fat feeding. Through region-, phenotype-, and network-based filtering steps, we identified a group of candidate genes that may be related to murine and human pulmonary hypertension.

Notable among these candidate genes is *Ppp2ca*, which encodes the catalytic subunit of protein phosphatase 2A (PP2A). In a recent RNA profiling study (GSE15197) [196] of human lung samples, its human orthologue *PPP2CA* was among the most downregulated transcripts in PAH lung tissue versus control. PP2A has diverse biological roles, including as a negative

regulator of cellular growth, proliferation, and cell cycle progression [197, 198]. Given the importance of these pathways in the pathogenesis of PH [30], *Ppp2ca* appears to be an ideal candidate for further study.

Although the focus of this study was on the pulmonary circulation and right-ventricular hemodynamics, our results should be widely useful to other investigators. For example, it is well-known that hyperlipidemic states contribute to diseases of the systemic circulation, as well [199, 200]. Hence, the results of this comprehensive study may be of use to investigators interested in left-sided cardiovascular disease. In addition, the results of our strain survey should be useful to all investigators studying pulmonary hypertension, regardless of their application to GWAS. With the recent advent of simpler approaches to genome editing [201], the strain survey should provide useful insight into the ideal background strains for future genetic studies into PH susceptibility.

5.5 CONCLUSIONS

In summary, this report describes the results of a strain study that was used to identify *Ppp2ca* as a candidate gene in high-fat diet-induced PH susceptibility. Our findings and data will be useful to investigators in multiple fields examining the relationship between metabolism and right- and left-sided cardiovascular hemodynamics.

6.0 IMPACT AND FUTURE DIRECTIONS

6.1 QUANTIFICATION OF VASCULAR REMODELING

The quantification of wall thickness extends to numerous scenarios beyond medial thickening of the small arteries in the lungs. Of course, intimal and adventitial thickening of pulmonary artery walls are key histopathological features of PAH [13] and can also be quantified by the skeleton method. Likewise, the accuracy of the method also applies to their systemic counterparts in the setting of systemic vascular remodeling [16, 202].

Meanwhile, one does not have to think very long to recognize the multiple other body conduits whose wall thicknesses could be measured using the skeleton method and the VMI calculator. For instance, bronchial smooth muscle growth is a notable feature of asthma [203] and its thickening is readily quantified by our approach. Hence, the breadth of its applicability should make the skeleton method of wall thickness quantification a useful and impactful resource for investigators in multiple fields.

6.2 SR20 IN LUNG CANCER

The beneficial angiostatic effects of MMP12 against lung cancer have long been known [98, 99]. However, the prospect of harnessing MMP12 activity to fight cancers has never gained traction,

presumably – at least in part – owing to its harmful elastolytic activity in the setting of emphysema [94, 204]. Here we show that SR20 offers the exciting prospect of harnessing some anti-tumor activity of MMP12 without the elastolytic side-effects. Of course, we still have much to learn about SR20 before it can be used in human populations, in particular its effects on other tissues such as the pulmonary vasculature where it may promote medial thickening and vascular remodeling.

6.3 TRANSCRIPTIONAL MODULATION BY SR20

The evidence presented suggests that SR20 mediates its tumor-apoptotic and vascular smooth muscle cell-proliferative effects through transcriptional upregulation of *TRAIL*. In the context of what is already known about MMP12, particularly that its catalytic and carboxyterminal domains traffic to the nucleus where the catalytic domain activates a gene transcription program [132], our explanation of a separate transcriptional role for SR20 appears plausible. However, it seems unlikely that SR20 and the MMP12 CTD would regulate *TRAIL* alone. Hence, further high-throughput studies are needed to determine the exact nature of SR20's transcriptional effects on multiple cell types. Using ChIP-Seq technology to identify genomic binding sites and gene expression arrays to identify transcriptomic responses will allow a better and more complete characterization of the true nature of SR20's actions.

6.4 THE ROLE OF MMP12 IN PULMONARY HYPERTENSION

In vitro, the MMP12 CTD appears to clearly induce TRAIL-dependent proliferation of hPASMCs. However, our murine models demonstrate that the exact nature of MMP12's role in PH is far more complex, as genetic deletion of *Mmp12* was associated with increased susceptibility to chronic hypoxia-induced PH. Future studies should first focus on the role of MMP12 in endothelial cell proliferation and intimal hypertrophy both *in vivo* and *in vitro*, as MMP12 and TRAIL are known to negatively regulate these processes and may therefore impede the development of PH [98, 164].

6.5 GWAS

In this report, we present the results of a murine GWAS relating genomic regions to high-fat diet-induced changes in right-ventricular maximum pressure. These findings will be useful to other researchers in the field, who can use the results to guide *in vitro* and *in vivo* studies that will further advance the field. In addition, the tissues banked from the study will be useful in determining genetic associations to other quantitative phenotypes; for example, using the VMI calculator, it will be feasible to quantify vascular remodeling in lungs from the 36 strains and determine genetic loci associated with this phenotype.

APPENDIX A

This section provides tables of the top 200 most significant single nucleotide polymorphisms (SNPs) from the genome-wide association study (see 5.0). Chromosomal positions are based upon NCBI genome build 37.

A.1 BODY WEIGHT SNP ASSOCIATIONS

Table 7 lists the top 200 SNPs associated with fold change in body weight (high-fat diet v. regular diet).

Table 7. Top 200 SNPs associated with fold change in body weight.

SNP	Chrom	Position	*P*-value
mm37-9-99229402:MAG18141024	9	99229402	1.73E-06
mm37-3-42827940	3	42827940	1.02E-05
NES15880954	3	32081078	1.10E-05
mm37-12-55400491:NES17579563	12	55400491	1.18E-05
NES15901144	3	42792364	1.27E-05
NES15371855	12	30645627	1.56E-05
NES15371686	12	30650567	1.56E-05
NES17579804	12	55389730	1.68E-05
NES17579626	12	55394467	1.68E-05
NES17579557	12	55400161	1.68E-05
NES13726835	6	97738622	3.17E-05

NES13725843	6	97771620	3.17E-05
NES13725745	6	97774932	3.17E-05
NES13725728	6	97775302	3.17E-05
NES13725733	6	97775571	3.17E-05
NES13725734	6	97775593	3.17E-05
NES13725737	6	97775761	3.17E-05
NES13725680	6	97781018	3.17E-05
NES13725248	6	97788727	3.17E-05
NES15143088	18	82453617	3.25E-05
NES15142919	18	82460182	3.25E-05
NES10276888	5	31360939	4.47E-05
NES15880950	3	32080777	4.75E-05
NES15880888	3	32082602	4.75E-05
NES15880839	3	32084566	4.75E-05
NES15880851	3	32084942	4.75E-05
NES15880799	3	32086414	4.75E-05
NES15880807	3	32086548	4.75E-05
NES15880702	3	32093941	4.75E-05
NES15880578	3	32107778	4.75E-05
NES11238208	12	55232071	5.08E-05
NES11241158	12	55174827	5.11E-05
NES11240253	12	55195989	5.11E-05
NES11239946	12	55198272	5.11E-05
NES15901461	3	42739894	5.22E-05
NES15901466	3	42740251	5.22E-05
NES15901379	3	42748319	5.22E-05
NES15901329	3	42756882	5.22E-05
NES15901143	3	42792249	5.22E-05
NES15901025	3	42810166	5.22E-05
NES15900602	3	42859769	5.22E-05
mm37-3-42860510:NES15900626	3	42860510	5.22E-05
NES15900425	3	42869682	5.22E-05
NES15900208	3	42878518	5.22E-05
mm37-3-42879722	3	42879722	5.22E-05
mm37-3-42965073:NES15899439	3	42965073	5.22E-05
mm37-1-129839661:NES16469524	1	129839661	5.25E-05
NES15371568	12	30654863	6.29E-05
NES17437016	18	82440722	7.03E-05
NES17437018	18	82440771	7.03E-05

NES17437020	18	82440804	7.03E-05
NES17437022	18	82440826	7.03E-05
NES17437024	18	82440838	7.03E-05
NES17437026	18	82440878	7.03E-05
NES17437030	18	82440940	7.03E-05
NES15143082	18	82452999	7.03E-05
NES15143083	18	82453483	7.03E-05
NES15143031	18	82455469	7.03E-05
NES15142894	18	82459542	7.03E-05
NES14696377	3	44600162	7.15E-05
NES11240781	12	55184153	7.37E-05
NES11240245	12	55195579	7.37E-05
NES11240050	12	55197289	7.37E-05
NES11240056	12	55197535	7.37E-05
NES11239985	12	55197772	7.37E-05
NES11239953	12	55198345	7.37E-05
NES11239838	12	55199738	7.37E-05
NES11239766	12	55200533	7.37E-05
mm37-5-31562956:rs6254142:NES10269394	5	31562956	7.59E-05
mm37-5-31564892	5	31564892	7.59E-05
NES15379173	12	30356570	7.72E-05
NES15379104	12	30362510	7.72E-05
NES15379105	12	30362538	7.72E-05
NES15378959	12	30374371	7.72E-05
NES15378929	12	30384888	7.72E-05
NES17549880	12	35349978	7.96E-05
NES16414654	1	115558525	8.46E-05
mm37-1-115561430	1	115561430	8.46E-05
NES16430769	1	115630623	8.46E-05
mm37-1-115663964:NES12799491	1	115663964	8.46E-05
NES16825034	9	99235831	8.79E-05
NES16825000	9	99236398	8.79E-05
NES16824899	9	99243583	8.79E-05
mm37-3-119623628:NES13912687	3	119623628	9.28E-05
mm37-3-42832136	3	42832136	9.30E-05
mm37-2-161205958:rs3664408:NES08878410	2	161205958	1.01E-04
mm37-2-161217352:NES08878182	2	161217352	1.01E-04
NES14158944	10	98725936	1.07E-04
NES14158962	10	98730683	1.07E-04

mm37-3-42924601	3	42924601	1.08E-04
NES15899392	3	42972986	1.08E-04
NES17542492	12	36597790	1.12E-04
NES17542329	12	36606064	1.12E-04
NES17542284	12	36606711	1.12E-04
mm37-3-44787487	3	44787487	1.12E-04
NES14693391	3	44800612	1.12E-04
NES14693392	3	44800710	1.12E-04
NES14693393	3	44800770	1.12E-04
mm37-3-44804863:NES14693357	3	44804863	1.12E-04
mm37-3-44805008	3	44805008	1.12E-04
mm37-9-103536855	9	103536855	1.25E-04
NES16825183	9	99228170	1.28E-04
NES16825185	9	99228308	1.28E-04
mm37-9-103305949	9	103305949	1.30E-04
mm37-9-103336198	9	103336198	1.30E-04
NES13013045	1	115314482	1.40E-04
NES10249433	5	31236455	1.41E-04
NES08879080	2	161167058	1.43E-04
NES08878978	2	161175327	1.43E-04
mm37-3-43003681:NES15899143	3	43003681	1.45E-04
NES14696800	3	44572702	1.45E-04
NES14696801	3	44572843	1.45E-04
mm37-3-44575652	3	44575652	1.45E-04
mm37-3-44592340	3	44592340	1.45E-04
mm37-3-44598954:NES14696366	3	44598954	1.45E-04
mm37-1-115415827:NES13011163	1	115415827	1.55E-04
mm37-1-115415905:NES13011166	1	115415905	1.55E-04
mm37-1-115441025:NES13010741	1	115441025	1.55E-04
NES13010687	1	115442030	1.55E-04
NES15901469	3	42740444	1.56E-04
mm37-3-42745130:NES15901402	3	42745130	1.56E-04
mm37-3-42745634:NES15901406	3	42745634	1.56E-04
mm37-3-42749006	3	42749006	1.56E-04
NES15901315	3	42761563	1.56E-04
NES15901131	3	42792895	1.56E-04
NES15901074	3	42805653	1.56E-04
mm37-3-42821843:NES15900958	3	42821843	1.56E-04
mm37-3-42837665	3	42837665	1.56E-04

mm37-5-31370225:NES10276507	5	31370225	1.60E-04
mm37-18-60815124	18	60815124	1.60E-04
NES11298223	9	90690527	1.61E-04
NES11298226	9	90690567	1.61E-04
NES11297573	9	90720450	1.61E-04
NES11297585	9	90721482	1.61E-04
NES11297473	9	90724593	1.61E-04
NES11297476	9	90724625	1.61E-04
NES11297480	9	90724778	1.61E-04
NES17437150	18	82424698	1.63E-04
mm37-3-32086003:rs3702402:NES15880869	3	32086003	1.70E-04
mm37-12-55120751:NES11242905	12	55120751	1.74E-04
mm37-18-67352668:NES13445857	18	67352668	1.74E-04
mm37-1-115424544:rs3662693	1	115424544	1.81E-04
mm37-12-55448035	12	55448035	1.90E-04
NES15371584	12	30655324	1.91E-04
NES15371480	12	30658515	1.91E-04
NES15371436	12	30659810	1.91E-04
NES15371437	12	30659823	1.91E-04
NES17549576	12	35363535	1.93E-04
NES13877203	5	28992569	2.01E-04
NES13877204	5	28992604	2.01E-04
NES16253271	8	116779495	2.04E-04
NES16253251	8	116780539	2.04E-04
mm37-12-30708434	12	30708434	2.06E-04
NES12617240	15	30208893	2.10E-04
mm37-3-42832943	3	42832943	2.15E-04
NES08873225	2	161381064	2.17E-04
NES14218431	9	94676111	2.20E-04
NES14218433	9	94676182	2.20E-04
NES14216699	9	94781578	2.20E-04
NES16987314	15	28836899	2.23E-04
NES16986784	15	28869241	2.23E-04
NES12608137	15	44045164	2.23E-04
NES13912487	3	119638490	2.27E-04
NES13912456	3	119644146	2.27E-04
NES15372105	12	30639193	2.28E-04
NES15371825	12	30645179	2.28E-04
NES15371718	12	30649544	2.28E-04

NES15371698	12	30651055	2.28E-04
NES15371701	12	30651361	2.28E-04
NES15371576	12	30655047	2.28E-04
NES15371514	12	30656615	2.28E-04
NES15371519	12	30656770	2.28E-04
NES15371479	12	30658511	2.28E-04
NES15371435	12	30659794	2.28E-04
NES15371446	12	30660314	2.28E-04
NES15371447	12	30660331	2.28E-04
NES15371448	12	30660482	2.28E-04
NES15371450	12	30660684	2.28E-04
NES15371396	12	30662688	2.28E-04
NES17541314	12	30669866	2.28E-04
NES17541329	12	30670292	2.28E-04
NES17541344	12	30671371	2.28E-04
NES17541346	12	30671674	2.28E-04
NES17541352	12	30671861	2.28E-04
NES17541369	12	30672732	2.28E-04
NES17541101	12	30677011	2.28E-04
NES17541033	12	30678354	2.28E-04
NES17541057	12	30679419	2.28E-04
NES17541071	12	30680026	2.28E-04
NES17540971	12	30680982	2.28E-04
mm37-9-90819248:NES11299217	9	90819248	2.29E-04
mm37-3-123129477	3	123129477	2.38E-04
NES12101074	15	70147859	2.40E-04
NES17540538	12	30707366	2.41E-04
NES17540556	12	30708157	2.41E-04
NES17540490	12	30709210	2.41E-04
NES17540494	12	30709905	2.41E-04
NES17540496	12	30709989	2.41E-04
NES17540498	12	30710044	2.41E-04
NES11265794	9	100464827	2.43E-04

A.2 LV MAXIMUM PRESSURE SNP ASSOCIATIONS

Table 8 lists the top 200 SNPs associated with fold change in LV maximum pressure (high-fat diet v. regular diet).

Table 8. Top 200 SNPs associated with fold change in LV maximum pressure.

SNP	Chrom	Position	*P*-value
mm37-4-119476429	4	119476429	9.37E-07
MAG9211909:NES09211909	4	118947139	1.34E-05
NES09622860	4	72939446	1.74E-05
mm37-4-74654892	4	74654892	2.39E-05
NES09606991	4	74671307	2.39E-05
mm37-4-74687915	4	74687915	2.39E-05
NES09605939	4	74711331	2.39E-05
NES09605453	4	74735628	2.39E-05
NES09605456	4	74735831	2.39E-05
NES09605459	4	74736427	2.39E-05
NES09605461	4	74736652	2.39E-05
NES09605463	4	74736936	2.39E-05
NES09605465	4	74737505	2.39E-05
NES09605129	4	74738351	2.39E-05
NES09605130	4	74738493	2.39E-05
NES09605133	4	74739529	2.39E-05
NES09604863	4	74759538	2.39E-05
mm37-4-74761420:NES09604634	4	74761420	2.39E-05
mm37-4-74767015:NES09604391	4	74767015	2.39E-05
NES09603971	4	74776152	2.39E-05
NES09603884	4	74777048	2.39E-05
NES09603885	4	74777122	2.39E-05
NES09603759	4	74790472	2.39E-05
NES09603761	4	74790509	2.39E-05
NES09603682	4	74793720	2.39E-05
NES09603683	4	74793987	2.39E-05
NES09603688	4	74794520	2.39E-05
mm37-4-74795775	4	74795775	2.39E-05
mm37-4-74861893	4	74861893	2.39E-05
NES09601316	4	74862082	2.39E-05

NES09206772	4	118339108	5.27E-05
NES09206589	4	118346220	5.27E-05
NES09206448	4	118352188	5.27E-05
NES09206449	4	118352279	5.27E-05
NES09206468	4	118352838	5.27E-05
NES09206338	4	118354949	5.27E-05
NES08890892	2	158148931	6.00E-05
NES08890578	2	158159601	6.00E-05
NES08890579	2	158159745	6.00E-05
NES08890540	2	158160423	6.00E-05
NES15555324	14	33754104	6.94E-05
NES15555326	14	33754179	6.94E-05
NES15555137	14	33761073	6.94E-05
NES15555105	14	33764593	6.94E-05
NES09207536	4	118300793	6.98E-05
NES09206764	4	118338691	6.98E-05
mm37-4-118425231:NES09204632	4	118425231	6.98E-05
NES14382140	12	110096209	7.47E-05
NES14382061	12	110096640	7.47E-05
NES14382027	12	110097481	7.47E-05
NES14382029	12	110097696	7.47E-05
NES14382030	12	110097733	7.47E-05
NES14382043	12	110098599	7.47E-05
NES14382050	12	110098747	7.47E-05
NES14382001	12	110099353	7.47E-05
NES14382005	12	110099640	7.47E-05
NES14381942	12	110100273	7.47E-05
NES14381953	12	110100731	7.47E-05
NES14381931	12	110101028	7.47E-05
NES14381934	12	110101241	7.47E-05
NES14381886	12	110103133	7.47E-05
NES14381900	12	110103490	7.47E-05
NES14381910	12	110103695	7.47E-05
NES14381702	12	110112646	7.47E-05
NES14381697	12	110113520	7.47E-05
NES14381652	12	110117222	7.47E-05
NES14381643	12	110119105	7.47E-05
NES14381647	12	110119534	7.47E-05
NES14381634	12	110120172	7.47E-05

NES14381631	12	110121517	7.47E-05
NES14381624	12	110122266	7.47E-05
NES14381606	12	110124597	7.47E-05
mm37-12-110136561:rs13481642:NES14381397	12	110136561	7.47E-05
NES14381182	12	110148475	7.47E-05
NES14381147	12	110149602	7.47E-05
mm37-12-113149691	12	113149691	7.47E-05
mm37-14-101290805:NES17292559	14	101290805	8.19E-05
NES08986261	2	131070746	9.38E-05
mm37-2-131372744:rs6206689	2	131372744	9.38E-05
NES09578155	4	89111651	9.38E-05
NES14380456	12	112372895	1.08E-04
NES14380392	12	112374448	1.08E-04
NES15325486	10	114306516	1.08E-04
NES15325492	10	114307088	1.08E-04
mm37-17-15897639	17	15897639	1.17E-04
mm37-14-33742812	14	33742812	1.27E-04
mm37-14-33748914	14	33748914	1.27E-04
NES15555388	14	33752836	1.27E-04
NES15555389	14	33752865	1.27E-04
NES15555390	14	33752882	1.27E-04
NES15555392	14	33753021	1.27E-04
NES15555393	14	33753096	1.27E-04
NES15555396	14	33753285	1.27E-04
NES15555398	14	33753411	1.27E-04
NES15555319	14	33753616	1.27E-04
NES15555320	14	33753638	1.27E-04
NES15555321	14	33753726	1.27E-04
NES15555322	14	33753774	1.27E-04
NES09620643	4	73588854	1.29E-04
NES09578806	4	89098525	1.34E-04
NES09578581	4	89100112	1.34E-04
NES09578590	4	89100570	1.34E-04
NES09578594	4	89101023	1.34E-04
NES09578597	4	89101144	1.34E-04
NES09578598	4	89101266	1.34E-04
NES09578599	4	89101331	1.34E-04
NES09578600	4	89101396	1.34E-04
NES09578601	4	89101463	1.34E-04

NES09578502	4	89101815	1.34E-04
NES09578515	4	89102282	1.34E-04
NES09578518	4	89102339	1.34E-04
NES09578387	4	89103796	1.34E-04
NES09578388	4	89103973	1.34E-04
NES09165205	4	133732760	1.46E-04
NES09164769	4	133752474	1.46E-04
NES09164669	4	133756839	1.46E-04
NES09164653	4	133757585	1.46E-04
NES09164636	4	133757816	1.46E-04
mm37-4-73666375:NES09619921	4	73666375	1.51E-04
NES17508375	4	73669661	1.51E-04
NES17508344	4	73672937	1.51E-04
NES17508345	4	73672956	1.51E-04
NES17508347	4	73673090	1.51E-04
mm37-4-74431635:NES09597900	4	74431635	1.51E-04
NES15556586	14	33650999	1.53E-04
NES15556588	14	33651114	1.53E-04
NES15556590	14	33651224	1.53E-04
NES15556591	14	33651241	1.53E-04
NES15556593	14	33651499	1.53E-04
NES15556488	14	33666202	1.53E-04
NES15556364	14	33681131	1.53E-04
NES15556350	14	33682366	1.53E-04
NES15556322	14	33682946	1.53E-04
NES15556325	14	33682972	1.53E-04
NES15556329	14	33683043	1.53E-04
NES15556222	14	33688466	1.53E-04
NES15556227	14	33688753	1.53E-04
NES15556228	14	33688818	1.53E-04
NES15556235	14	33689010	1.53E-04
NES15556200	14	33689687	1.53E-04
NES15556087	14	33697398	1.53E-04
NES15556041	14	33698784	1.53E-04
NES15556014	14	33700678	1.53E-04
NES15555957	14	33701907	1.53E-04
NES15555964	14	33702438	1.53E-04
NES15555977	14	33703621	1.53E-04
NES15555848	14	33711433	1.53E-04

NES15555590	14	33730600	1.53E-04
NES15555595	14	33731160	1.53E-04
NES15555613	14	33732324	1.53E-04
NES15555549	14	33735902	1.53E-04
NES15555519	14	33739563	1.53E-04
NES13041746	1	168034034	1.56E-04
NES09132218	4	140617089	1.57E-04
mm37-11-7316060:NES08405904	11	7316060	1.69E-04
NES16857407	9	124036804	1.77E-04
NES16857412	9	124037070	1.77E-04
NES16857219	9	124038619	1.77E-04
NES16857221	9	124038646	1.77E-04
NES16857226	9	124038721	1.77E-04
NES12204093	16	89361587	1.80E-04
NES12198104	16	89508178	1.80E-04
NES08904471	2	158333971	1.85E-04
NES08904261	2	158343066	1.85E-04
NES08904262	2	158343244	1.85E-04
NES08904265	2	158343285	1.85E-04
NES08904192	2	158344228	1.85E-04
NES08904218	2	158345265	1.85E-04
NES08904112	2	158348489	1.85E-04
NES08986258	2	131070195	1.93E-04
NES14451111	1	168909119	2.12E-04
NES14451114	1	168909224	2.12E-04
NES09616523	4	72359781	2.14E-04
NES12530568	14	76589485	2.14E-04
mm37-14-76591940:NES12530477	14	76591940	2.14E-04
NES12530308	14	76596545	2.14E-04
mm37-14-76605080:NES12530055	14	76605080	2.14E-04
mm37-16-86640905	16	86640905	2.14E-04
mm37-17-41425478:gnf17.041.719:NES12214197	17	41425478	2.28E-04
NES08889329	2	158210048	2.36E-04
NES08889332	2	158210212	2.36E-04
NES08889335	2	158210323	2.36E-04
NES08889317	2	158211579	2.36E-04
NES17204253	14	34816108	2.36E-04
NES17202918	14	34881395	2.36E-04
NES17198117	14	35080473	2.36E-04

NES17196428	14	35139619	2.36E-04
NES17196320	14	35143150	2.36E-04
NES17195945	14	35149557	2.36E-04
NES10806469	3	53038243	2.47E-04
NES10806474	3	53038311	2.47E-04
NES10806400	3	53038979	2.47E-04
NES10806406	3	53039268	2.47E-04
NES10806407	3	53039294	2.47E-04
NES10806408	3	53039329	2.47E-04
NES10806281	3	53040433	2.47E-04
NES10806285	3	53040867	2.47E-04
NES10805570	3	53051821	2.47E-04
NES17198120	14	35080850	2.55E-04
NES17196595	14	35132522	2.55E-04

A.3 LV END-SYSTOLIC PRESSURE SNP ASSOCIATIONS

Table 9 lists the top 200 SNPs associated with fold change in LV end-systolic pressure (high-fat diet v. regular diet).

Table 9. Top 200 SNPs associated with fold change in LV end-systolic pressure.

SNP	Chrom	Position	*P*-value
mm37-4-119476429	4	119476429	3.73E-07
MAG9211909:NES09211909	4	118947139	9.35E-06
NES09622860	4	72939446	1.02E-05
mm37-4-74654892	4	74654892	1.42E-05
NES09606991	4	74671307	1.42E-05
mm37-4-74687915	4	74687915	1.42E-05
NES09605939	4	74711331	1.42E-05
NES09605453	4	74735628	1.42E-05
NES09605456	4	74735831	1.42E-05
NES09605459	4	74736427	1.42E-05
NES09605461	4	74736652	1.42E-05

NES09605463	4	74736936	1.42E-05
NES09605465	4	74737505	1.42E-05
NES09605129	4	74738351	1.42E-05
NES09605130	4	74738493	1.42E-05
NES09605133	4	74739529	1.42E-05
NES09604863	4	74759538	1.42E-05
mm37-4-74761420:NES09604634	4	74761420	1.42E-05
mm37-4-74767015:NES09604391	4	74767015	1.42E-05
NES09603971	4	74776152	1.42E-05
NES09603884	4	74777048	1.42E-05
NES09603885	4	74777122	1.42E-05
NES09603759	4	74790472	1.42E-05
NES09603761	4	74790509	1.42E-05
NES09603682	4	74793720	1.42E-05
NES09603683	4	74793987	1.42E-05
NES09603688	4	74794520	1.42E-05
mm37-4-74795775	4	74795775	1.42E-05
mm37-4-74861893	4	74861893	1.42E-05
NES09601316	4	74862082	1.42E-05
NES09207536	4	118300793	2.66E-05
NES09206764	4	118338691	2.66E-05
mm37-4-118425231:NES09204632	4	118425231	2.66E-05
NES09206772	4	118339108	2.85E-05
NES09206589	4	118346220	2.85E-05
NES09206448	4	118352188	2.85E-05
NES09206449	4	118352279	2.85E-05
NES09206468	4	118352838	2.85E-05
NES09206338	4	118354949	2.85E-05
NES15555324	14	33754104	4.20E-05
NES15555326	14	33754179	4.20E-05
NES15555137	14	33761073	4.20E-05
NES15555105	14	33764593	4.20E-05
NES08890892	2	158148931	4.44E-05
NES08890578	2	158159601	4.44E-05
NES08890579	2	158159745	4.44E-05
NES08890540	2	158160423	4.44E-05
NES14382140	12	110096209	5.56E-05
NES14382061	12	110096640	5.56E-05
NES14382027	12	110097481	5.56E-05

NES14382029	12	110097696	5.56E-05
NES14382030	12	110097733	5.56E-05
NES14382043	12	110098599	5.56E-05
NES14382050	12	110098747	5.56E-05
NES14382001	12	110099353	5.56E-05
NES14382005	12	110099640	5.56E-05
NES14381942	12	110100273	5.56E-05
NES14381953	12	110100731	5.56E-05
NES14381931	12	110101028	5.56E-05
NES14381934	12	110101241	5.56E-05
NES14381886	12	110103133	5.56E-05
NES14381900	12	110103490	5.56E-05
NES14381910	12	110103695	5.56E-05
NES14381702	12	110112646	5.56E-05
NES14381697	12	110113520	5.56E-05
NES14381652	12	110117222	5.56E-05
NES14381643	12	110119105	5.56E-05
NES14381647	12	110119534	5.56E-05
NES14381634	12	110120172	5.56E-05
NES14381631	12	110121517	5.56E-05
NES14381624	12	110122266	5.56E-05
NES14381606	12	110124597	5.56E-05
mm37-12-110136561:rs13481642:NES14381397	12	110136561	5.56E-05
NES14381182	12	110148475	5.56E-05
NES14381147	12	110149602	5.56E-05
mm37-12-113149691	12	113149691	5.56E-05
NES16857407	9	124036804	7.58E-05
NES16857412	9	124037070	7.58E-05
NES16857219	9	124038619	7.58E-05
NES16857221	9	124038646	7.58E-05
NES16857226	9	124038721	7.58E-05
NES14380456	12	112372895	7.60E-05
NES14380392	12	112374448	7.60E-05
mm37-14-33742812	14	33742812	8.69E-05
mm37-14-33748914	14	33748914	8.69E-05
NES15555388	14	33752836	8.69E-05
NES15555389	14	33752865	8.69E-05
NES15555390	14	33752882	8.69E-05
NES15555392	14	33753021	8.69E-05

NES15555393	14	33753096	8.69E-05
NES15555396	14	33753285	8.69E-05
NES15555398	14	33753411	8.69E-05
NES15555319	14	33753616	8.69E-05
NES15555320	14	33753638	8.69E-05
NES15555321	14	33753726	8.69E-05
NES15555322	14	33753774	8.69E-05
NES08986261	2	131070746	9.06E-05
mm37-2-131372744:rs6206689	2	131372744	9.06E-05
NES09578155	4	89111651	9.06E-05
mm37-14-101290805:NES17292559	14	101290805	1.01E-04
NES15556586	14	33650999	1.08E-04
NES15556588	14	33651114	1.08E-04
NES15556590	14	33651224	1.08E-04
NES15556591	14	33651241	1.08E-04
NES15556593	14	33651499	1.08E-04
NES15556488	14	33666202	1.08E-04
NES15556364	14	33681131	1.08E-04
NES15556350	14	33682366	1.08E-04
NES15556322	14	33682946	1.08E-04
NES15556325	14	33682972	1.08E-04
NES15556329	14	33683043	1.08E-04
NES15556222	14	33688466	1.08E-04
NES15556227	14	33688753	1.08E-04
NES15556228	14	33688818	1.08E-04
NES15556235	14	33689010	1.08E-04
NES15556200	14	33689687	1.08E-04
NES15556087	14	33697398	1.08E-04
NES15556041	14	33698784	1.08E-04
NES15556014	14	33700678	1.08E-04
NES15555957	14	33701907	1.08E-04
NES15555964	14	33702438	1.08E-04
NES15555977	14	33703621	1.08E-04
NES15555848	14	33711433	1.08E-04
NES15555590	14	33730600	1.08E-04
NES15555595	14	33731160	1.08E-04
NES15555613	14	33732324	1.08E-04
NES15555549	14	33735902	1.08E-04
NES15555519	14	33739563	1.08E-04

NES17198120	14	35080850	1.15E-04
NES17196595	14	35132522	1.15E-04
NES09165205	4	133732760	1.16E-04
NES09164769	4	133752474	1.16E-04
NES09164669	4	133756839	1.16E-04
NES09164653	4	133757585	1.16E-04
NES09164636	4	133757816	1.16E-04
NES11223031	12	81752212	1.21E-04
NES11222962	12	81752728	1.21E-04
NES11222965	12	81752891	1.21E-04
NES11222858	12	81754828	1.21E-04
NES11222742	12	81756236	1.21E-04
NES11222600	12	81759772	1.21E-04
NES11222400	12	81763590	1.21E-04
NES11222402	12	81763618	1.21E-04
NES11222406	12	81763768	1.21E-04
NES13041746	1	168034034	1.22E-04
NES09578806	4	89098525	1.22E-04
NES09578581	4	89100112	1.22E-04
NES09578590	4	89100570	1.22E-04
NES09578594	4	89101023	1.22E-04
NES09578597	4	89101144	1.22E-04
NES09578598	4	89101266	1.22E-04
NES09578599	4	89101331	1.22E-04
NES09578600	4	89101396	1.22E-04
NES09578601	4	89101463	1.22E-04
NES09578502	4	89101815	1.22E-04
NES09578515	4	89102282	1.22E-04
NES09578518	4	89102339	1.22E-04
NES09578387	4	89103796	1.22E-04
NES09578388	4	89103973	1.22E-04
NES16858033	9	123994045	1.22E-04
NES16857400	9	124036436	1.22E-04
NES16857401	9	124036565	1.22E-04
NES16857244	9	124039043	1.22E-04
mm37-11-7316060:NES08405904	11	7316060	1.38E-04
NES09620643	4	73588854	1.38E-04
NES08904471	2	158333971	1.39E-04
NES08904261	2	158343066	1.39E-04

NES08904262	2	158343244	1.39E-04
NES08904265	2	158343285	1.39E-04
NES08904192	2	158344228	1.39E-04
NES08904218	2	158345265	1.39E-04
NES08904112	2	158348489	1.39E-04
NES12204093	16	89361587	1.43E-04
NES12198104	16	89508178	1.43E-04
mm37-4-73666375:NES09619921	4	73666375	1.48E-04
NES17508375	4	73669661	1.48E-04
NES17508344	4	73672937	1.48E-04
NES17508345	4	73672956	1.48E-04
NES17508347	4	73673090	1.48E-04
mm37-4-74431635:NES09597900	4	74431635	1.48E-04
NES09132218	4	140617089	1.49E-04
mm37-4-73858188	4	73858188	1.61E-04
NES14451111	1	168909119	1.63E-04
NES14451114	1	168909224	1.63E-04
mm37-17-15897639	17	15897639	1.69E-04
NES15325486	10	114306516	1.70E-04
NES15325492	10	114307088	1.70E-04
mm37-14-109924888:NES12548985	14	109924888	1.72E-04
NES09616523	4	72359781	1.74E-04
NES12530568	14	76589485	1.74E-04
mm37-14-76591940:NES12530477	14	76591940	1.74E-04
NES12530308	14	76596545	1.74E-04
mm37-14-76605080:NES12530055	14	76605080	1.74E-04
mm37-16-86640905	16	86640905	1.74E-04
NES08986258	2	131070195	1.75E-04
mm37-12-81746815:NES11223291	12	81746815	1.75E-04
mm37-12-81746910:NES11223293	12	81746910	1.75E-04
NES11223106	12	81749778	1.75E-04
NES11223108	12	81749986	1.75E-04
NES11223112	12	81750129	1.75E-04

A.4 RV MAXIMUM PRESSURE SNP ASSOCIATIONS

Table 10 lists the top 200 SNPs associated with fold change in RV maximum pressure (high-fat diet v. regular diet).

Table 10. Top 200 SNPs associated with fold change in RV maximum pressure.

SNP	Chrom	Position	*P*-value
NES14421225	12	34348982	6.72E-06
mm37-12-34367760:NES14421066	12	34367760	6.72E-06
NES14420774	12	34394368	6.72E-06
NES08383993	11	16688981	8.18E-06
mm37-12-10580142:rs6209157:NES14428743	12	10580142	1.50E-05
NES08383985	11	16688806	1.80E-05
NES08383987	11	16688901	1.80E-05
NES08383996	11	16689319	1.80E-05
NES08384006	11	16689824	1.88E-05
mm37-6-93865234:NES13736033	6	93865234	1.99E-05
NES08383994	11	16689147	2.50E-05
NES08384007	11	16690201	2.50E-05
NES08384013	11	16690515	2.50E-05
NES08384117	11	16685717	2.51E-05
NES08384120	11	16685917	2.51E-05
NES08384100	11	16686440	2.51E-05
NES08384102	11	16686785	2.51E-05
mm37-6-94065571	6	94065571	3.00E-05
mm37-11-16690559:NES08384017	11	16690559	3.54E-05
NES09185662	4	127744586	4.04E-05
NES09185523	4	127748136	4.04E-05
NES15851806	1	178917666	4.35E-05
NES15851754	1	178921819	4.35E-05
NES15851706	1	178922738	4.35E-05
NES15851678	1	178923061	4.35E-05
NES15851697	1	178924544	4.35E-05
NES15851700	1	178924690	4.35E-05
NES14366459	13	19750561	5.39E-05
NES14366409	13	19751818	5.39E-05
NES14366412	13	19752054	5.39E-05

NES14366414	13	19752097	5.39E-05
NES14366415	13	19752115	5.39E-05
NES14366416	13	19752284	5.39E-05
NES15519226	13	19181316	6.00E-05
NES15518974	13	19197798	6.00E-05
NES14817172	6	73101326	6.00E-05
NES15851740	1	178921101	6.89E-05
NES15851750	1	178921643	6.89E-05
NES15851764	1	178922460	6.89E-05
NES15851690	1	178923747	6.89E-05
NES16938219	10	121657770	6.97E-05
NES16938220	10	121657799	6.97E-05
NES16938223	10	121657900	6.97E-05
NES16938225	10	121658060	6.97E-05
NES16937101	10	121714570	6.97E-05
NES16937008	10	121720102	6.97E-05
mm37-10-121721932	10	121721932	6.97E-05
mm37-4-18793387	4	18793387	7.17E-05
mm37-4-127954923:NES09178224	4	127954923	8.11E-05
mm37-11-16303153	11	16303153	8.14E-05
NES08379433	11	16311919	8.14E-05
mm37-11-16314885:NES08379472	11	16314885	8.14E-05
NES09185013	4	127758583	8.14E-05
NES09184977	4	127758889	8.14E-05
NES09184979	4	127758909	8.14E-05
NES17183667	14	29099282	8.32E-05
NES17183670	14	29100658	8.32E-05
MAG9169696:NES09169696	4	126883887	8.60E-05
NES11178924	8	117382015	1.02E-04
NES11165321	8	117624341	1.02E-04
NES15346540	10	121764304	1.13E-04
mm37-10-121655426	10	121655426	1.22E-04
NES16938276	10	121656518	1.22E-04
NES16938226	10	121658235	1.22E-04
NES16938228	10	121658365	1.22E-04
mm37-10-121661260	10	121661260	1.22E-04
mm37-10-121661350	10	121661350	1.22E-04
NES16937186	10	121711611	1.22E-04
NES16937036	10	121716297	1.22E-04
NES16936889	10	121724596	1.22E-04
mm37-10-121728125:NES16936780	10	121728125	1.22E-04

NES16936788	10	121728718	1.22E-04
NES16936693	10	121733018	1.22E-04
NES16936616	10	121736411	1.22E-04
mm37-10-121749980	10	121749980	1.22E-04
mm37-10-121759261:NES15346697	10	121759261	1.22E-04
NES15346666	10	121759840	1.22E-04
NES15346642	10	121761075	1.22E-04
NES15346630	10	121761850	1.22E-04
NES15346472	10	121764883	1.22E-04
NES15346369	10	121768577	1.22E-04
NES15346380	10	121768965	1.22E-04
mm37-14-47879937:NES17232878	14	47879937	1.27E-04
mm37-14-48011506:NES17231909	14	48011506	1.27E-04
mm37-11-16328794:mCV23871121:NES08379183	11	16328794	1.30E-04
NES17232950	14	47865038	1.46E-04
NES14817162	6	73101162	1.49E-04
NES14817169	6	73101303	1.49E-04
NES14817190	6	73102386	1.49E-04
NES14816956	6	73107036	1.49E-04
NES14425710	12	11099565	1.54E-04
NES10674752	1	178545461	1.57E-04
NES10674638	1	178546743	1.57E-04
mm37-6-93813955:gnf06.092.758	6	93813955	1.66E-04
mm37-13-22028735:NES11359412	13	22028735	1.75E-04
mm37-13-22316310	13	22316310	1.75E-04
NES09178582	4	127940749	1.77E-04
NES15515106	13	18348576	1.77E-04
NES15514887	13	17176833	1.82E-04
mm37-16-76655762:NES15743146	16	76655762	1.94E-04
NES16492812	1	153101216	1.95E-04
NES16492814	1	153101306	1.95E-04
NES16492827	1	153101709	1.95E-04
NES16492787	1	153102530	1.95E-04
NES17305693	14	119582336	1.96E-04
NES09185675	4	127745558	1.98E-04
NES09185676	4	127745584	1.98E-04
mm37-13-22327855	13	22327855	2.02E-04
NES09185081	4	127758009	2.05E-04
NES09184983	4	127759127	2.05E-04
NES09184930	4	127759882	2.07E-04
NES09184944	4	127760080	2.07E-04

NES09184947	4	127760123	2.07E-04
NES09184847	4	127760370	2.07E-04
NES09184858	4	127760963	2.07E-04
NES09184862	4	127761251	2.07E-04
NES09184864	4	127761415	2.07E-04
NES09184867	4	127761586	2.07E-04
NES09184868	4	127761631	2.07E-04
NES09184871	4	127762005	2.07E-04
NES09184879	4	127762771	2.07E-04
NES14816673	6	73125480	2.11E-04
NES14815774	6	73186532	2.11E-04
NES14815777	6	73186662	2.11E-04
NES14815780	6	73186693	2.11E-04
NES14815782	6	73186743	2.11E-04
NES14815784	6	73186759	2.11E-04
NES14815787	6	73186839	2.11E-04
NES14815761	6	73187840	2.11E-04
NES14815763	6	73187868	2.11E-04
NES14815723	6	73188775	2.11E-04
NES14815724	6	73188895	2.11E-04
NES14815727	6	73188962	2.11E-04
NES14815734	6	73189129	2.11E-04
NES14815735	6	73189286	2.11E-04
NES14815736	6	73189318	2.11E-04
mm37-13-64937956	13	64937956	2.12E-04
NES11360250	13	22017129	2.13E-04
NES11364725	13	22345864	2.13E-04
mm37-13-22347935	13	22347935	2.13E-04
mm37-13-22348024	13	22348024	2.13E-04
mm37-8-117367834:NES11179508	8	117367834	2.14E-04
mm37-13-22144343	13	22144343	2.15E-04
mm37-8-98286283	8	98286283	2.33E-04
mm37-8-98292310:NES11420353	8	98292310	2.33E-04
NES17183692	14	29102941	2.43E-04
NES17183694	14	29103321	2.43E-04
NES17183698	14	29104227	2.43E-04
NES17183121	14	29126119	2.43E-04
NES17182824	14	29139319	2.43E-04
mm37-4-19656120	4	19656120	2.52E-04
mm37-13-17160425	13	17160425	2.62E-04
mm37-13-17168396:NES15514934	13	17168396	2.62E-04

NES17691934	13	17190071	2.62E-04
NES17691939	13	17190587	2.62E-04
NES17691966	13	17192040	2.62E-04
mm37-13-17201190:NES17691691	13	17201190	2.62E-04
NES17691586	13	17206560	2.62E-04
mm37-11-13365940	11	13365940	2.64E-04
NES16760927	9	34667711	2.66E-04
mm37-9-34669650:NES16760952	9	34669650	2.66E-04
NES16760953	9	34669675	2.66E-04
mm37-9-34670792	9	34670792	2.66E-04
NES10661807	1	178116420	2.73E-04
NES10661756	1	178117136	2.73E-04
NES10661758	1	178117260	2.73E-04
NES10661761	1	178117374	2.73E-04
NES10661766	1	178117639	2.73E-04
NES17186296	14	28984219	2.75E-04
NES15513977	13	19476538	2.90E-04
NES14360451	13	20075225	2.90E-04
NES15520038	13	18836939	2.91E-04
NES15512931	13	19542562	2.91E-04
NES17690748	13	19625576	2.91E-04
NES17690739	13	19627925	2.91E-04
NES14816610	6	73131741	2.92E-04
MAG14261638:NES14261638	9	57571327	2.97E-04
NES14366411	13	19751998	2.97E-04
NES14360324	13	20088740	2.97E-04
NES14420865	12	34384374	3.04E-04
NES14420866	12	34384424	3.04E-04
NES14420867	12	34384517	3.04E-04
NES14420869	12	34384591	3.04E-04
NES13074723	1	153877595	3.06E-04
NES13073998	1	153901847	3.06E-04
NES13073940	1	153904045	3.06E-04
NES13073917	1	153905005	3.06E-04
NES13073867	1	153906913	3.06E-04
NES13073829	1	153907167	3.06E-04
NES13073830	1	153907283	3.06E-04
NES13073832	1	153907395	3.06E-04
NES13073833	1	153907423	3.06E-04
NES13073834	1	153907525	3.06E-04
NES13073837	1	153907807	3.06E-04

NES13073842	1	153908142	3.06E-04
NES13073621	1	153911923	3.06E-04
NES13073175	1	153925670	3.06E-04
NES13073159	1	153926358	3.06E-04
NES13073123	1	153926942	3.06E-04
NES13073117	1	153927594	3.06E-04

A.5 RV END-SYSTOLIC PRESSURE SNP ASSOCIATIONS

Table 11 lists the top 200 SNPs associated with fold change in RV end-systolic pressure (high-fat diet v. regular diet).

Table 11. Top 200 SNPs associated with fold change in RV end-systolic pressure.

SNP	Chrom	Position	*P*-value
NES08383993	11	16688981	5.66E-06
NES14421225	12	34348982	9.70E-06
mm37-12-34367760:NES14421066	12	34367760	9.70E-06
NES14420774	12	34394368	9.70E-06
NES09185662	4	1.28E+08	1.29E-05
NES09185523	4	1.28E+08	1.29E-05
NES08384006	11	16689824	1.61E-05
mm37-12-10580142:rs6209157:NES14428743	12	10580142	1.77E-05
NES09185013	4	1.28E+08	1.90E-05
NES09184977	4	1.28E+08	1.90E-05
NES09184979	4	1.28E+08	1.90E-05
MAG9169696:NES09169696	4	1.27E+08	1.94E-05
NES08383985	11	16688806	2.24E-05
NES08383987	11	16688901	2.24E-05
NES08383996	11	16689319	2.24E-05
NES17305693	14	1.2E+08	2.29E-05
NES09185081	4	1.28E+08	2.62E-05
NES09184983	4	1.28E+08	2.62E-05
mm37-4-127954923:NES09178224	4	1.28E+08	3.15E-05

NES09184930	4	1.28E+08	3.28E-05
NES09184944	4	1.28E+08	3.28E-05
NES09184947	4	1.28E+08	3.28E-05
NES09184847	4	1.28E+08	3.28E-05
NES09184858	4	1.28E+08	3.28E-05
NES09184862	4	1.28E+08	3.28E-05
NES09184864	4	1.28E+08	3.28E-05
NES09184867	4	1.28E+08	3.28E-05
NES09184868	4	1.28E+08	3.28E-05
NES09184871	4	1.28E+08	3.28E-05
NES09184879	4	1.28E+08	3.28E-05
NES15851806	1	1.79E+08	3.29E-05
NES15851754	1	1.79E+08	3.29E-05
NES15851706	1	1.79E+08	3.29E-05
NES15851678	1	1.79E+08	3.29E-05
NES15851697	1	1.79E+08	3.29E-05
NES15851700	1	1.79E+08	3.29E-05
NES08383994	11	16689147	3.43E-05
NES08384007	11	16690201	3.43E-05
NES08384013	11	16690515	3.43E-05
NES11178924	8	1.17E+08	4.10E-05
NES11165321	8	1.18E+08	4.10E-05
NES09185675	4	1.28E+08	4.11E-05
NES09185676	4	1.28E+08	4.11E-05
mm37-6-94065571	6	94065571	4.29E-05
mm37-6-93865234:NES13736033	6	93865234	4.53E-05
NES14366459	13	19750561	4.91E-05
NES14366409	13	19751818	4.91E-05
NES14366412	13	19752054	4.91E-05
NES14366414	13	19752097	4.91E-05
NES14366415	13	19752115	4.91E-05
NES14366416	13	19752284	4.91E-05
NES16938219	10	1.22E+08	4.94E-05
NES16938220	10	1.22E+08	4.94E-05
NES16938223	10	1.22E+08	4.94E-05
NES16938225	10	1.22E+08	4.94E-05
NES16937101	10	1.22E+08	4.94E-05
NES16937008	10	1.22E+08	4.94E-05
mm37-10-121721932	10	1.22E+08	4.94E-05
NES08384117	11	16685717	5.04E-05
NES08384120	11	16685917	5.04E-05

NES08384100	11	16686440	5.04E-05
NES08384102	11	16686785	5.04E-05
mm37-8-98286283	8	98286283	5.33E-05
mm37-8-98292310:NES11420353	8	98292310	5.33E-05
NES14817172	6	73101326	5.39E-05
NES15514887	13	17176833	5.55E-05
mm37-13-22028735:NES11359412	13	22028735	5.65E-05
mm37-13-22316310	13	22316310	5.65E-05
NES16492812	1	1.53E+08	5.70E-05
NES16492814	1	1.53E+08	5.70E-05
NES16492827	1	1.53E+08	5.70E-05
NES16492787	1	1.53E+08	5.70E-05
NES15519226	13	19181316	6.00E-05
NES15518974	13	19197798	6.00E-05
NES09178582	4	1.28E+08	6.16E-05
NES17183667	14	29099282	6.17E-05
NES17183670	14	29100658	6.17E-05
mm37-13-22327855	13	22327855	7.11E-05
NES11419812	8	99211368	7.13E-05
mm37-11-16690559:NES08384017	11	16690559	7.46E-05
mm37-16-76655762:NES15743146	16	76655762	7.60E-05
NES11360250	13	22017129	7.81E-05
NES11364725	13	22345864	7.81E-05
mm37-13-22347935	13	22347935	7.81E-05
mm37-13-22348024	13	22348024	7.81E-05
mm37-13-22144343	13	22144343	7.90E-05
NES17691474	13	37065600	8.30E-05
NES15520038	13	18836939	8.33E-05
NES15512931	13	19542562	8.33E-05
NES17690748	13	19625576	8.33E-05
NES17690739	13	19627925	8.33E-05
NES08439654	11	52956630	8.44E-05
NES09187852	4	1.28E+08	8.77E-05
NES09187859	4	1.28E+08	8.77E-05
NES09187735	4	1.28E+08	8.77E-05
NES09187590	4	1.28E+08	8.77E-05
NES09187592	4	1.28E+08	8.77E-05
NES09187285	4	1.28E+08	8.77E-05
NES09187139	4	1.28E+08	8.77E-05
NES09187099	4	1.28E+08	8.77E-05
NES08439704	11	52954210	8.84E-05

NES08439705	11	52954359	8.84E-05
NES08439683	11	52955060	8.84E-05
NES08439660	11	52955682	8.84E-05
NES08439616	11	52958722	8.84E-05
NES08439618	11	52958844	8.84E-05
NES08439321	11	52987026	8.84E-05
NES08439123	11	52999509	8.84E-05
mm37-4-18793387	4	18793387	8.84E-05
NES08442698	11	52798580	9.08E-05
NES08441723	11	52861291	9.08E-05
NES08441652	11	52865375	9.08E-05
NES08441665	11	52865937	9.08E-05
NES08440934	11	52897170	9.08E-05
NES15514295	13	17267731	9.12E-05
NES15514301	13	17267902	9.12E-05
NES15514071	13	17275014	9.12E-05
NES15514041	13	17278967	9.12E-05
NES15513953	13	17280725	9.12E-05
NES15513869	13	17286287	9.12E-05
NES15513456	13	17324957	9.12E-05
NES15512972	13	18463915	9.12E-05
mm37-13-18471100:NES15512895	13	18471100	9.12E-05
NES15512768	13	18472898	9.12E-05
NES15512307	13	18490811	9.12E-05
NES15512261	13	18492987	9.12E-05
NES15512187	13	18494508	9.12E-05
NES17685103	13	18853315	9.12E-05
NES17685110	13	18854268	9.12E-05
NES17685111	13	18854453	9.12E-05
NES17685071	13	18856438	9.12E-05
NES15513977	13	19476538	9.13E-05
NES14360451	13	20075225	9.13E-05
NES15514199	13	17269782	9.17E-05
NES15513015	13	18461851	9.17E-05
NES11359217	13	22032386	9.57E-05
NES15515106	13	18348576	9.86E-05
NES13074723	1	1.54E+08	1.02E-04
NES13073998	1	1.54E+08	1.02E-04
NES13073940	1	1.54E+08	1.02E-04
NES13073917	1	1.54E+08	1.02E-04
NES13073867	1	1.54E+08	1.02E-04

NES13073829	1	1.54E+08	1.02E-04
NES13073830	1	1.54E+08	1.02E-04
NES13073832	1	1.54E+08	1.02E-04
NES13073833	1	1.54E+08	1.02E-04
NES13073834	1	1.54E+08	1.02E-04
NES13073837	1	1.54E+08	1.02E-04
NES13073842	1	1.54E+08	1.02E-04
NES13073621	1	1.54E+08	1.02E-04
NES13073175	1	1.54E+08	1.02E-04
NES13073159	1	1.54E+08	1.02E-04
NES13073123	1	1.54E+08	1.02E-04
NES13073117	1	1.54E+08	1.02E-04
NES13073067	1	1.54E+08	1.02E-04
NES13073073	1	1.54E+08	1.02E-04
NES13072951	1	1.54E+08	1.02E-04
NES13072170	1	1.54E+08	1.02E-04
NES13072176	1	1.54E+08	1.02E-04
NES13072095	1	1.54E+08	1.02E-04
NES13071844	1	1.54E+08	1.02E-04
NES13067163	1	1.54E+08	1.02E-04
NES15851740	1	1.79E+08	1.07E-04
NES15851750	1	1.79E+08	1.07E-04
NES15851764	1	1.79E+08	1.07E-04
NES15851690	1	1.79E+08	1.07E-04
NES09184985	4	1.28E+08	1.13E-04
NES09184989	4	1.28E+08	1.13E-04
NES09184932	4	1.28E+08	1.13E-04
NES09184936	4	1.28E+08	1.13E-04
NES09184852	4	1.28E+08	1.13E-04
NES09184863	4	1.28E+08	1.13E-04
NES09184872	4	1.28E+08	1.13E-04
NES15346540	10	1.22E+08	1.13E-04
mm37-13-17160425	13	17160425	1.17E-04
mm37-13-17168396:NES15514934	13	17168396	1.17E-04
NES17691934	13	17190071	1.17E-04
NES17691939	13	17190587	1.17E-04
NES17691966	13	17192040	1.17E-04
mm37-13-17201190:NES17691691	13	17201190	1.17E-04
NES17691586	13	17206560	1.17E-04
NES11419814	8	99211450	1.19E-04
NES11419822	8	99211690	1.19E-04

mm37-8-117367834:NES11179508	8	1.17E+08	1.20E-04
mm37-11-16303153	11	16303153	1.26E-04
NES08379433	11	16311919	1.26E-04
mm37-11-16314885:NES08379472	11	16314885	1.26E-04
mm37-4-127784232	4	1.28E+08	1.39E-04
NES15512252	13	18492314	1.44E-04
NES15512276	13	18493445	1.44E-04
NES15512164	13	18493732	1.44E-04
mm37-13-18494573:NES15512190	13	18494573	1.44E-04
NES15511111	13	18557054	1.44E-04
mm37-13-19488036:rs6345767	13	19488036	1.48E-04
mm37-13-19545618	13	19545618	1.48E-04
mm37-13-19546769:NES15512873	13	19546769	1.48E-04
mm37-13-18862634	13	18862634	1.50E-04
NES16796293	9	67422344	1.59E-04
NES14816673	6	73125480	1.63E-04
NES14815774	6	73186532	1.63E-04

BIBLIOGRAPHY

1. George, M.G., et al., *Pulmonary hypertension surveillance: United States, 2001 to 2010.* Chest, 2014. **146**(2): p. 476-95.

2. Humbert, M., et al., *Pulmonary arterial hypertension in France: results from a national registry.* Am J Respir Crit Care Med, 2006. **173**(9): p. 1023-30.

3. Ling, Y., et al., *Changing demographics, epidemiology, and survival of incident pulmonary arterial hypertension: results from the pulmonary hypertension registry of the United Kingdom and Ireland.* Am J Respir Crit Care Med, 2012. **186**(8): p. 790-6.

4. Badesch, D.B., et al., *Pulmonary arterial hypertension: baseline characteristics from the REVEAL Registry.* Chest, 2010. **137**(2): p. 376-87.

5. Thenappan, T., et al., *A USA-based registry for pulmonary arterial hypertension: 1982-2006.* Eur Respir J, 2007. **30**(6): p. 1103-10.

6. Hoeper, M.M., et al., *Definitions and diagnosis of pulmonary hypertension.* J Am Coll Cardiol, 2013. **62**(25 Suppl): p. D42-50.

7. Simonneau, G., et al., *Updated clinical classification of pulmonary hypertension.* J Am Coll Cardiol, 2013. **62**(25 Suppl): p. D34-41.

8. Lai, Y.C., et al., *Pulmonary arterial hypertension: the clinical syndrome.* Circ Res, 2014. **115**(1): p. 115-30.

9. Giaid, A., et al., *Expression of endothelin-1 in the lungs of patients with pulmonary hypertension.* N Engl J Med, 1993. **328**(24): p. 1732-9.

10. Giaid, A. and D. Saleh, *Reduced expression of endothelial nitric oxide synthase in the lungs of patients with pulmonary hypertension.* N Engl J Med, 1995. **333**(4): p. 214-21.

11. Ward, J.P. and I.F. McMurtry, *Mechanisms of hypoxic pulmonary vasoconstriction and their roles in pulmonary hypertension: new findings for an old problem.* Curr Opin Pharmacol, 2009. **9**(3): p. 287-96.

12. Tonelli, A.R., et al., *Causes and circumstances of death in pulmonary arterial hypertension.* Am J Respir Crit Care Med, 2013. **188**(3): p. 365-9.

13. Pietra, G.G., et al., *Pathologic assessment of vasculopathies in pulmonary hypertension.* J Am Coll Cardiol, 2004. **43**(12 Suppl S): p. 25S-32S.

14. Robbins, S.L., V. Kumar, and R.S. Cotran, *Robbins and Cotran pathologic basis of disease*. 2010, Philadelphia, PA: Saunders/Elsevier.

15. Wright, J.L., et al., *The structure and function of the pulmonary vasculature in mild chronic obstructive pulmonary disease. The effect of oxygen and exercise.* Am Rev Respir Dis, 1983. **128**(4): p. 702-7.

16. Gibbons, G.H. and V.J. Dzau, *The emerging concept of vascular remodeling.* N Engl J Med, 1994. **330**(20): p. 1431-8.

17. Clozel, J.P., et al., *Effects of cilazapril, a novel angiotensin converting enzyme inhibitor, on the structure of pulmonary arteries of rats exposed to chronic hypoxia.* J Cardiovasc Pharmacol, 1991. **17**(1): p. 36-40.

18. Austin, E.D. and J.E. Loyd, *The genetics of pulmonary arterial hypertension.* Circ Res, 2014. **115**(1): p. 189-202.

19. International, P.P.H.C., et al., *Heterozygous germline mutations in BMPR2, encoding a TGF-beta receptor, cause familial primary pulmonary hypertension.* Nat Genet, 2000. **26**(1): p. 81-4.

20. Deng, Z., et al., *Familial primary pulmonary hypertension (gene PPH1) is caused by mutations in the bone morphogenetic protein receptor-II gene.* Am J Hum Genet, 2000. **67**(3): p. 737-44.

21. Harrison, R.E., et al., *Molecular and functional analysis identifies ALK-1 as the predominant cause of pulmonary hypertension related to hereditary haemorrhagic telangiectasia.* J Med Genet, 2003. **40**(12): p. 865-71.

22. Shintani, M., et al., *A new nonsense mutation of SMAD8 associated with pulmonary arterial hypertension.* J Med Genet, 2009. **46**(5): p. 331-7.

23. Austin, E.D., et al., *Whole exome sequencing to identify a novel gene (caveolin-1) associated with human pulmonary arterial hypertension.* Circ Cardiovasc Genet, 2012. **5**(3): p. 336-43.

24. Ma, L., et al., *A novel channelopathy in pulmonary arterial hypertension.* N Engl J Med, 2013. **369**(4): p. 351-61.

25. Eyries, M., et al., *EIF2AK4 mutations cause pulmonary veno-occlusive disease, a recessive form of pulmonary hypertension.* Nat Genet, 2014. **46**(1): p. 65-9.

26. Best, D.H., et al., *EIF2AK4 mutations in pulmonary capillary hemangiomatosis.* Chest, 2014. **145**(2): p. 231-6.

27. Germain, M., et al., *Genome-wide association analysis identifies a susceptibility locus for pulmonary arterial hypertension.* Nat Genet, 2013. **45**(5): p. 518-21.

28. Wojciak-Stothard, B., et al., *Role of RhoB in the regulation of pulmonary endothelial and smooth muscle cell responses to hypoxia.* Circ Res, 2012. **110**(11): p. 1423-34.

29. Gerthoffer, W.T., *Mechanisms of vascular smooth muscle cell migration.* Circ Res, 2007. **100**(5): p. 607-21.

30. Shimoda, L.A. and S.S. Laurie, *Vascular remodeling in pulmonary hypertension.* J Mol Med (Berl), 2013. **91**(3): p. 297-309.

31. Miyazono, K., K. Kusanagi, and H. Inoue, *Divergence and convergence of TGF-beta/BMP signaling.* J Cell Physiol, 2001. **187**(3): p. 265-76.

32. Rosenzweig, B.L., et al., *Cloning and characterization of a human type II receptor for bone morphogenetic proteins.* Proc Natl Acad Sci U S A, 1995. **92**(17): p. 7632-6.

33. David, L., et al., *Identification of BMP9 and BMP10 as functional activators of the orphan activin receptor-like kinase 1 (ALK1) in endothelial cells.* Blood, 2007. **109**(5): p. 1953-61.

34. Massague, J., J. Seoane, and D. Wotton, *Smad transcription factors.* Genes Dev, 2005. **19**(23): p. 2783-810.

35. Morrell, N.W., et al., *Cellular and molecular basis of pulmonary arterial hypertension.* J Am Coll Cardiol, 2009. **54**(1 Suppl): p. S20-31.

36. Yuan, J.X., et al., *Dysfunctional voltage-gated K+ channels in pulmonary artery smooth muscle cells of patients with primary pulmonary hypertension.* Circulation, 1998. **98**(14): p. 1400-6.

37. Suzuki, H. and B.M. Twarog, *Membrane properties of smooth muscle cells in pulmonary hypertensive rats.* Am J Physiol, 1982. **242**(5): p. H907-15.

38. Shimoda, L.A. and J. Polak, *Hypoxia. 4. Hypoxia and ion channel function.* Am J Physiol Cell Physiol, 2011. **300**(5): p. C951-67.

39. Bortner, C.D., F.M. Hughes, Jr., and J.A. Cidlowski, *A primary role for K+ and Na+ efflux in the activation of apoptosis.* J Biol Chem, 1997. **272**(51): p. 32436-42.

40. Maeno, E., et al., *Normotonic cell shrinkage because of disordered volume regulation is an early prerequisite to apoptosis.* Proc Natl Acad Sci U S A, 2000. **97**(17): p. 9487-92.

41. Hughes, F.M., Jr., et al., *Intracellular K+ suppresses the activation of apoptosis in lymphocytes.* J Biol Chem, 1997. **272**(48): p. 30567-76.

42. Dallaporta, B., et al., *Potassium leakage during the apoptotic degradation phase.* J Immunol, 1998. **160**(11): p. 5605-15.

43. McMurtry, M.S., et al., *Dichloroacetate prevents and reverses pulmonary hypertension by inducing pulmonary artery smooth muscle cell apoptosis.* Circ Res, 2004. **95**(8): p. 830-40.

44. Michelakis, E.D., et al., *Dichloroacetate, a metabolic modulator, prevents and reverses chronic hypoxic pulmonary hypertension in rats: role of increased expression and activity of voltage-gated potassium channels.* Circulation, 2002. **105**(2): p. 244-50.

45. Bonnet, S., et al., *Dehydroepiandrosterone (DHEA) prevents and reverses chronic hypoxic pulmonary hypertension.* Proc Natl Acad Sci U S A, 2003. **100**(16): p. 9488-93.

46. Golovina, V.A., et al., *Upregulated TRP and enhanced capacitative Ca(2+) entry in human pulmonary artery myocytes during proliferation.* Am J Physiol Heart Circ Physiol, 2001. **280**(2): p. H746-55.

47. Landsberg, J.W. and J.X. Yuan, *Calcium and TRP channels in pulmonary vascular smooth muscle cell proliferation.* News Physiol Sci, 2004. **19**: p. 44-50.

48. Song, M.Y., A. Makino, and J.X. Yuan, *STIM2 Contributes to Enhanced Store-operated Ca Entry in Pulmonary Artery Smooth Muscle Cells from Patients with Idiopathic Pulmonary Arterial Hypertension.* Pulm Circ, 2011. **1**(1): p. 84-94.

49. Rabinovitch, M., et al., *Inflammation and immunity in the pathogenesis of pulmonary arterial hypertension.* Circ Res, 2014. **115**(1): p. 165-75.

50. MacLean, M.R. and Y. Dempsie, *The Serotonin Hypothesis of Pulmonary Hypertension Revisited.* 2010. **661**: p. 309-322.

51. Yu, Y., et al., *A functional single-nucleotide polymorphism in the TRPC6 gene promoter associated with idiopathic pulmonary arterial hypertension.* Circulation, 2009. **119**(17): p. 2313-22.

52. Yu, Y., et al., *Enhanced expression of transient receptor potential channels in idiopathic pulmonary arterial hypertension.* Proc Natl Acad Sci U S A, 2004. **101**(38): p. 13861-6.

53. Kunichika, N., et al., *Bosentan inhibits transient receptor potential channel expression in pulmonary vascular myocytes.* Am J Respir Crit Care Med, 2004. **170**(10): p. 1101-7.

54. Lin, M.J., et al., *Chronic hypoxia-induced upregulation of store-operated and receptor-operated Ca2+ channels in pulmonary arterial smooth muscle cells: a novel mechanism of hypoxic pulmonary hypertension.* Circ Res, 2004. **95**(5): p. 496-505.

55. Kuhr, F.K., et al., *New mechanisms of pulmonary arterial hypertension: role of Ca(2)(+) signaling.* Am J Physiol Heart Circ Physiol, 2012. **302**(8): p. H1546-62.

56. Bonnet, S., et al., *The nuclear factor of activated T cells in pulmonary arterial hypertension can be therapeutically targeted.* Proc Natl Acad Sci U S A, 2007. **104**(27): p. 11418-23.

57. Semenza, G.L. and G.L. Wang, *A nuclear factor induced by hypoxia via de novo protein synthesis binds to the human erythropoietin gene enhancer at a site required for transcriptional activation.* Mol Cell Biol, 1992. **12**(12): p. 5447-54.

58. Prabhakar, N.R. and G.L. Semenza, *Adaptive and maladaptive cardiorespiratory responses to continuous and intermittent hypoxia mediated by hypoxia-inducible factors 1 and 2.* Physiol Rev, 2012. **92**(3): p. 967-1003.

59. Semenza, G.L., *Pulmonary vascular responses to chronic hypoxia mediated by hypoxia-inducible factor 1.* Proc Am Thorac Soc, 2005. **2**(1): p. 68-70.

60. Yu, A.Y., et al., *Impaired physiological responses to chronic hypoxia in mice partially deficient for hypoxia-inducible factor 1alpha.* J Clin Invest, 1999. **103**(5): p. 691-6.

61. Brusselmans, K., et al., *Heterozygous deficiency of hypoxia-inducible factor-2alpha protects mice against pulmonary hypertension and right ventricular dysfunction during prolonged hypoxia.* J Clin Invest, 2003. **111**(10): p. 1519-27.

62. Wang, J., et al., *Hypoxia inducible factor 1 mediates hypoxia-induced TRPC expression and elevated intracellular Ca2+ in pulmonary arterial smooth muscle cells.* Circ Res, 2006. **98**(12): p. 1528-37.

63. Bertero, T., et al., *The microRNA-130/301 family controls vasoconstriction in pulmonary hypertension.* J Biol Chem, 2015. **290**(4): p. 2069-85.

64. Bertero, T., et al., *Systems-level regulation of microRNA networks by miR-130/301 promotes pulmonary hypertension.* J Clin Invest, 2014. **124**(8): p. 3514-28.

65. Mulvany, M.J., *Small artery remodeling and significance in the development of hypertension.* News Physiol Sci, 2002. **17**: p. 105-9.

66. Farber, H.W. and J. Loscalzo, *Pulmonary arterial hypertension.* N Engl J Med, 2004. **351**(16): p. 1655-65.

67. Tuder, R.M., et al., *Development and pathology of pulmonary hypertension.* J Am Coll Cardiol, 2009. **54**(1 Suppl): p. S3-9.

68. Schermuly, R.T., et al., *Mechanisms of disease: pulmonary arterial hypertension.* Nat Rev Cardiol, 2011. **8**(8): p. 443-55.

69. Ghodsi, F. and J.A. Will, *Changes in pulmonary structure and function induced by monocrotaline intoxication.* Am J Physiol, 1981. **240**(2): p. H149-55.

70. Teoh, H., et al., *Impaired endothelial function in C-reactive protein overexpressing mice.* Atherosclerosis, 2008. **201**(2): p. 318-25.

71. Taraseviciene-Stewart, L., et al., *Inhibition of the VEGF receptor 2 combined with chronic hypoxia causes cell death-dependent pulmonary endothelial cell proliferation and severe pulmonary hypertension.* FASEB J, 2001. **15**(2): p. 427-38.

72. Vitali, S.H., et al., *The Sugen 5416/hypoxia mouse model of pulmonary hypertension revisited: long-term follow-up.* Pulm Circ, 2014. **4**(4): p. 619-29.

73. Kelley, E.E., et al., *Fatty acid nitroalkenes ameliorate glucose intolerance and pulmonary hypertension in high-fat diet-induced obesity.* Cardiovasc Res, 2014. **101**(3): p. 352-63.

74. Goncharov, D.A., et al., *Mammalian target of rapamycin complex 2 (mTORC2) coordinates pulmonary artery smooth muscle cell metabolism, proliferation, and survival in pulmonary arterial hypertension.* Circulation, 2014. **129**(8): p. 864-74.

75. Bland, J.M. and D.G. Altman, *Statistical methods for assessing agreement between two methods of clinical measurement.* Lancet, 1986. **1**(8476): p. 307-10.

76. Székely, G.J. and M.L. Rizzo, *Brownian distance covariance.* The Annals of Applied Statistics, 2009. **3**(4): p. 1236-1265.

77. Ciuclan, L., et al., *A novel murine model of severe pulmonary arterial hypertension.* Am J Respir Crit Care Med, 2011. **184**(10): p. 1171-82.

78. Gonzalez, R.C. and R.E. Woods, *Digital Image Processing*. 2001: Addison-Wesley Longman Publishing Co., Inc. 793.

79. Schneider, C.A., W.S. Rasband, and K.W. Eliceiri, *NIH Image to ImageJ: 25 years of image analysis.* Nat Methods, 2012. **9**(7): p. 671-5.

80. Goodman, A.W. and G. Goodman, *Generalizations of the Theorems of Pappus.* The American Mathematical Monthly, 1969. **76**(4): p. 355-366.

81. Caro, C.G. and P.G. Saffman, *Extensibility of Blood Vessels in Isolated Rabbit Lungs.* J Physiol, 1965. **178**: p. 193-210.

82. Wang, D.C., et al., *Fully automated common carotid artery and internal jugular vein identification and tracking using B-mode ultrasound.* IEEE Trans Biomed Eng, 2009. **56**(6): p. 1691-9.

83. Peterson, L.H., R.E. Jensen, and J. Parnell, *Mechanical Properties of Arteries in Vivo.* Circulation Research, 1960. **8**(3): p. 622-639.

84. Hearn, E.J., *Mechanics of Materials Volume 1: An Introduction to the Mechanics of Elastic and Plastic Deformation of Solids and Structural Materials*. 1997: Elsevier Science.

85. Pries, A.R., B. Reglin, and T.W. Secomb, *Remodeling of blood vessels: responses of diameter and wall thickness to hemodynamic and metabolic stimuli.* Hypertension, 2005. **46**(4): p. 725-31.

86. Rakusan, K. and P. Wicker, *Morphometry of the small arteries and arterioles in the rat heart: effects of chronic hypertension and exercise.* Cardiovasc Res, 1990. **24**(4): p. 278-84.

87. Barth, P.J., et al., *An improved mathematical approach for the assessment of the medial thickness of pulmonary arteries.* Pathol Res Pract, 1993. **189**(5): p. 567-76.

88. Cook, T.A. and P.O. Yates, *A critical survey of techniques for arterial mensuration.* J Pathol, 1972. **108**(2): p. 119-27.

89. Lowe, J., *Method for the morphometric analysis of arterial structure.* J Clin Pathol, 1984. **37**(12): p. 1413-5.

90. Townsley, M.I., *Structure and composition of pulmonary arteries, capillaries, and veins.* Compr Physiol, 2012. **2**(1): p. 675-709.

91. Siegel, R., D. Naishadham, and A. Jemal, *Cancer statistics, 2012.* CA Cancer J Clin, 2012. **62**(1): p. 10-29.

92. Herbst, R.S., J.V. Heymach, and S.M. Lippman, *Lung cancer.* N Engl J Med, 2008. **359**(13): p. 1367-80.

93. Parks, W.C. and S.D. Shapiro, *Matrix metalloproteinases in lung biology.* Respir Res, 2001. **2**(1): p. 10-9.

94. Hautamaki, R.D., et al., *Requirement for macrophage elastase for cigarette smoke-induced emphysema in mice.* Science, 1997. **277**(5334): p. 2002-4.

95. Shapiro, S.D., *Proteinases in chronic obstructive pulmonary disease.* Biochem Soc Trans, 2002. **30**(2): p. 98-102.

96. Shapiro, S.D., *Proteolysis in the lung.* Eur Respir J Suppl, 2003. **44**: p. 30s-32s.

97. Kessenbrock, K., V. Plaks, and Z. Werb, *Matrix metalloproteinases: regulators of the tumor microenvironment.* Cell, 2010. **141**(1): p. 52-67.

98. Houghton, A.M., et al., *Macrophage elastase (matrix metalloproteinase-12) suppresses growth of lung metastases.* Cancer Res, 2006. **66**(12): p. 6149-55.

99. Acuff, H.B., et al., *Analysis of host- and tumor-derived proteinases using a custom dual species microarray reveals a protective role for stromal matrix metalloproteinase-12 in non-small cell lung cancer.* Cancer Res, 2006. **66**(16): p. 7968-75.

100. Egeblad, M. and Z. Werb, *New functions for the matrix metalloproteinases in cancer progression.* Nat Rev Cancer, 2002. **2**(3): p. 161-74.

101. Chambers, A.F. and L.M. Matrisian, *Changing views of the role of matrix metalloproteinases in metastasis.* J Natl Cancer Inst, 1997. **89**(17): p. 1260-70.

102. Stetler-Stevenson, W.G. and A.E. Yu, *Proteases in invasion: matrix metalloproteinases.* Semin Cancer Biol, 2001. **11**(2): p. 143-52.

103. Li, Q., et al., *Matrilysin shedding of syndecan-1 regulates chemokine mobilization and transepithelial efflux of neutrophils in acute lung injury.* Cell, 2002. **111**(5): p. 635-46.

104. McQuibban, G.A., et al., *Matrix metalloproteinase activity inactivates the CXC chemokine stromal cell-derived factor-1.* J Biol Chem, 2001. **276**(47): p. 43503-8.

105. Fang, J., et al., *Matrix metalloproteinase-2 is required for the switch to the angiogenic phenotype in a tumor model.* Proc Natl Acad Sci U S A, 2000. **97**(8): p. 3884-9.

106. Bergers, G., et al., *Matrix metalloproteinase-9 triggers the angiogenic switch during carcinogenesis.* Nat Cell Biol, 2000. **2**(10): p. 737-44.

107. Fidler, I.J. and L.M. Ellis, *The implications of angiogenesis for the biology and therapy of cancer metastasis.* Cell, 1994. **79**(2): p. 185-8.

108. Kondraganti, S., et al., *Selective suppression of matrix metalloproteinase-9 in human glioblastoma cells by antisense gene transfer impairs glioblastoma cell invasion.* Cancer Res, 2000. **60**(24): p. 6851-5.

109. Yonemura, Y., et al., *Inhibition of peritoneal dissemination in human gastric cancer by MMP-7-specific antisense oligonucleotide.* J Exp Clin Cancer Res, 2001. **20**(2): p. 205-12.

110. Moore, M.J., et al., *Comparison of gemcitabine versus the matrix metalloproteinase inhibitor BAY 12-9566 in patients with advanced or metastatic adenocarcinoma of the pancreas: a phase III trial of the National Cancer Institute of Canada Clinical Trials Group.* J Clin Oncol, 2003. **21**(17): p. 3296-302.

111. Zucker, S., J. Cao, and W.T. Chen, *Critical appraisal of the use of matrix metalloproteinase inhibitors in cancer treatment.* Oncogene, 2000. **19**(56): p. 6642-50.

112. Woodruff, P.G., et al., *A distinctive alveolar macrophage activation state induced by cigarette smoking.* Am J Respir Crit Care Med, 2005. **172**(11): p. 1383-92.

113. Hofmann, H.S., et al., *Identification and classification of differentially expressed genes in non-small cell lung cancer by expression profiling on a global human 59.620-element oligonucleotide array.* Oncol Rep, 2006. **16**(3): p. 587-95.

114. Hofmann, H.S., et al., *Matrix metalloproteinase-12 expression correlates with local recurrence and metastatic disease in non-small cell lung cancer patients.* Clin Cancer Res, 2005. **11**(3): p. 1086-92.

115. Scherf, D.B., et al., *Single nucleotide polymorphisms in matrix metalloproteinase genes and lung cancer chemotherapy response and prognosis.* Eur Respir J, 2010. **35**(2): p. 381-90.

116. Ferreras, M., et al., *Generation and degradation of human endostatin proteins by various proteinases.* FEBS Lett, 2000. **486**(3): p. 247-51.

117. Cornelius, L.A., et al., *Matrix metalloproteinases generate angiostatin: effects on neovascularization.* J Immunol, 1998. **161**(12): p. 6845-52.

118. Houghton, A.M., et al., *Macrophage elastase kills bacteria within murine macrophages.* Nature, 2009. **460**(7255): p. 637-41.

119. Stabile, L.P., et al., *Human non-small cell lung tumors and cells derived from normal lung express both estrogen receptor alpha and beta and show biological responses to estrogen.* Cancer Res, 2002. **62**(7): p. 2141-50.

120. Gandhi, L., et al., *Sunitinib prolongs survival in genetically engineered mouse models of multistep lung carcinogenesis.* Cancer Prev Res (Phila), 2009. **2**(4): p. 330-7.

121. Yasuoka, H., et al., *Insulin-like growth factor-binding protein-5 induces pulmonary fibrosis and triggers mononuclear cellular infiltration.* Am J Pathol, 2006. **169**(5): p. 1633-42.

122. Nenan, S., et al., *Analysis of the inflammatory response induced by rhMMP-12 catalytic domain instilled in mouse airways.* Int Immunopharmacol, 2005. **5**(3): p. 511-24.

123. Wang, Q., et al., *Isolation and molecular characterization of the 5'-upstream region of the human TRAIL gene.* Biochem Biophys Res Commun, 2000. **276**(2): p. 466-71.

124. Shipley, J.M., et al., *Metalloelastase is required for macrophage-mediated proteolysis and matrix invasion in mice.* Proc Natl Acad Sci U S A, 1996. **93**(9): p. 3942-6.

125. Jackson, E.L., et al., *Analysis of lung tumor initiation and progression using conditional expression of oncogenic K-ras.* Genes Dev, 2001. **15**(24): p. 3243-8.

126. Raza, S.L., et al., *Proteinase-activated receptor-1 regulation of macrophage elastase (MMP-12) secretion by serine proteinases.* J Biol Chem, 2000. **275**(52): p. 41243-50.

127. Shapiro, S.D., D.K. Kobayashi, and T.J. Ley, *Cloning and characterization of a unique elastolytic metalloproteinase produced by human alveolar macrophages.* J Biol Chem, 1993. **268**(32): p. 23824-9.

128. Wiley, S.R., et al., *Identification and characterization of a new member of the TNF family that induces apoptosis.* Immunity, 1995. **3**(6): p. 673-82.

129. Mariani, S.M., et al., *Interleukin 1 beta-converting enzyme related proteases/caspases are involved in TRAIL-induced apoptosis of myeloma and leukemia cells.* J Cell Biol, 1997. **137**(1): p. 221-9.

130. Pan, G., et al., *An antagonist decoy receptor and a death domain-containing receptor for TRAIL.* Science, 1997. **277**(5327): p. 815-8.

131. Pan, G., et al., *The receptor for the cytotoxic ligand TRAIL.* Science, 1997. **276**(5309): p. 111-3.

132. Marchant, D.J., et al., *A new transcriptional role for matrix metalloproteinase-12 in antiviral immunity.* Nat Med, 2014. **20**(5): p. 493-502.

133. Hao, C., et al., *Modulation of TRAIL signaling complex.* Vitam Horm, 2004. **67**: p. 81-99.

134. Medema, J.P., et al., *FLICE is activated by association with the CD95 death-inducing signaling complex (DISC).* EMBO J, 1997. **16**(10): p. 2794-804.

135. Li, H., et al., *Cleavage of BID by caspase 8 mediates the mitochondrial damage in the Fas pathway of apoptosis.* Cell, 1998. **94**(4): p. 491-501.

136. Li, P., et al., *Cytochrome c and dATP-dependent formation of Apaf-1/caspase-9 complex initiates an apoptotic protease cascade.* Cell, 1997. **91**(4): p. 479-89.

137. Luo, X., et al., *Bid, a Bcl2 interacting protein, mediates cytochrome c release from mitochondria in response to activation of cell surface death receptors.* Cell, 1998. **94**(4): p. 481-90.

138. Lieber, M., et al., *A continuous tumor-cell line from a human lung carcinoma with properties of type II alveolar epithelial cells.* Int J Cancer, 1976. **17**(1): p. 62-70.

139. Scaffidi, C., et al., *Two CD95 (APO-1/Fas) signaling pathways.* EMBO J, 1998. **17**(6): p. 1675-87.

140. Song, J.H., et al., *Lipid rafts and nonrafts mediate tumor necrosis factor related apoptosis-inducing ligand induced apoptotic and nonapoptotic signals in non small cell lung carcinoma cells.* Cancer Res, 2007. **67**(14): p. 6946-55.

141. Yang, E., et al., *Bad, a heterodimeric partner for Bcl-XL and Bcl-2, displaces Bax and promotes cell death.* Cell, 1995. **80**(2): p. 285-91.

142. Deveraux, Q.L. and J.C. Reed, *IAP family proteins--suppressors of apoptosis.* Genes Dev, 1999. **13**(3): p. 239-52.

143. Boise, L.H., et al., *bcl-x, a bcl-2-related gene that functions as a dominant regulator of apoptotic cell death.* Cell, 1993. **74**(4): p. 597-608.

144. Zhu, H., et al., *Enhancing TRAIL-induced apoptosis by Bcl-X(L) siRNA.* Cancer Biol Ther, 2005. **4**(4): p. 393-7.

145. Taghiyev, A.F., et al., *Overexpression of BAD potentiates sensitivity to tumor necrosis factor-related apoptosis-inducing ligand treatment in the prostatic carcinoma cell line LNCaP.* Mol Cancer Res, 2003. **1**(7): p. 500-7.

146. Chawla-Sarkar, M., et al., *Downregulation of Bcl-2, FLIP or IAPs (XIAP and survivin) by siRNAs sensitizes resistant melanoma cells to Apo2L/TRAIL-induced apoptosis.* Cell Death Differ, 2004. **11**(8): p. 915-23.

147. Kataoka, T. and J. Tschopp, *N-terminal fragment of c-FLIP(L) processed by caspase 8 specifically interacts with TRAF2 and induces activation of the NF-kappaB signaling pathway.* Mol Cell Biol, 2004. **24**(7): p. 2627-36.

148. Lemke, J., et al., *Getting TRAIL back on track for cancer therapy.* Cell Death Differ, 2014. **21**(9): p. 1350-64.

149. Gajewski, T.F., *On the TRAIL toward death receptor-based cancer therapeutics.* J Clin Oncol, 2007. **25**(11): p. 1305-7.

150. Pitti, R.M., et al., *Induction of apoptosis by Apo-2 ligand, a new member of the tumor necrosis factor cytokine family.* J Biol Chem, 1996. **271**(22): p. 12687-90.

151. Walczak, H., et al., *Tumoricidal activity of tumor necrosis factor-related apoptosis-inducing ligand in vivo.* Nat Med, 1999. **5**(2): p. 157-63.

152. Walczak, H., et al., *TRAIL-R2: a novel apoptosis-mediating receptor for TRAIL.* EMBO J, 1997. **16**(17): p. 5386-97.

153. MacFarlane, M., et al., *Identification and molecular cloning of two novel receptors for the cytotoxic ligand TRAIL.* J Biol Chem, 1997. **272**(41): p. 25417-20.

154. Screaton, G.R., et al., *TRICK2, a new alternatively spliced receptor that transduces the cytotoxic signal from TRAIL.* Curr Biol, 1997. **7**(9): p. 693-6.

155. Wu, G.S., et al., *Molecular cloning and functional analysis of the mouse homologue of the KILLER/DR5 tumor necrosis factor-related apoptosis-inducing ligand (TRAIL) death receptor.* Cancer Res, 1999. **59**(12): p. 2770-5.

156. Ashkenazi, A. and V.M. Dixit, *Death receptors: signaling and modulation.* Science, 1998. **281**(5381): p. 1305-8.

157. Degli-Esposti, M.A., et al., *Cloning and characterization of TRAIL-R3, a novel member of the emerging TRAIL receptor family.* J Exp Med, 1997. **186**(7): p. 1165-70.

158. Degli-Esposti, M.A., et al., *The novel receptor TRAIL-R4 induces NF-kappaB and protects against TRAIL-mediated apoptosis, yet retains an incomplete death domain.* Immunity, 1997. **7**(6): p. 813-20.

159. Marsters, S.A., et al., *A novel receptor for Apo2L/TRAIL contains a truncated death domain.* Curr Biol, 1997. **7**(12): p. 1003-6.

160. Pan, G., et al., *TRUNDD, a new member of the TRAIL receptor family that antagonizes TRAIL signalling.* FEBS Lett, 1998. **424**(1-2): p. 41-5.

161. Emery, J.G., et al., *Osteoprotegerin is a receptor for the cytotoxic ligand TRAIL.* J Biol Chem, 1998. **273**(23): p. 14363-7.

162. LeBlanc, H.N. and A. Ashkenazi, *Apo2L/TRAIL and its death and decoy receptors.* Cell Death Differ, 2003. **10**(1): p. 66-75.

163. Miyashita, T., et al., *Osteoprotegerin (OPG) acts as an endogenous decoy receptor in tumour necrosis factor-related apoptosis-inducing ligand (TRAIL)-mediated apoptosis of fibroblast-like synovial cells.* Clin Exp Immunol, 2004. **137**(2): p. 430-6.

164. Gochuico, B.R., et al., *TRAIL expression in vascular smooth muscle.* Am J Physiol Lung Cell Mol Physiol, 2000. **278**(5): p. L1045-50.

165. Sato, K., et al., *TRAIL-expressing T cells induce apoptosis of vascular smooth muscle cells in the atherosclerotic plaque.* J Exp Med, 2006. **203**(1): p. 239-50.

166. Secchiero, P., et al., *TRAIL promotes the survival, migration and proliferation of vascular smooth muscle cells.* Cell Mol Life Sci, 2004. **61**(15): p. 1965-74.

167. Kavurma, M.M., et al., *TRAIL stimulates proliferation of vascular smooth muscle cells via activation of NF-kappaB and induction of insulin-like growth factor-1 receptor.* J Biol Chem, 2008. **283**(12): p. 7754-62.

168. Secchiero, P., et al., *Systemic tumor necrosis factor-related apoptosis-inducing ligand delivery shows antiatherosclerotic activity in apolipoprotein E-null diabetic mice.* Circulation, 2006. **114**(14): p. 1522-30.

169. Lawrie, A., et al., *Evidence of a role for osteoprotegerin in the pathogenesis of pulmonary arterial hypertension.* Am J Pathol, 2008. **172**(1): p. 256-64.

170. Lawrie, A., et al., *Paigen diet-fed apolipoprotein E knockout mice develop severe pulmonary hypertension in an interleukin-1-dependent manner.* Am J Pathol, 2011. **179**(4): p. 1693-705.

171. Hameed, A.G., et al., *Inhibition of tumor necrosis factor-related apoptosis-inducing ligand (TRAIL) reverses experimental pulmonary hypertension.* J Exp Med, 2012. **209**(11): p. 1919-35.

172. Vergadi, E., et al., *Early macrophage recruitment and alternative activation are critical for the later development of hypoxia-induced pulmonary hypertension.* Circulation, 2011. **123**(18): p. 1986-95.

173. Todorovich-Hunter, L., et al., *Increased pulmonary artery elastolytic activity in adult rats with monocrotaline-induced progressive hypertensive pulmonary vascular disease compared with infant rats with nonprogressive disease.* Am Rev Respir Dis, 1992. **146**(1): p. 213-23.

174. Todorovich-Hunter, L., et al., *Altered elastin and collagen synthesis associated with progressive pulmonary hypertension induced by monocrotaline. A biochemical and ultrastructural study.* Lab Invest, 1988. **58**(2): p. 184-95.

175. Rabinovitch, M., *Pulmonary hypertension: updating a mysterious disease.* Cardiovasc Res, 1997. **34**(2): p. 268-72.

176. Cowan, K.N., P.L. Jones, and M. Rabinovitch, *Elastase and matrix metalloproteinase inhibitors induce regression, and tenascin-C antisense prevents progression, of vascular disease.* J Clin Invest, 2000. **105**(1): p. 21-34.

177. Cowan, K.N., et al., *Complete reversal of fatal pulmonary hypertension in rats by a serine elastase inhibitor.* Nat Med, 2000. **6**(6): p. 698-702.

178. Stenmark, K.R., et al., *Animal models of pulmonary arterial hypertension: the hope for etiological discovery and pharmacological cure.* Am J Physiol Lung Cell Mol Physiol, 2009. **297**(6): p. L1013-32.

179. Michelakis, E.D., *Pulmonary arterial hypertension: yesterday, today, tomorrow.* Circ Res, 2014. **115**(1): p. 109-14.

180. Cogan, J.D., et al., *High frequency of BMPR2 exonic deletions/duplications in familial pulmonary arterial hypertension.* Am J Respir Crit Care Med, 2006. **174**(5): p. 590-8.

181. Rich, S., et al., *Primary pulmonary hypertension. A national prospective study.* Ann Intern Med, 1987. **107**(2): p. 216-23.

182. Aldred, M.A., et al., *BMPR2 gene rearrangements account for a significant proportion of mutations in familial and idiopathic pulmonary arterial hypertension.* Hum Mutat, 2006. **27**(2): p. 212-3.

183. Paulin, R. and E.D. Michelakis, *The metabolic theory of pulmonary arterial hypertension.* Circ Res, 2014. **115**(1): p. 148-64.

184. Agard, C., et al., *Protective role of the antidiabetic drug metformin against chronic experimental pulmonary hypertension.* Br J Pharmacol, 2009. **158**(5): p. 1285-94.

185. Himes, B.E., et al., *Integration of mouse and human genome-wide association data identifies KCNIP4 as an asthma gene.* PLoS One, 2013. **8**(2): p. e56179.

186. Berndt, A., et al., *Identification of fat4 and tsc22d1 as novel candidate genes for spontaneous pulmonary adenomas.* Cancer Res, 2011. **71**(17): p. 5779-91.

187. Yang, H., et al., *A customized and versatile high-density genotyping array for the mouse.* Nat Methods, 2009. **6**(9): p. 663-6.

188. Yang, H., et al., *Subspecific origin and haplotype diversity in the laboratory mouse.* Nat Genet, 2011. **43**(7): p. 648-55.

189. Zhou, X. and M. Stephens, *Efficient multivariate linear mixed model algorithms for genome-wide association studies.* Nat Methods, 2014. **11**(4): p. 407-9.

190. Zhou, X. and M. Stephens, *Genome-wide efficient mixed-model analysis for association studies.* Nat Genet, 2012. **44**(7): p. 821-4.

191. Menche, J., et al., *Disease networks. Uncovering disease-disease relationships through the incomplete interactome.* Science, 2015. **347**(6224): p. 1257601.

192. Eppig, J.T., et al., *The Mouse Genome Database (MGD): facilitating mouse as a model for human biology and disease.* Nucleic Acids Res, 2015. **43**(Database issue): p. D726-36.

193. Parikh, V.N., et al., *MicroRNA-21 integrates pathogenic signaling to control pulmonary hypertension: results of a network bioinformatics approach.* Circulation, 2012. **125**(12): p. 1520-32.

194. Brandes, U., *On variants of shortest-path betweenness centrality and their generic computation.* Social Networks, 2008. **30**(2): p. 136-145.

195. Umar, S., M. Rabinovitch, and M. Eghbali, *Estrogen paradox in pulmonary hypertension: current controversies and future perspectives.* Am J Respir Crit Care Med, 2012. **186**(2): p. 125-31.

196. Rajkumar, R., et al., *Genomewide RNA expression profiling in lung identifies distinct signatures in idiopathic pulmonary arterial hypertension and secondary pulmonary hypertension.* Am J Physiol Heart Circ Physiol, 2010. **298**(4): p. H1235-48.

197. Janssens, V. and J. Goris, *Protein phosphatase 2A: a highly regulated family of serine/threonine phosphatases implicated in cell growth and signalling.* Biochem J, 2001. **353**(Pt 3): p. 417-39.

198. Alessi, D.R., et al., *Inactivation of p42 MAP kinase by protein phosphatase 2A and a protein tyrosine phosphatase, but not CL100, in various cell lines.* Curr Biol, 1995. **5**(3): p. 283-95.

199. Nakashima, Y., et al., *ApoE-deficient mice develop lesions of all phases of atherosclerosis throughout the arterial tree.* Arterioscler Thromb, 1994. **14**(1): p. 133-40.

200. Van Gaal, L.F., I.L. Mertens, and C.E. De Block, *Mechanisms linking obesity with cardiovascular disease.* Nature, 2006. **444**(7121): p. 875-80.

201. Sander, J.D. and J.K. Joung, *CRISPR-Cas systems for editing, regulating and targeting genomes.* Nat Biotechnol, 2014. **32**(4): p. 347-55.

202. Mulvany, M.J., *Small artery remodeling in hypertension.* Curr Hypertens Rep, 2002. **4**(1): p. 49-55.

203. Bentley, J.K. and M.B. Hershenson, *Airway smooth muscle growth in asthma: proliferation, hypertrophy, and migration.* Proc Am Thorac Soc, 2008. **5**(1): p. 89-96.

204. Hunninghake, G.M., et al., *MMP12, lung function, and COPD in high-risk populations.* N Engl J Med, 2009. **361**(27): p. 2599-608.